A Portable Colorimetric Sensing Platform for the Evaluation of Carbon Dioxide in Breath

by

Devon Taylor Bridgeman

A Dissertation Presented in the Partial Fulfillment
of the Requirements for the Degree
Doctor of Philosophy

Approved April 2017 by the
Graduate Supervisory Committee:

Erica Forzani, Chair
Gregory Raupp
Heather Emady
Julianne Holloway
Mehdi Nikkhah

ARIZONA STATE UNIVERSITY

May 2017

ABSTRACT

This work describes the development of a device for measuring CO_2 in breath, which has applications in monitoring a variety of health issues, such as Chronic Obstructive Pulmonary Disease (COPD), asthma, and cardiovascular disease. The device takes advantage of colorimetric sensing technology in order to maintain a low cost and high user-friendliness. The sensor consists of a pH dye, reactive element, and base coated on a highly porous Teflon membrane. The transmittance of the sensor is measured in the device via a simple LED/photodiode system, along with the flow rate, ambient relative humidity, and barometric pressure. The flow is measured by a newly developed flow meter described in this work, the Confined Pitot Tube (CPT) flow meter, which provides a high accuracy with reduced flow-resistance with a standard differential pressure transducer. I demonstrate in this work that the system has a high sensitivity, high specificity, fast time-response, high reproducibility, and good stability. The sensor has a simple calibration method which requires no action by the user, and utilizes a sophisticated, yet lightweight, model in order to predict temperature changes on the sensor during breathing and track changes in water content. It is shown to be effective for measuring CO_2 waveform parameters on a breath-by-breath basis, such as End-Tidal CO_2, Alveolar Plateau Slope, and Beginning Exhalation Slope.

TABLE OF CONTENTS

TABLE OF CONTENTS

CHAPTER Page

TABLE OF CONTENTS

CHAPTER Page

TABLE OF CONTENTS

LIST OF TABLES

Table Page

LIST OF FIGURES

Figure Page

LIST OF FIGURES

Figure Page

LIST OF FIGURES

Figure Page

LIST OF FIGURES

Figure Page

LIST OF FIGURES

Figure Page

LIST OF FIGURES

Figure Page

LIST OF FIGURES

Figure Page

LIST OF FIGURES

Figure Page

LIST OF FIGURES

Figure Page

LIST OF FIGURES

Figure Page

1. Introduction

Carbon dioxide is the third largest component of exhaled breath and a powerful biomarker for measuring the performance of the cardiorespiratory system. By measuring exhaled carbon dioxide and breath flows, one can gain insights into their metabolism[1], level of lung obstruction[2-4], ventilation status[5], blood acid-base status[6,7], cardiac output[8], and many other parameters[9]. The measurement of carbon dioxide in exhaled breath, otherwise known as Capnography, gives an opportunity to directly monitor the effectiveness of the cardiopulmonary system non-invasively. Currently, capnography is mainly used while administering anesthesia[5], mechanical ventilation[10], and other critical applications[11]. Capnography measurements have very far-reaching applications in the medical landscape. Applications require a fast-response time response, high temporal resolution, wide measurement range, and a high accuracy.[9,12] There are two main methods in which to interpret capnography results: On a per-time basis or on a per-volume basis. Each has their benefits and challenges, with volumetric capnography also requiring accurate flow measurements that do not impede normal breathing. Because of this, capnography devices are typically big, bulky, and relatively expensive (for suitable accuracy) which limits its applications to hospital use. In this work, I present the development of a low-cost, user-friendly capnography device which is capable of performing on-par with or better than current commercially available technology with both volumetric- and time-based measurements.

1.1 Potential Applications of a Mobile-Health Capnography Device

Developing a low-cost and user-friendly Capnometer opens many new opportunities in patient care. Respiratory illness is generally a chronic condition, which means that the patient will need to be monitored indefinitely to detect a worsening of the condition; hence, it is useful to monitor a patient to see if a treatment plan is working or to alert the patient when immediate care is needed. Although there are many diseases that can be monitored via capnography in home-monitoring, the most prevalent are obstructive disorders, mainly Chronic Obstructive Pulmonary Disease (COPD) and Asthma, with applications also being seen with cardiopulmonary disease. In the most severe cases of COPD, it becomes medically necessary to administer oxygen therapy. When administering oxygen, a major concern is a buildup of carbon dioxide in the blood, which can cause serious health issues. In addition to lung obstruction, capnography provides a non-invasive method to measure cardiac output, which is a valuable parameter for a wide variety of diseases, such as hypertension, heart failure, and many other diseases. Cardiac output is currently not a measurement available in the home setting, as many current methods require expensive equipment and trained professionals, with the most trusted methods being extremely invasive.

1.1.1Lung Obstruction (COPD and Asthma)

COPD and Asthma are two of the most prevalent diseases in the United States, with over 15 million Americans diagnosed with COPD[13] and over 17 million Americans

diagnosed with Asthma[14]. COPD is a group of diseases characterized by restriction of airways in the lungs, thus making breathing more difficult and in more severe cases leading to lower oxygen saturation levels and increased carbon dioxide levels in the blood. Asthma is also the restriction of airways, but is more episodic in nature and generally less severe (with more severe cases also being characterized as COPD). Treatments for COPD tend to vary, but monitoring of the disease is important in order to evaluate the efficacy of a treatment[15]. In the clinical setting, monitoring is typically done using spirometry. Spirometry is a volume-based breath measurement which consists of flow measurements taken as a person takes a full inhale then exhales with maximum effort. The test gives a measure of airway constriction and is the accepted diagnostic method for COPD[15]. Spirometry is a very powerful tool in the clinical setting, but unfortunately it is not feasible for home care due to the need for a medical professional to administer the test. Spirometry also poses a unique challenge for Asthma diagnosis in that the condition is episodic, with spirometry parameters often do not correlate with Asthma severity outside of an episode[16]. Because of this, Asthma severity assessment is very difficult to assign via a general metric[17].

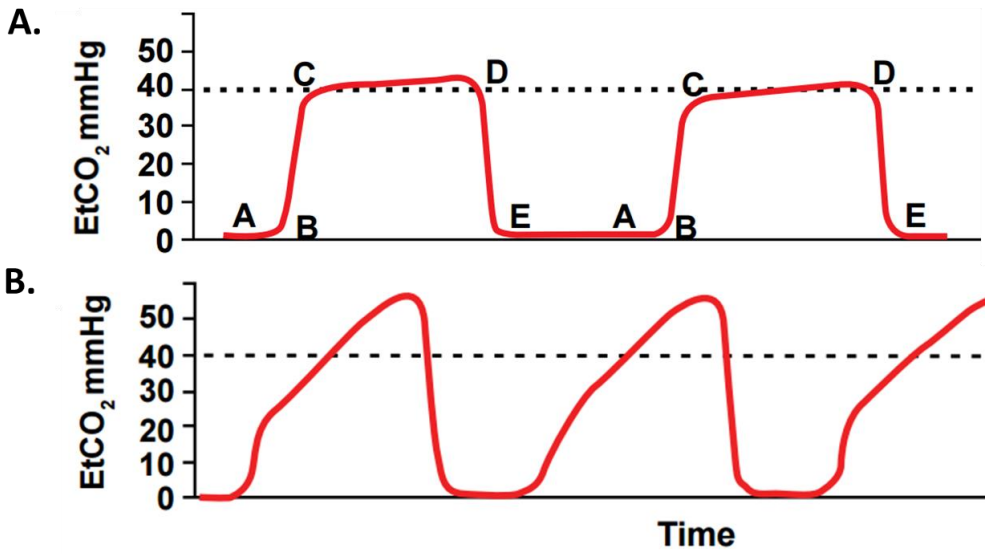

Figure 1-1. Comparison of Capnographic Waveforms of a health subject (A) and a subject with lung obstruction (B). The markers in part A note the different portions of the breathing waveform: A-B is the inspiratory baseline, B-C is the beginning of exhalation, C-D is the alveolar plateau, and D-E is the beginning of inspiration.[18]

Capnography waveforms give an additional perspective in order to evaluate lung function. Where spirometry is looking at only physical parameters in the lung, capnography gives a direct measurement of gas transport during respiration. By directly measuring gas transport in the lungs, Capnography can provide improved implementations to provide new insights on patient health. Two common parameters sought after in capnography traces are the end-tidal carbon dioxide (point D on figure 1.1.A) and the slope of the alveolar plateau (slope between points C and D on figure 1.1.A). In figure 1.1, two time-based capnography traces are shown, with part A showing

a healthy subject and part B showing a subject with lung obstruction. The reason for the differences between the two CO_2 traces is due to pulmonary heterogeneity: the fact that different paths in the lungs will have different gas exchange properties.[19] Due to the inhomogeneous gas exchange, breathing will not provide ideal flows in airways, leading to insufficient airflow in lower airways in the lungs. Due to a lack of airflow, earlier air exhaled will have lower levels of CO_2 (this air was in higher airways) while later air exhaled will have abnormally high levels of CO_2 (this air was in low-flow conditions in lower airways). Due to the nature of the condition, Capnography is provided with many parameters to track.

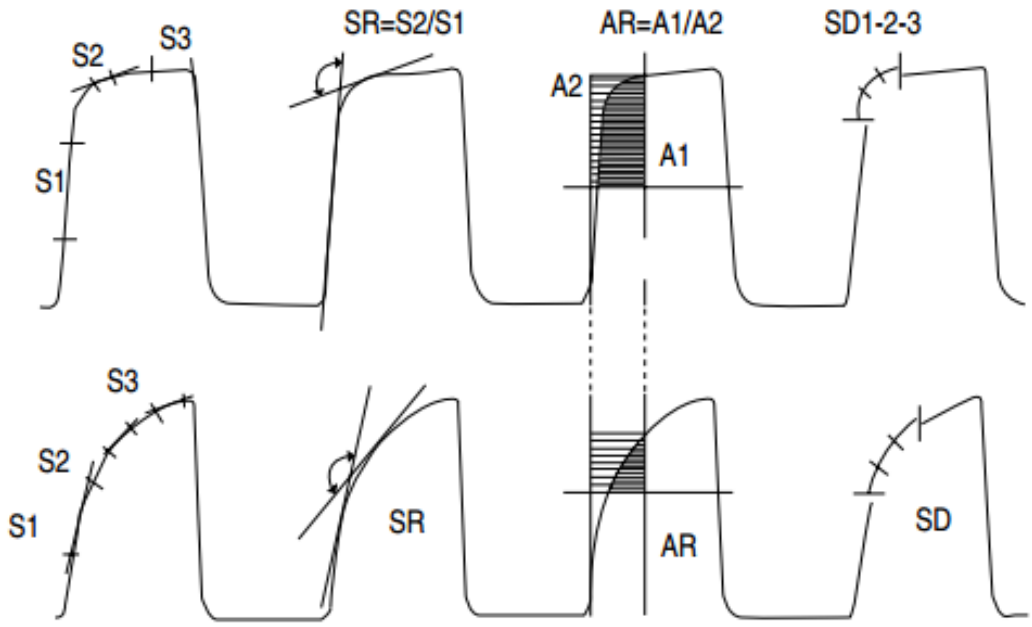

Figure 1-2. A number of Capnography indices investigated for application to Asthma stage diagnosis, with an unobstructed waveform on the top row and obstructed waveform

on the bottom row. S1,S2, and S3 represent slopes in the waveform at the beginning of the breath, in the middle of the breath, and at the end of the breath, respectively. SR represents the ratio between slopes. AR represents the Area Ratio between areas under and over the curve as a measure of curvature during a relevant range of breathing. SD represents the second derivative, which is a direct measure of curvature.[4]

Yaron, You, Krauss, and others have previously discussed several relevant applications of capnography in evaluating lung obstruction.[4,20,21] B. You et al evaluated time-based capnography waveforms in order to see what parameters could be measured and how well said parameters correlate with spirometry tests (see figure 1.1-2). Although many parameters have been tested, End-Tidal CO_2 and the slope of the alveolar plateau are still the most common. Many studies have shown correlation between these Capnography indices and spirometry measurements, which demonstrates that the indices are correlated with the severity of lung obstruction.

By measuring these over time, a physician can get direct and quantifiable feedback on how a patient is responding to treatment, which opens new avenues in looking at precision-medicine approaches. Many severe cases of COPD tend to lead to hospitalization, and the rehospitalization rate among COPD patients is an ongoing issue, with rehospitalization even being a target of the Affordable Healthcare Act[22]. Hospitalizations are generally due to acute exacerbations, and have been shown to correlate with physical activity and depression[23,24]. Our lab has previously demonstrated

that health tracking can increase engagement in health goals and result in better outcomes[25]. COPD rehospitalization is a disaster for patients, and also presents a significant cost factor in healthcare, with a rehospitalization costing upwards of $10,000 on average as of 2008[26].

1.1.2 Oxygen Therapy

For advanced cases of COPD, oxygen therapy is a very common treatment. Supplementing oxygen to a COPD patient can restore mobility, restore quality of life, and keep patients alive. Increases of CO_2 in the body during oxygen therapy are due to two main culprits: the Haldane effect and changes in respiratory drive. The Haldane effect is the phenomenon in which by increasing oxygen saturation in the hemoglobin, the capacity for hemoglobin to carry CO_2 is decreased. The Haldane effect is generally of largest concern when beginning oxygen therapy. Changes in respiratory drive, however, are caused by a change in drive from lower oxygen levels. When a hypoxic patient is introduced to oxygen therapy, they cease to be hypoxic and lower their respiration rate as a result, which causes less CO_2 to be expelled. In oxygen therapy, CO_2 retention remains the leading risk in terms of side effects[27,28].

1.1.3 Cardiac Output

Cardiac output is the measure of the volume of blood that the heart is pumping at any given time. In patients with cardiovascular disease, cardiac output measurement can provide an important parameter for diagnosis and monitoring[29]. Cardiovascular disease is

the leading cause of death in the United States, which means that there is a need for improved methods in monitoring and treatment[30]. Unfortunately, current methods for measurement of cardiac output require bulky equipment or invasive procedures, both of which prohibit monitoring in the home setting and limit monitoring in the clinical setting. Two common methods are the Fick method and the thermodilution method. Both methods are very invasive as they involve direct measurement of arterial blood concentrations.

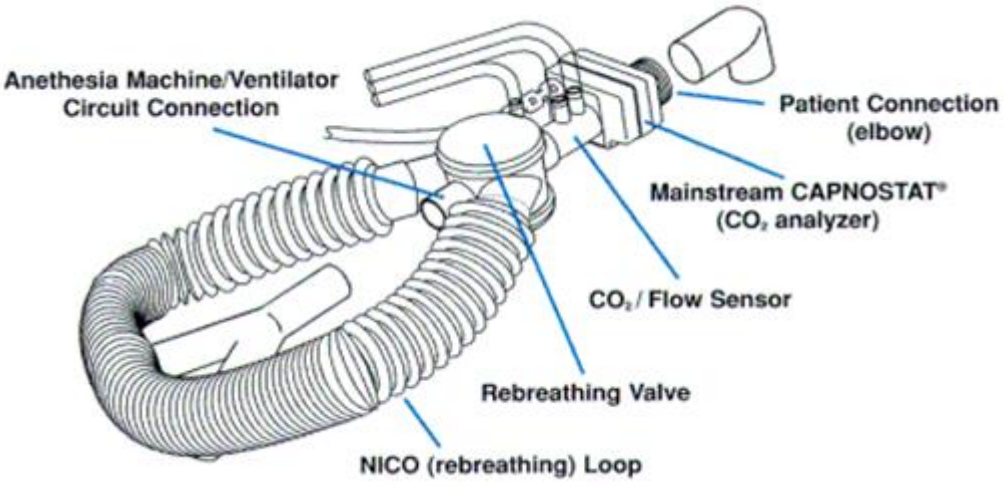

Figure 1-3. Diagram of a NICO (Non-Invasive Cardiac Output) breathing circuit. The breathing apparatus is hooked up to the patient's airway and periodically the rebreathing valve is switched to the rebreathing loop, where a patient will rebreathe the previous breath. The difference in end-tidal concentrations and volumes of CO_2 expelled are then analyzed.[31]

One example of a less invasive and more portable method is the NICO (non-invasive cardiac output) unit (Respironics, Philips Healthcare), which utilizes the Indirect Fick Method.[31] This method involves monitoring carbon dioxide, then seeing changes in the concentration with partial rebreathing (as seen in Figure 1-3), which has been shown to be an effective method for measuring cardiac output for a variety of conditions[8,32-34]. The NICO is targeted towards critical care and inpatient applications due to its price and the healthcare professionals needed to operate the instrumentation. There is a need for a low-cost and patient-user friendly device that would allow for monitoring in the home setting.

1.3 Current Breath Carbon Dioxide Technologies

1.3.1 Thermal Conductance

One of the simplest methods for measuring Carbon Dioxide is by measuring thermal conductance. With different gasses there are differences in thermal conductance. The principle of the measurement is to measure the thermal conductance of the sample gas against a reference, which in most applications is atmospheric gas. An example of a thermal conductivity sensor is shown in Figure 1-4, where sample and reference gases are passed over resistive elements which vary with temperature, which at constant flows will vary with thermal conductance. By constructing a Wheatstone Bridge, there is a simple measurement that can be calibrated: when all resistances are equal, there is no voltage out and with large differences in resistance, a greater voltage is measured[35]. A thermal

conductance sensor will be calibrated based on the gas being measured. Carbon dioxide is commonly measured in this manner for relatively high (4% and higher) applications, with breath measurement being one application. Although a reliable method for many applications, breath measurement poses unique challenges: the thermal conductance of a gas changes drastically with humidity and the measurement rate for these sensors is fairly slow, which makes capnography measurements difficult with this method[35,36].

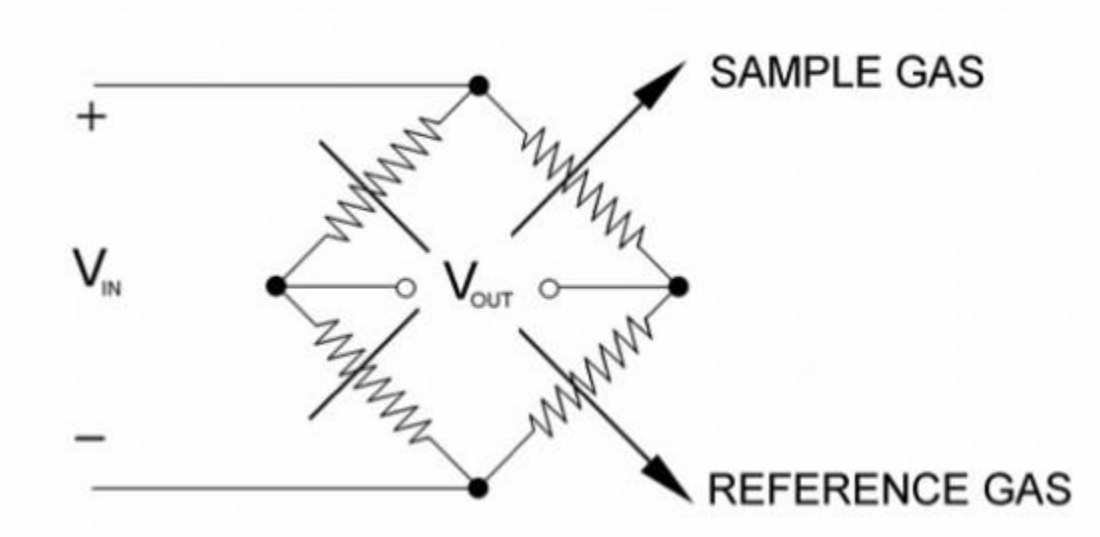

Figure 1-4. A diagram of a Thermal Conductivity gas sensor Wheatstone Bridge.[35]

1.3.2 Non-Dispersive Infrared (NDIR) Detection

Non-Dispersive Infrared (NDIR) detection of carbon dioxide is the most widespread, although it presents issues which limit its utility in home care. The method is

very simple in principle: infrared light is passed through the gas sample and the absorbance of light is measured. A wide-band infrared source is used, and then a bandpass optical filter is used in order to quantify the transmittance at a particular wavelength (see Figure 1-5).

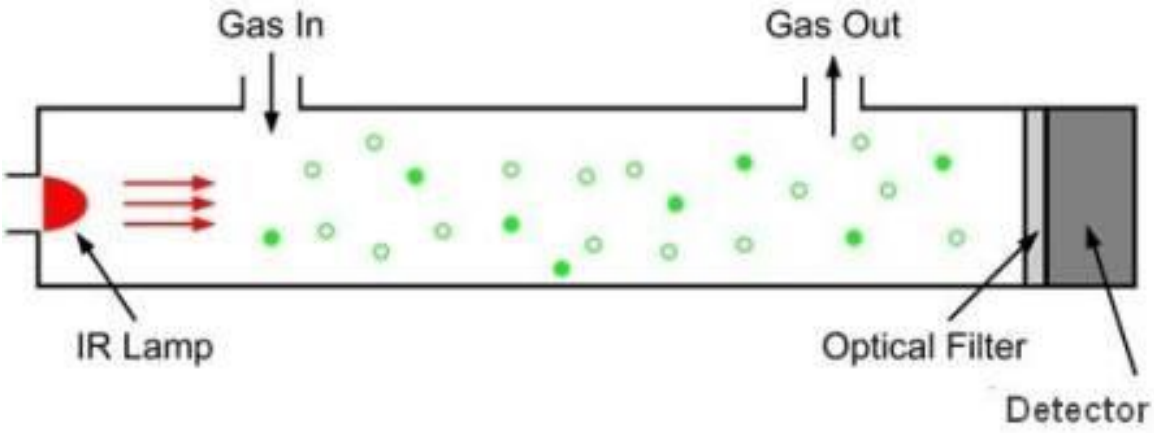

Figure 1-5. A Non-Dispersive Infrared Detector.[37]

This design has many challenges for detection CO_2 in breath. The main challenge is that breath is moist and water interferes with the CO_2 measurement: gaseous water absorbs light at the wavelength that is optimal for detecting CO_2 and condensed water refracts light. There are three common methods for dealing with this issue: 1. The sample can be dried before analysis, although reversible drying methods (such as Nafion Tubing) leave the sample at ambient relative humidity, meaning the sensor must be calibrated for ambient humidity. 2. The sample can be measured at two wavelengths, one for CO_2 and water and another just for water. Some issues with this are an increased cost and still a

failure to deal with condensed water. 3. The sample can be heated and sampled at two wavelengths. This eliminates effects from water, but is the most expensive.

The other main challenge of NDIR detection is temperature. The density of gas is dependent on temperature, so in a fixed volume the number of moles of gas is dependent on temperature. In addition, the components used for emission of infrared light and the photodetectors may have a dependence on temperature. This issue can be especially problematic in mainstream systems, and are often mitigated with heating, which adds more complexity and more cost to the system.

1.3.3 Colorimetric Detection

Colorimetric chemical detection is a very widespread method for detecting a very wide array of chemicals, with current market applications for colorimetric sensors ranging from pH paper, to metabolic analyzers, to heavy metal tests, to home pregnancy tests[1,38-41]. Colorimetric sensors have proven to be a reliable, accurate, and low cost sensing solution in many areas. Despite the successes of colorimetric detection methods, they still suffer from the same issues as most chemical sensors. One major challenge facing chemical detection is degradation over time. Most chemical sensors will degrade over time, which is an especially problematic issue for quantitative sensors, such as glucose strips. In order to handle this, special considerations need to be taken in the storage and evaluation of shelf life, and even better is that the platform can account for degradation over time and compensate for it.

Breathing (and especially rebreathing) offers additional challenges to colorimetric detection. Breath is a complex medium with a saturated relative humidity and elevated temperature, which in most cases will greatly affect the sensor reading. In on-direction analysis, this can be difficult to handle due to moisture accumulation and steadily increasing temperature through the test. In rebreathing systems, this can be difficult to handle due to cyclically changing temperature and humidity. The pattern of the cycle varies widely patient to patient and the magnitudes of the temperature and humidity shifts depend on the patient's surroundings. In order to combat this in a rebreathing setup, a robust model is needed in order to account for these variations. Physical measurement is generally difficult due to the nature of the sensors: colorimetric sensors are generally thin film sensors, which makes the use of contact measurement difficult, and non-contact temperature methods are expensive, which negates the cost-benefit of producing colorimetric sensors.

2 Development of a Colorimetric Sensing Platform for Human Breathing

A major portion of the work put into the project has been in developing the technology surrounding the sensor. This involves the system for translating the color change of the sensor into a signal, measuring the factors that affect the sensors (temperature, humidity, barometric pressure, and flow), transmitting the data to the phone, and translating the data into CO_2 waveforms and extracted parameters. A major portion of this work has been in developing a suitable flow sensor for a low cost, which

involves balancing accuracy and flow-resistance. The device can provide accurate flows at a low flow-resistance, measure the transmittance of the colorimetric sensing element, measure relative humidity and barometric pressure, and measure the appropriate temperatures in order to compensate for temperature effects in the device.

2.1 The Confined Pitot Tube (CPT) Flow Meter

Accurate measurement of breath flow rates is essential for volumetric capnography, along with many other respiratory tests, such as spirometry and metabolic analysis. To obtain good performance during volumetric capnography measurements, the following requirements are necessary: 1) High sensitivity and accuracy to detect low flow rates. 2) Low flow-resistance for enabling unperturbed exhalation and inhalation measurements[42]. 3) Capability to differentiate flow direction. 4) Capability to correct for humidity and temperature changes present during breathing.

There are many commercially available products currently for measuring relaxed breath flows[9,43], including turbine, hot-wire, ultrasonic, and differential pressure flow meters[9,43]. Each flow meter has its advantages and disadvantages. Turbine flow meters are ideal for applications with low flow-resistance; however, their accuracy is limited at low flow rates, and breathing maneuvers can cause errors due to "lag-before-start" and "spin-after-stop" effects[44,45]. Hot-wire flow meters are fairly common in one-direction flow metering, but require warm-up, frequent calibration, and knowledge of gas composition[46]. Ultrasonic flow meters can measure flow direction and require infrequent

calibration, but their sensitivity to factors altering the speed of sound (mainly gas composition, temperature, and humidity) limits their application in relaxed breath flow measurements[9,47].

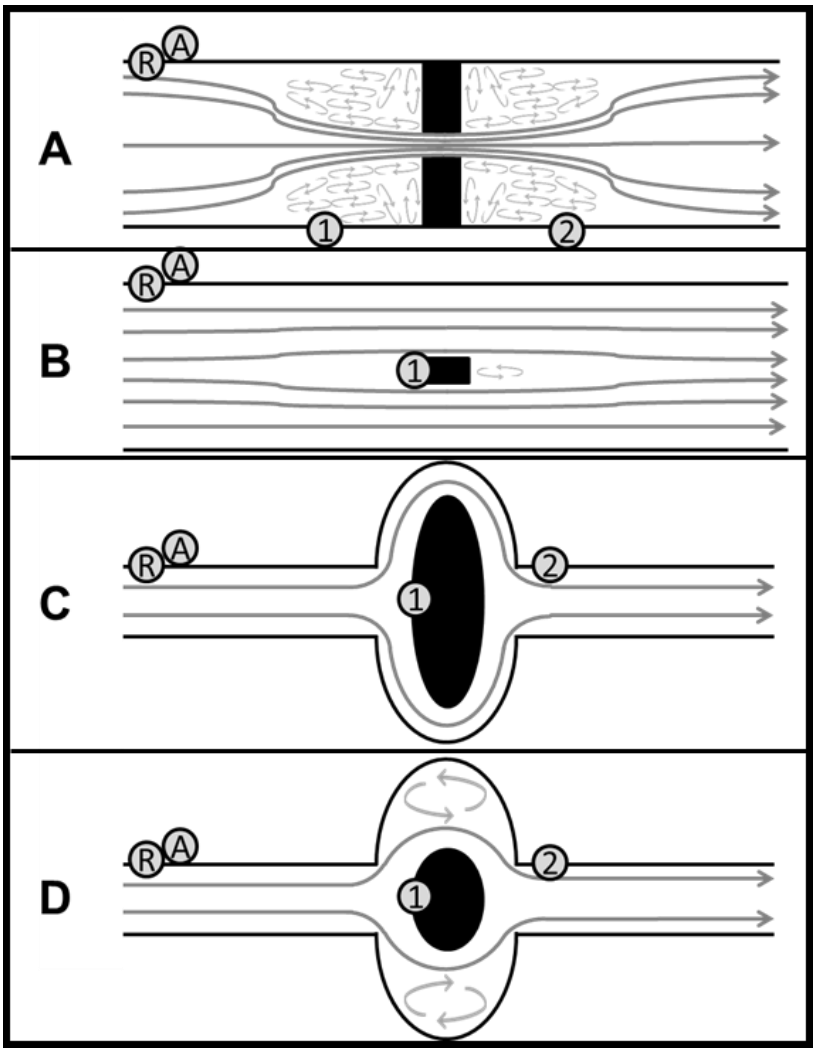

Figure 2-1. Streamline flows for: (A) an orifice flow meter, (B) a Pitot Tube flow meter, and (C and D) Confined Pitot Tube flow meter with high (C) and low (D) confinement,

including a buffer region. The circles indicate sampling ports: (1) at the center of the disk's face and (2) on the wall of the tube, or atmospheric pressure port (A), which is outside the flow system. Flow-resistance is measured in any of the setups at port (R) relative to atmospheric pressure (A).

Differential pressure flow meters are very widely used due to their simplicity, robustness, and adaptability (Figure 2-1). Among them, Fleish-type meters, which rely upon the pressure drop across a capillary screen, provide good linear response, but they are susceptible to clogs, difficult to clean, and require frequent calibration[48]. Orifice flow meters are simple, robust, and inexpensive to implement, but they have high flow-resistance[43]. Variable-orifice flow meters provide a reduced flow-resistance by having an orifice size proportional to flow; however they are more expensive and prone to mechanical wear out over time[9]. Alternatively, Pitot Tube flow meters have very low flow-resistance and can be inexpensive to implement. In these meters, typically, pressure sampling is done in the center of fluid flow where the velocity is highest. Since the pressure sampling port is stationary, a stagnation pressure develops proportional to the flow rate. However, the sensitivity of a Pitot Tube is generally very low and limited to fairly steady flows[49]. Thus, despite the field being very well developed for differential pressure flow meters, bidirectional flow measurement for relaxed breathing conditions is still non-trivial and undeveloped.

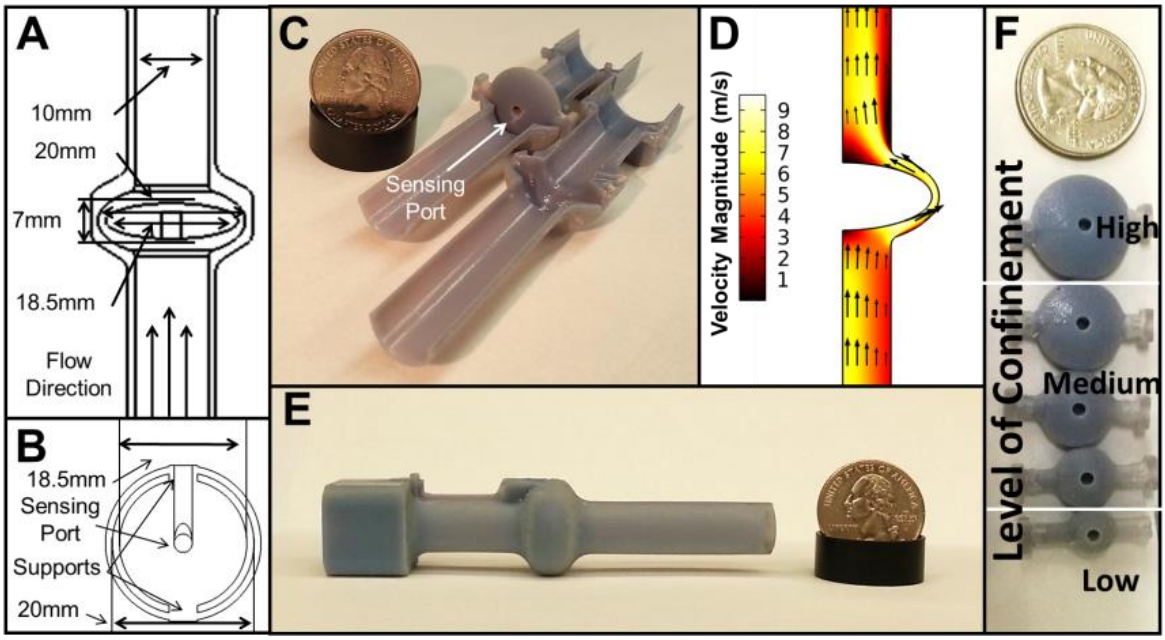

Figure 2-2. (A and B) Schematic of the Confined Pitot Tube. (C) Photograph of the flow meter showing the interior design (view from inlet). (D) Flow pattern of the flow meter as modeled axisymmetrically (model is axisymmetric about the left boundary pictured). The arrows represent the fluid velocity and the tone represents the velocity magnitude (m/s). (E) Photograph showing the profile view of the Confined Pitot Tube flow meter (inlet to the right) placed next to a quarter for scale. (F) Photograph showing the different sizes of inner disks used next to a quarter for scale.

In the present work, a new flow meter called the Confined Pitot Tube is developed, which successfully overcomes the barriers of sensitivity, accuracy, resistance, bi-directionality, and cost of existing flow meters to measure human breath. The new device consists of an elliptical disk with a centered pressure sensing port, as shown in

Figure 2-1C-D and Figure 2-2 A-B. The disk is located in an elliptical expansion cavity placed to reroute flow (Figure 2-2 C). The design leads to increased stagnant pressure at the center of the elliptical disk on the side facing the incoming flow (Figure 2-2 D). In addition, the elliptical disk is exchangeable and has different diameters. When the diameter is large, the gap between the disk and the expansion cavity is small: high confinement flow conditions are present (Figure 2-1 C). On the contrary, when the disk diameter is small, the gap between the disk and the expansion cavity is high, and low confinement flow conditions are developed, and eddies are induced in the buffer regions (Figure 2-1 D). In both, low and high Confined Pitot Tubes, the viscous drag built from the confinement and inertial effects from bending the flow amplify the pressure at lower flow rates, allowing for greater accuracy. For conditions where the flow direction of the device is inverted (e.g., inhalation), the confinement of the flow meter yields a high negative pressure signal at the sampling pressure port (disk center), allowing for easy differentiation and measurement of flow direction.

Different configurations of the new Confined Pitot Tube flow meter are presented here that use a constant inner radius of 10mm for the elliptical expansion chamber, and variable inner disks of radii ranging from 4.25mm to 9.25mm (Figure 2-2 E-F). The performance of these different configurations is investigated at constant flows of 0 to 20 L/min, as well as at simulated breathing cycles consisting of inhalation and exhalation conditions of [-60;60] L/min (negative referring to inhalation flows). An optimal

geometry rendering maximum sensitivity for low flows, high accuracy, and low flow-resistance for measurement of human breath flow is also identified.

2.2.1 Computational Fluid Mechanics Modeling

Simulations were performed using Comsol Multiphysics®. The Confined Pitot Tube flow sensor was modeled axisymmetrically (see Figure 2D), neglecting the supports of the inner disk to reduce computation time. Two flow models, a laminar model and a k-ω Reynolds-Averaged Navier-Stokes (RANS) turbulent model, were applied using steady-state fluid flows and converged to a tolerance of 0.001.

2.2.2 Laminar Models

Laminar fluid flow[50] was simulated using the Navier-Stokes (1) and continuity (2) equations for a compressible flow:

$$\rho(u \cdot \nabla)u = \nabla \cdot \left[-p\mathrm{I} + \mu(\nabla u + (\nabla u)^T) - \frac{2}{3}\mu(\nabla \cdot u)\mathrm{I}\right] + \mathrm{F} \quad (1)$$

$$\nabla \cdot (\rho u) = 0 \quad (2)$$

where ρ is density, u is fluid velocity, p is pressure, and F is volume force, and ∇, I, and $^{\mathrm{T}}$ represent the gradient, identity matrix, and transpose operators, respectively. The laminar

model was used to simulate flow profile and pressure distributions for constant flow through the flow meter.

2.2.3 Turbulent Models

The k-ω RANS turbulence model was used because currently it is the best two-equation model for flows exhibiting high curvature. Being a two-equation model, it can predict turbulent behavior without previous knowledge of the turbulent structure. The first two-equation k-ω turbulence model was proposed by Kolmogorov[51]. The model was later developed independently by Saffman, greatly improved by Wilcox and Alber, and then revisited and improved by Wilcox[52]. The k-ω model accounts for the turbulent fluctuation (k) (equation 3), as well as the specific dissipation rate (ω) (equation 4):

$$\rho \frac{\partial k}{\partial t} + \rho u \cdot \nabla k = P_k - \rho \beta^* k \omega + \nabla \cdot ((\mu + \sigma^* \mu_T) \nabla k) \tag{3}$$

$$\rho \frac{\partial \omega}{\partial t} + \rho u \cdot \nabla \omega = \alpha \frac{\omega}{k} P_k - \rho \beta \omega^2 + \nabla \cdot ((\mu + \sigma \mu_T) \nabla \omega) \tag{4}$$

where P_k is the production term, which is defined as:

$$P_k = \mu_T (\nabla u : \left(\nabla u + (\nabla u)^T - \frac{2}{3} (\nabla \cdot u)^2 \right) - \frac{2}{3} \rho k \nabla \cdot u \tag{5}$$

The closure coefficients ($\alpha, \beta, \beta^*, \sigma, \sigma^*$)) and eddy viscosity ($\mu_T$) are defined as:

$$\alpha = \frac{13}{25}, \beta = \frac{13}{125} f_\beta, \beta^* = \frac{9}{100} f_{\beta^*}, \sigma = \frac{1}{2}, \sigma^* = \frac{3}{5}, \mu_T = \rho \frac{k}{\omega} \tag{6-11}$$

The closing coefficients β and β^* are variant with factors f_β and f_{β^*}, which depend on non-dimensional measures of vortex stretching χ_k and χ_ω, defined as:

$$f_\beta = \frac{1 + 70\chi_\omega}{1 + 80\chi_\omega}, f_{\beta^*} = \begin{cases} 1 & \text{if} \quad \chi_k \leq 0 \\ \dfrac{1 + 680\chi_k^2}{1 + 400\chi_k^2} & \text{if} \quad \chi_k > 0 \end{cases} \tag{11,12}$$

The parameter χ_ω is based on Pope's non-dimensional measure of vortex stretching parameter (χ_p), and is simply the absolute value of χ_p. χ_k is a non-dimensional parameter defined by k and ω as shown below:

$$\chi_\omega = |\chi_p| = \left| \frac{\Omega_{ij}\Omega_{jk}S_{ki}}{\left(\frac{9}{100}\omega\right)^3} \right|, \chi_k = \frac{1}{\omega^3}(\nabla k \cdot \nabla \omega) \tag{13,14}$$

where $\Omega_{ij}$is the mean rotation tensor, defined by a difference of partial derivatives of the mean velocity ($\bar{u}_i$) and S_{ij} is the mean strain-rate tensor, defined by a sum of partial derivatives of the mean velocity ($\bar{u}_i$), as shown below:

$$\Omega_{ij} = \frac{1}{2}\left(\frac{\partial \bar{u}_i}{\partial x_j} - \frac{\partial \bar{u}_j}{\partial x_i}\right), S_{ij} = \frac{1}{2}\left(\frac{\partial \bar{u}_i}{\partial x_j} + \frac{\partial \bar{u}_j}{\partial x_i}\right) \tag{15,16}$$

2.2.4 Flow Sensor Fabrication

As mentioned before, the Confined Pitot Tube was designed with internal confined pitot disks ranging from 4.25mm to 9.25mm in radius. This radius range was initially determined via simulation results. All the disks were interchangeable and placed in the common expansion cavity of 10mm radius. The disks had a sample port located at the center, as shown in Figure 2-2. The radii of the Confined Pitot Tube's disks allowed the classification of the resulting assembled flow meters as: **a)** low confinement (4.25mm), **b)** moderate confinement (5.5-8mm), and **c)** high confinement (9.25mm) (Figure 2-2 F). The Confined Pitot Tube flow meter device was fabricated using a Stratasys Object Photopolymer 3D printer (Rocky Mountain Tech, LLC). Pressure readings were taken for different configurations, including: **a)** Flow-resistance (point ® and Ⓐ as shown in Figure 2-1 C-D), **b)** One-point sampling (point ① and ② as shown in Figure 2-1 C-D), or **c)** Two-point sampling (point ① and Ⓐ as shown in Figure 1C-D). A Freescale MP3V5004DP differential pressure sensor was used for the differential pressure measurements.

2.2.5 Static Flow Results

Simulations were run for a Confined Pitot Tube with five different inner radii disks ranging from 4.25 mm to 9.25mm (Figure 2-2) in a flow rate range from 2 to 20 L/min of dry air. Both laminar and turbulent simulations were conducted as described in the experimental section, and considered smooth surfaces for the flow with no-slip

conditions. Therefore, it is noteworthy that inaccuracies resulting from surface roughness were not accounted for, along with other minor features. For instance, neither model accounted for the disk supports or the actual pressure sampling ports, which were present in the actual flow chamber. Figure 4 shows an example of the pressure distribution profiles obtained for the Confined Pitot Tube system under laminar flow. It can be observed that the optimal points for measuring differential pressure values are: 1) The pressure at the center of the Confined Pitot Tube, which is a stagnant pressure, and 2) The pressure after the curvature of the Confined Pitot Tube on the wall of the tube. These two pressure points were defined as sampling ports ① and ②, as shown in Figure 2-2 C-D. The simulations verified the correct choice of the sampling ports for maximizing differential pressure measurements, which were correlated to flow rate. As mentioned before, the alternative choice for measuring differential pressure was sampling port ①, and a sampling point outside the system at atmospheric pressure, which was named atmospheric pressure port Ⓐ (Figure 2-1 C-D).

Figure 2-4 shows plots for differential pressure experimental measurements vs. flow rate for different Confined Pitot Tube flow meters of various radii with *one-point sampling* (left side) for assessment at sampling port ① vs. Ⓐ, and *two-point sampling* (right side) for assessment at sampling port ① vs. ②. In addition, the simulation results for both models, laminar and turbulent, at each corresponding condition are shown for comparison. Two-point sampling provides a slightly higher signal, but not a significant

difference in performance compared to one-point sampling. Additional analysis of results represented in Figure 2-4 indicates a trend that could be classified as follows:

a. Low confinement flows: The smallest inner disk of 4.25mm in radius (Figure 2-5 A-B) was better described by the turbulent flow model. The relatively big gap between the external wall of the device and the inner wall of the disk yields a buffer area, which leads to turbulence at relatively low flow rates.

b. High confinement flows: The largest inner disk of 9.25mm in radius is well described by the laminar flow model (Figure 2-4 I-J). In this case, a relatively high sensitivity of ~3 Pa at a low flow rate of 2 L/min flow using two-point sampling with a low flow-resistance was observed. The high confinement design provides a relatively small gap between the external wall of the device and the inner wall of disk, which yields mainly laminar flows. The analytical sensitivity and flow-resistance of this specific design made it an inner disk dimension of choice for the design of a flow meter for breath analysis.

c. Moderate confinement flows: Intermediate inner disk radii of 5.5 mm to 8.0 mm were better described by the laminar model at flows less than 10 L/min and better described by the turbulent model flows greater than 12 L/min (Figure 2-5 C-H).

Comparison of Confined Pitot Tube Flow Meter and Fixed Orifice Flow Meter

In order to benchmark the performance of the Confined Pitot Tube flow meter, it was compared to a Fixed Orifice flow meter with a 2.5mm orifice radius (Figure 2-1 A)

in both signal and flow-resistance. The dimension of the orifice was chosen to establish a comparison with state-of-the-art commercial flow meters for breath.[53]

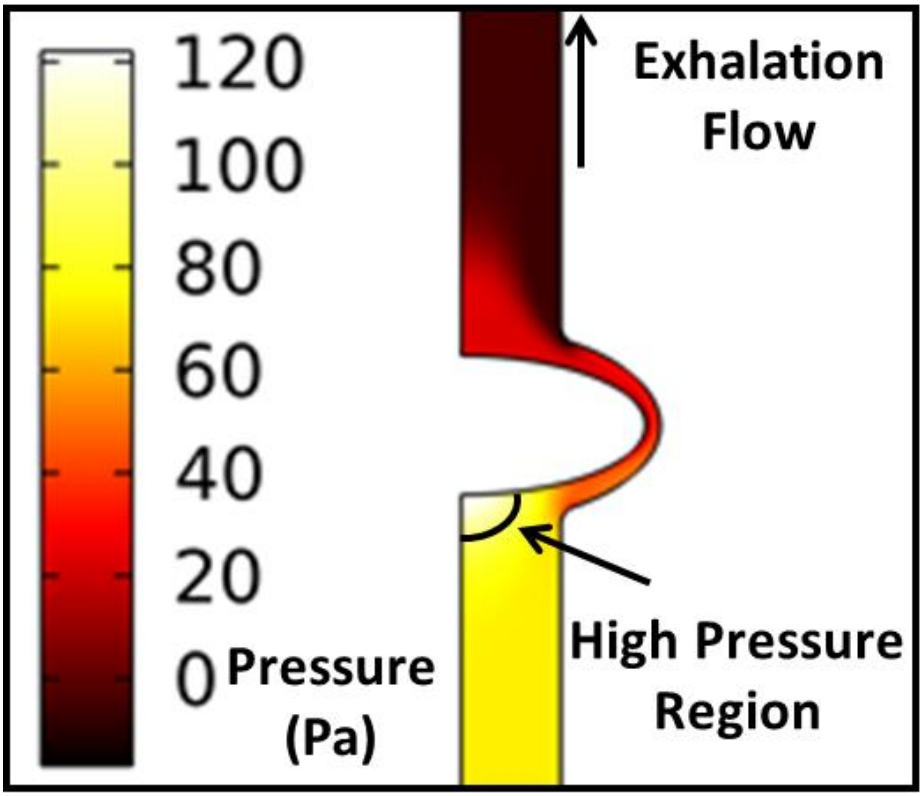

Figure 2-3. Pressure distribution (Pa) in the Confined Pitot Tube flow meter simulated with 9.25mm inner radius disk at 20L/min flow for laminar model. Note that the direction of flow is from bottom to top; the greatest pressure is at the center of the face of the disk, where sampling port 1 is located, and the lowest pressure is on the wall immediately after the disk, where sampling port 2 is located (Figure 2-1 C-D).

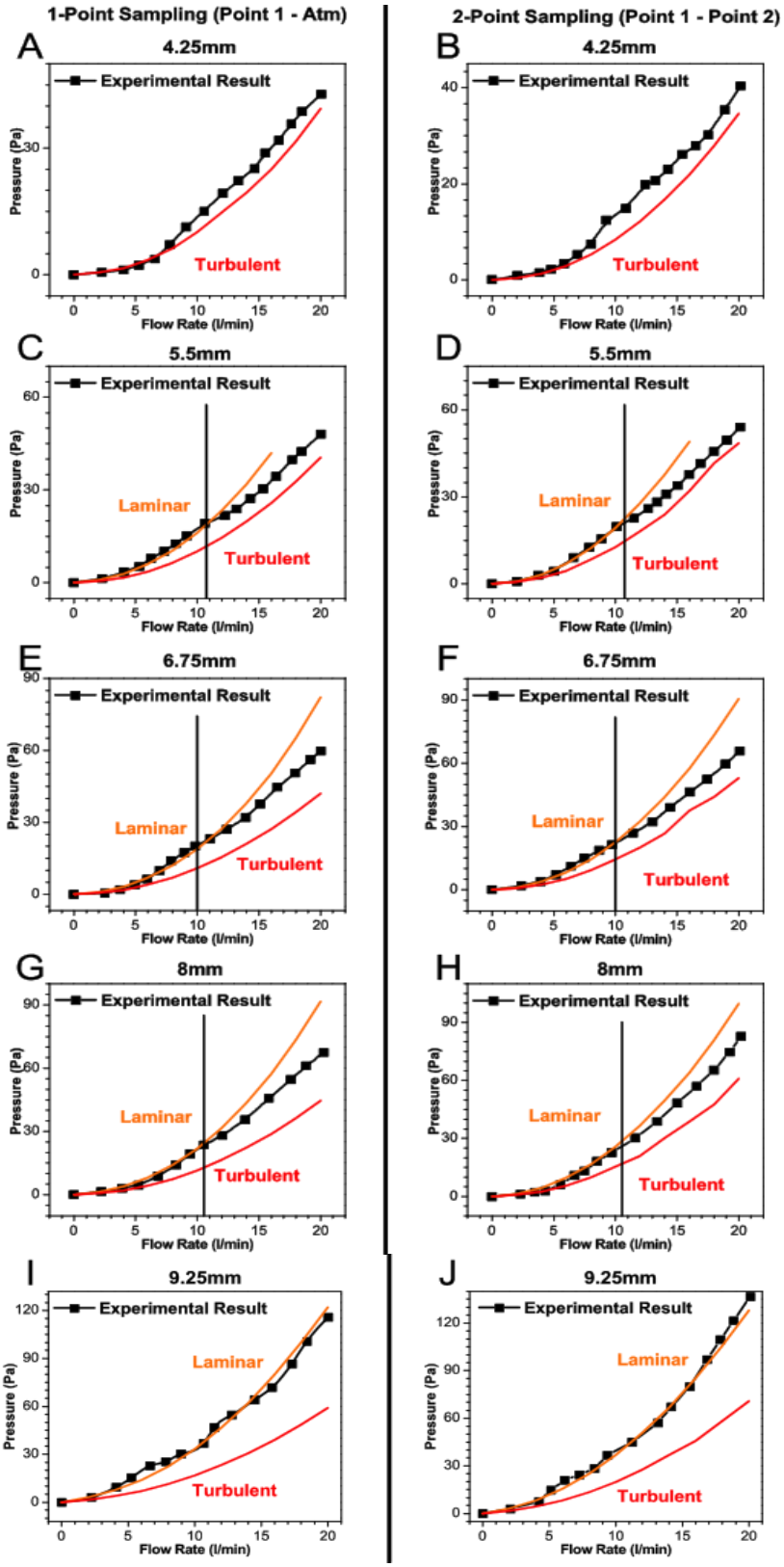
1-Point Sampling (Point 1 - Atm)
2-Point Sampling (Point 1 - Point 2)
A
4.25mm
B
4.25mm
C
5.5mm
D
5.5mm
E
6.75mm
F
6.75mm
G
8mm
H
8mm
I
9.25mm
J
9.25mm
Experimental Result
Laminar
Turbulent
Pressure (Pa)
Flow Rate (l/min)

Figure 2-4. (A-J) Flow calibrations (differential pressure vs. flow rate) as compared to simulated results (laminar and turbulent model), either sampled at pressure port 1 (center of the disk) and atmospheric pressure (right side), or two pressure ports 1 and 2 (left side) (see Figure 2-1 C-D and Figure 2-2 for reference).

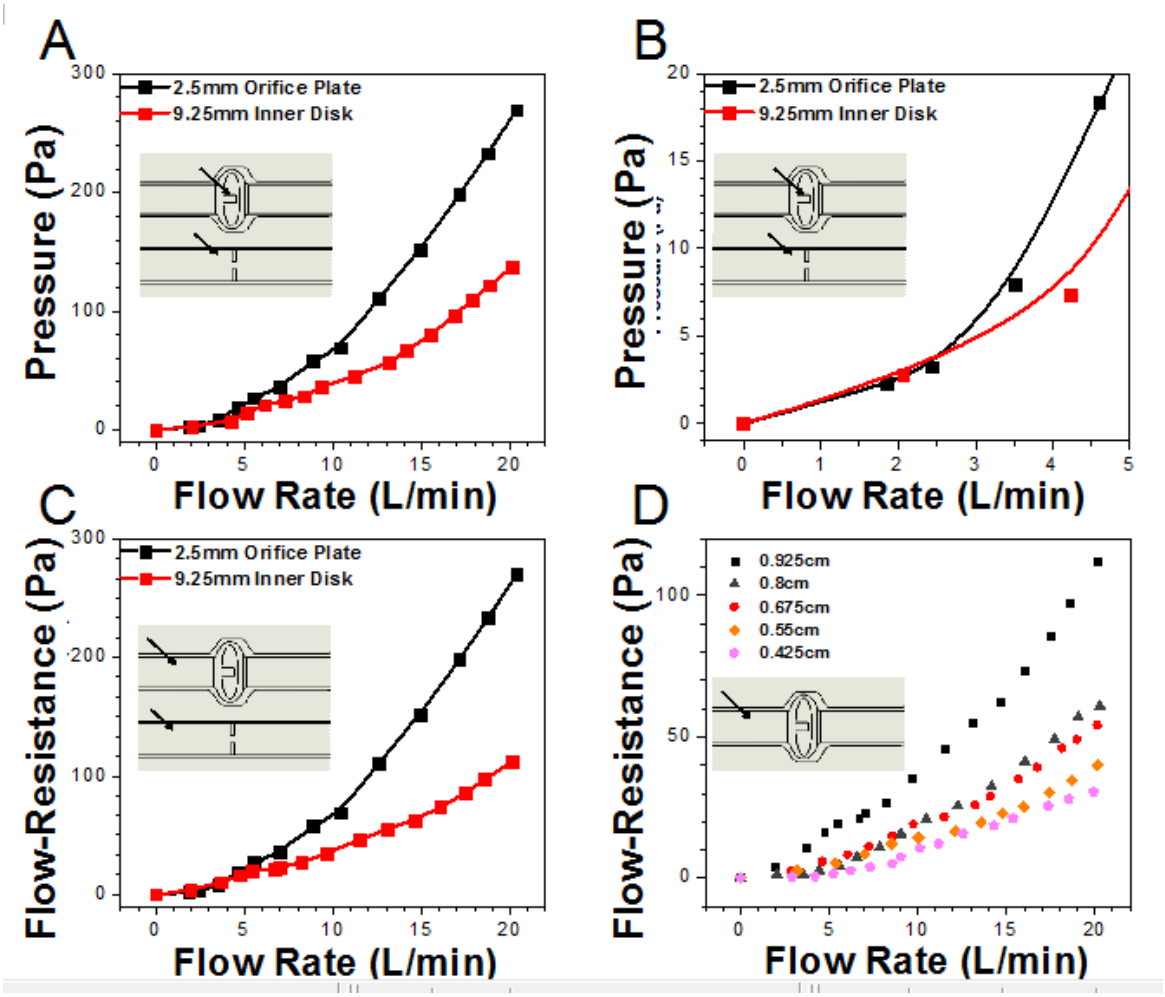

Figure 2-5. Comparative differential pressure vs. flow rate plots for a Confined Pitot Tube flow meter (9.25mm) and a Fixed Orifice (2.5-mm radius). (A) Comparison of pressure signal from 0-20 L/min. (B) Comparison of pressure signal from 0-5 L/min. (C) Comparison of flow-resistance from 0-20 L/min. (D) Comparison of flow-resistance between disk sizes from 0-20 L/min.

Figure 2-5 A-B show the differential pressure measured by a two-point sampling method vs flow. At low flow rates of less than 3L/min, the sensitivity given by the differential pressure of either device is similar (Figure 6B). At higher flow rates, higher differential pressure signal is observed for the fixed orifice flow meter. However, the higher sensitivity comes with a higher flow-resistance, as seen in Figure 6C. At 20L/min, although the fixed orifice meter has roughly 2 times the signal, it also has nearly 3 times higher in flow-resistance. The resistance generated by the Fixed Orifice scales considerably higher than the resistance generated by the Confined Pitot Tube. This point is of interest for breath flow meter measurements that require free-breathing or low flow-resistance such as capnography[9]. The Confined Pitot Tube flow meter has considerably less flow-resistance than the Fixed Orifice meter, while still offering the same sensitivity to low flows (<3 L/min), which are of physiological interest in relaxed breathing conditions[9].

Figure 2-5 D shows the flow-resistance for the Confined Pitot Tube having different inner radii. Although the 9.25mm disk yields a low flow-resistance, the flow-resistance could be further decreased using smaller inner disks if necessary for measuring other types of high flow-rate breathing tests, such as spirometry[54].

2.2.5 Dynamic Flow Tests and Validation in Human Breathing

Given the advantages of the 9.25-mm disk Confined Pitot Tube flow meter as candidate of choice for breath flow meter, the meter was calibrated using a lung calibrator/simulator

as reference flow using the method described in the experimental section. The use of the calibrator/simulator was essential to simulate intended use conditions of exhalation and inhalation. One-point sampling method was used (center of the disk against atmospheric pressure) in the Confined Pitot Tube flow meter since a notable enough advantage was not seen with respect to two-point sampling method. Figure 2-6 shows the comparison between the measured differential pressure in the Confined Pitot Tube and the reference flow. It is worth noticing that the square root of the measured differential pressure in the Confined Pitot Tube flow meter scales linearly with the reference flow in certain regimes. However, there is no single square root relationship in the entire range of flow rates; therefore, a set of equations of differential pressure vs. flow rate were used to calibrate the system at different flow ranges. This practice of piecewise calibration is appropriate for most applications considering that the current computing power of smartphones and even microprocessors allow for very fast signal processing. For the present work, five linear equations relating the square root of the measured differential pressure to the flow rate were used. For commercial implementation, this could be further enhanced or simplified to a larger or smaller number of equations depending on the accuracy requirements of the flow metering application.

Once the Confined Pitot Tube was calibrated, real breath samples were measured simultaneously using the Confined Pitot Tube and a reference flow measurement (Oxycon Mobile). The accuracy was assessed by comparing the total volume of

individual inhalation and exhalation cycles from the integration of the flow measured by both methods. Volume was used to assess compounded errors. In Figure 2-7 A, a strong correlation is noted between the breath volumes from the Confined Pitot Tube and reference flow meter for expired and inspired volumes. An offset between the two measurements is observed due to the aforementioned problems with the calibration method, such as leaks in the lung simulator system as the flow rate increased (see experimental). In order to combat this, a linear regression was computed and used to apply a linear correction. After applying a linear correction, the standard deviation between the two methods was about 50mL, which happens to be the reported accuracy of the reference method; and the overall accuracy error is <10%.

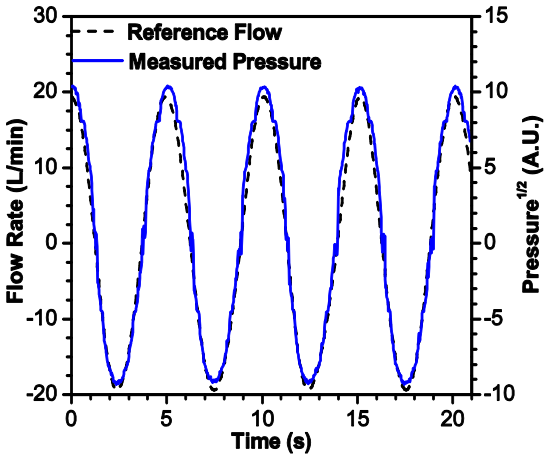

Figure 2-6. Comparison of the reference flow rate (dashed, left axis) and the lung calibrator/simulator, and the square root of the measured differential pressure (solid, right

axis) from a Confined Pitot Tube flow meter. The samples were taken at 40 Hz with no filtering.

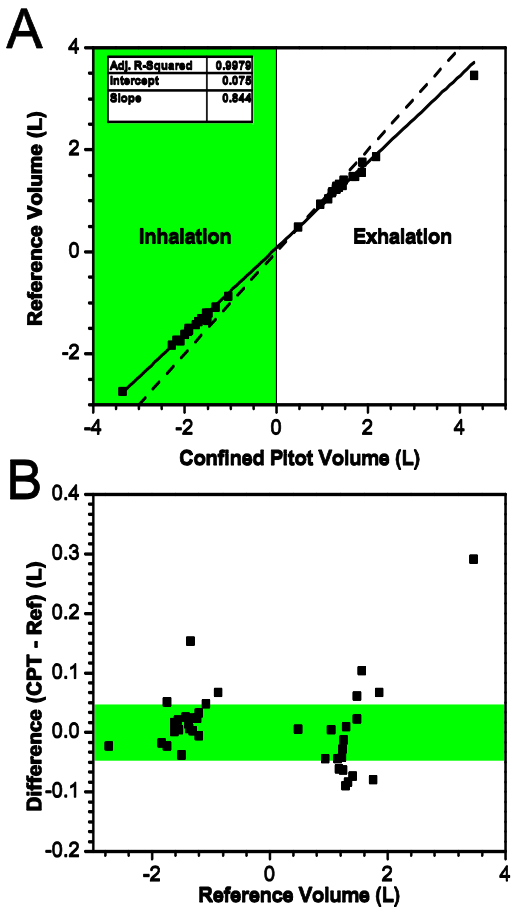

Figure 2-7. (A) Comparison of volumes measured from real breath between the Confined Pitot Tube (CPT) flow meter (9.25 mm inner radius disk) and a reference method (Oxycon). The dotted line represents the ideal 1:1 relationship, and the solid line represents a linear regression of the actual results. (B) Difference between measured volumes of the Confined Pitot Tube and the Oxycon system. Confined Pitot Tube

measurements had a linear correction applied. The shaded area represents the standard deviation of the measurement difference, and the reported error of the Oxycon unit at low volumes (50mL).

2.3 Sensing Chamber Design

The sensing chamber of the device was designed in Solidworks[tm] with two main design goals: To optimize the flow patterns in the device and to reduce effects from ambient lighting. The optimization of the flow patterns mainly consisted of ensuring that the surface of the sensor is as close to the flow stream as possible. Ambient light protection is performed by designing the channels to reject light not from the LED and prevent light ingress into the chamber.

2.3.1 Flow Optimization

Previous works have demonstrated the importance of the physical design on the transport of analyte to the sensor in this system[55]. As can be seen in Figure 2-8 A and B, one major factor is the depth of the sensor within the chamber. With increasing depths, of course the time for the sample to reach the sensor increases. In order to avoid these effects, the sensor in the current design is placed with essentially no offset from the flow tube, as can be seen in Figure 2-8C. Additionally, the flow tube has a bend which directs flow more directly to the surface of the sensor, to ensure a more rapid transit of species to the surface. By designing the flow system as such, we ensure that the sensor is exposed to a representative sample in the device and that the settling time of the system is not diffusion-limited.

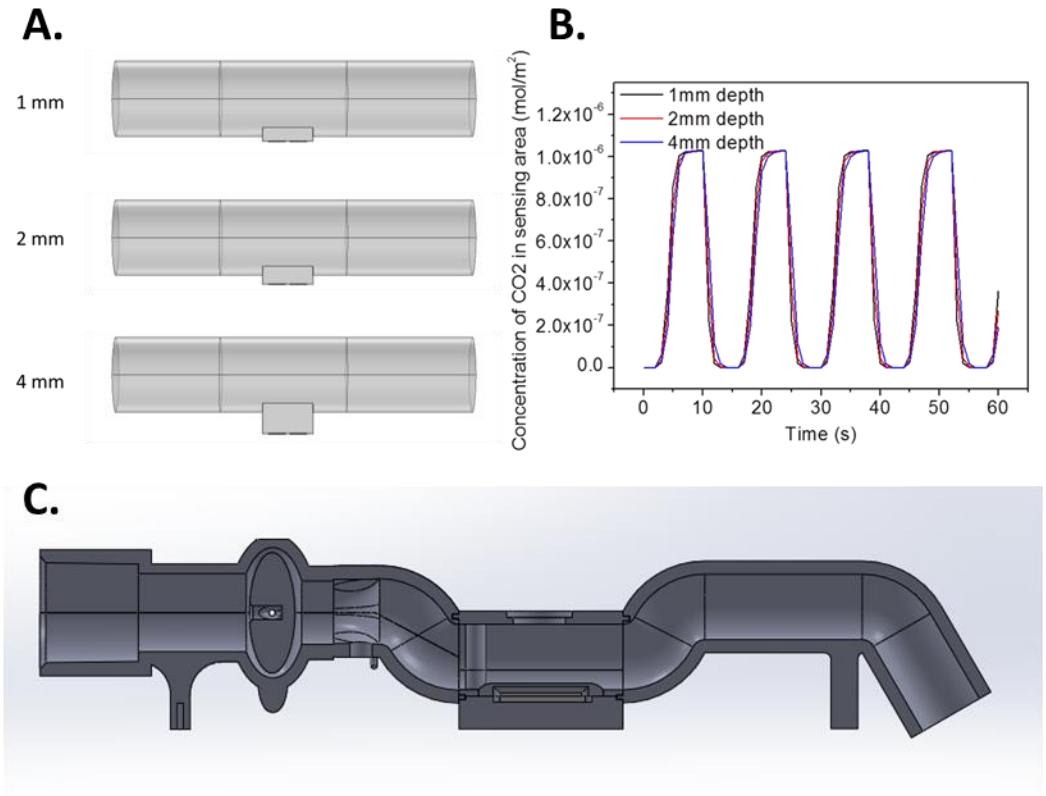

Figure 2-8. A&B represent previous work demonstrating that the depth of the sensor relative to the flow tube has a significant effect on the transport of species to the sensing surface[55]. C is a sketch of the current flow tube and sensing chamber showing the bent-tube design and the sensor position at a negligible depth relative to the flow tube.

2.3.2 Ambient Light Protection

With a colorimetric platform, light ingress is also an issue. The system is designed with three main measures to combat this. The first is the bent-tube design. This makes light ingress from the flow tube itself minimal, as it restricts any direct light path, as can

be seen in Figure 2-8 C. The second measure is to have deep channels in the base of the sensor chamber. These channels help to reduce the impact of light interference by rejecting reflected light. The third measure is the use of a reference photodiode in the device, which allows for corrections for any ambient lighting that does make it into the device. An experiment was performed to show verify the performance of two of these measures; no correction is applied during the experiment for ambient light. The test was simple, the device was switched between two positions: upright (as pictured in Figure 2-8C) and sideways (with the face shown in Figure 2-8 C facing upwards). As can be seen in Figure 2-9, the effect of the shifts does produce a noticeable change in the signal, but the effect is very small compared to changes over the course of an actual test.

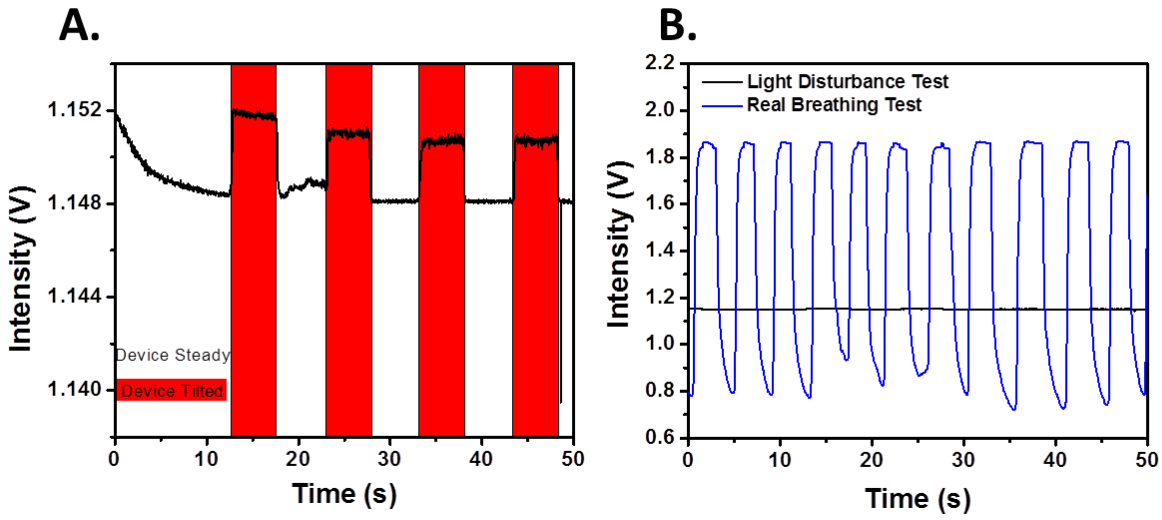

Figure 2-9. Ambient light disturbance tests. Part A shows the signal from the device with a blank sensor. The white sections are the device sitting upright, and the red areas

indicate times when the device was overturned with the sensor port facing indoor lighting sources. Part B shows the same test relative to the changes in an actual breath test.

3 Development of a Colorimetric Carbon Dioxide Sensor

The core of the project is the colorimetric carbon dioxide sensor. The sensing element consists of a solution of m-cresol purple, glycine, and a long chain quaternary amine base coated in a thin film on a porous Teflon membrane. For easy use and minimal production cost, the sensor is manufactured in a simple substrate consisting of laminated plastic, paper, and coated Teflon (see Figure 3-1).

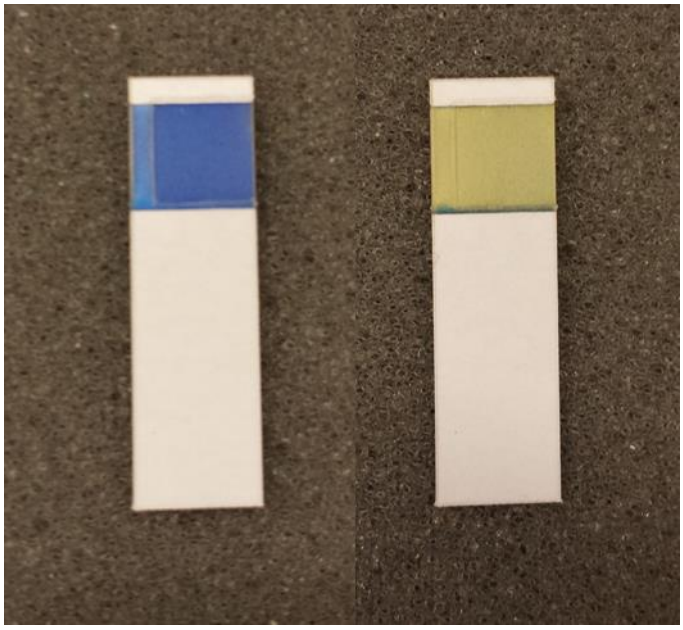

Figure 3-1. The colorimetric sensor. On the left is the sensor without exposure to CO_2 and on the right is the sensor while exposed to CO_2.

3. 1 Sensor Fabrication

The sensor is fabricated in a manner that is simple, consistent, and efficient. Sensors are manufactured in sheets of 210 sensors. Strips of the sensing probe are produced by dip coating Teflon strips in a solution consisting of water, ethanol, methanol, n-hexadecytrimethlyammonium hydroxide, glycine, and m-cresol purple. After coating, the sensors are left to hang dry in ambient conditions. Meanwhile, a laminating sheet and paper stencil are laser cut to the proper specifications (see Figure 3-2 A). Once the strips are dry, they are arranged in the matrix and laminated (see Figure 3-2 B). The paper stencil provides a channel for the Teflon strip, which results in a simple and easy method for ensuring accurate lamination. After the sheet is laminated, it is then laser cut in to individual sensors. The sensors are then packed with desiccants and ready for use.

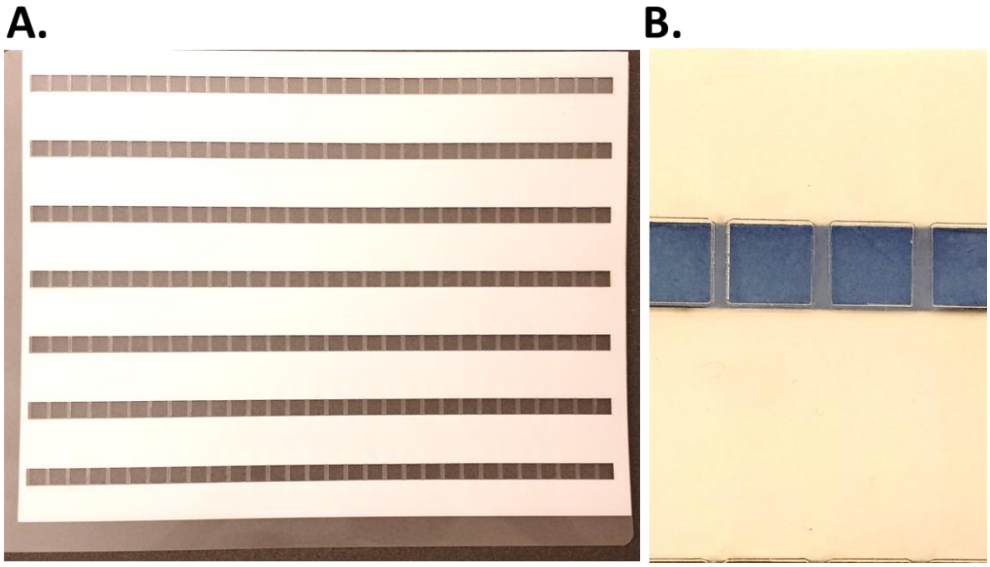

Figure 3-2. The assembly matrix. A laser-cut paper stencil and laminating sheet assembled (A) and a close up of a section with the coated Teflon in place (B).

3.2 Sensor Chemistry

The chemistry of the sensor relies on several components. The main component is the sensing pH dye, m-cresol purple, which acts as a buffer and provides a change in transmittance relative to the concentration of carbon dioxide. In order to sense carbon dioxide, two main elements are used: Hexadecyltrimethylammonium hydroxide is used as a phase transfer agent and base while glycine is used as a buffer and reactive element. Quaternary ammonium hydroxides are commonly used in CO_2 sensors due to their ability to interact with hydrophobic materials and CO_2[56-60].

Colorimetric sensors are based on a dye that is sensitive to some property being altered by the chemical being monitored. In our case, carbon dioxide will alter the pH of

the sensing environment, which will then change the protonation state of the dye and in turn give a change in color (see Figure 3-3). The color change can be measured as a transmittance at a relevant wavelength. For our system, we use m-cresol purple as the sensing dye, as it has many advantages. The dye is highly soluble in water and offers a more optimal pKa for detecting CO_2 than other pH dyes. A more optimal pKa is beneficial for obvious reasons, and being able to use more dye allows for increased reproducibility, greater changes in transmittance with changes in analyte concentrations, more resistance to degradation, and more resistance to sensor saturation.

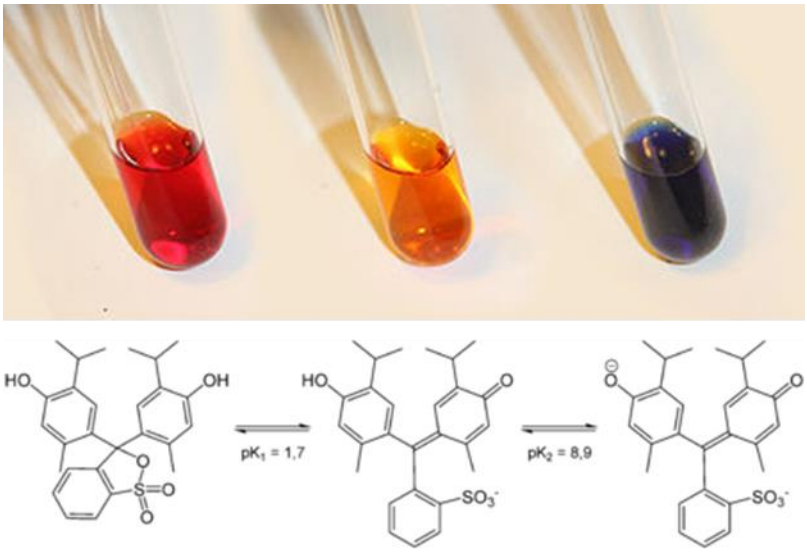

Figure 3-3. A comparison between the three protonation states of Thymol Blue. Color changes are compared on the top vs. protonated forms of the dye on the bottom, which allows for a relationship between the color and pH.

One issue that arises with detecting CO_2 is water content. The targeted reactions with CO_2 detection require water, but accumulation of water will cause dilution, which will greatly alter the sensor response, resulting in a slow sensor which cannot be easily calibrated. In order to combat this effect, this sensor utilizes hydrophobic materials. The thin film sensor is coated on a perfluorinated polymer membrane (Teflon) which can provide resistance to humidity while providing a very high surface area due to its porosity.

In order to increase the pH, increase the effectiveness of the system for detecting CO_2, and to mediate hydrophobic and hydrophilic in interactions on the sensor surface we use hexadecyltrimethylammonium hydroxide. The base is a detergent, which allows for effective CO_2 detection on our hydrophobic surface. The hydrophobic tail interacts with the Teflon membrane while the hydrophilic end interacts with CO_2, our dye, and our amino acid. With this type of chemical environment, we are able to use a humidity resistant sensing substrate and still maintain enough water to carry out aqueous-phase reactions. The quaternary ammonium hydroxide is a weak base, which pushes the pH high enough for optimal CO_2 detection and gives a base for CO_2 to react with by the following reaction:

$$R_4N^+OH^-(aq) + CO_2(g) \leftrightarrow R_4N^+HCO_3^-(aq)$$

This reaction allows for the quaternary ammonium hydroxide to act as a phase transfer agent, reacting with CO_2 in the gas phase and bringing it into the aqueous phase of the

sensor. The last component of the sensor is glycine, which acts as both a buffer and a reactive agent. Glycine has a terminal amine group. Carbamate reactions (reaction between an amine and carbon dioxide) are known to be fast, high yield, and reversible[61]. This reaction and the formation of carbonic acid constitute the main reactions allowing for detection of CO_2 with this sensing element.

3.2.2 Carbonic Acid

Carbonic acid is one of the main reactions of this and most other chemical CO_2 sensors. The reaction consists of dissolved carbon dioxide reacting with water for form carbonic acid, which is dependent on temperature and ionic strength, as seen in the equation below[62,63]:

$$CO_2 + H_2O \leftrightarrow H_2CO_3$$

Although the reaction can be used to measure CO_2 in humid environments, the reaction alone has some major drawbacks in chemical detection. The rate constant for this reaction is fairly low, so it does not react in large quantities.[62,63] Although this can be resolved with using lower amounts of hydroxide and dye, this creates more issues with reproducibility, sensitivity, and variability with humidity. Another issue with this reaction is that it is relatively slow[64,65]. Using this reaction alone, a real-time, accurate, and reliable sensor for CO_2 in breath is incredibly difficult.

3.2.3 The Carbamate Reaction

The main reaction in our sensor is the carbamate formation from the reaction of CO_2 and glycine. Carbamate reactions have been measured to be very fast reactions with high yields[61,66]. The reaction can be summarized as follows:

$$C_2H_5NO_2 + CO_2 + H_2O \leftrightarrow C_3H_4NO_4^- + H_3O^+$$

This reaction allows for our sensor to reach much lower settling times and have a more reliable output.

3.3 Sensitivity

In order to evaluate the accuracy of the sensor, the shape of the calibration curve, and the reproducibility of the sensor, breathing conditions were simulated in a setup where the only major variable is the CO_2 concentration. The setup consists of pre-made bags of dry CO_2, which are pumped through a heated water bath. By keeping the water bath at 35 Celsius, we can get a humidity-saturated gas sample at roughly 33.5 Celsius. The sample is then switched between the simulated gas stream and ambient air by switching pumps, see Figure 3-4.

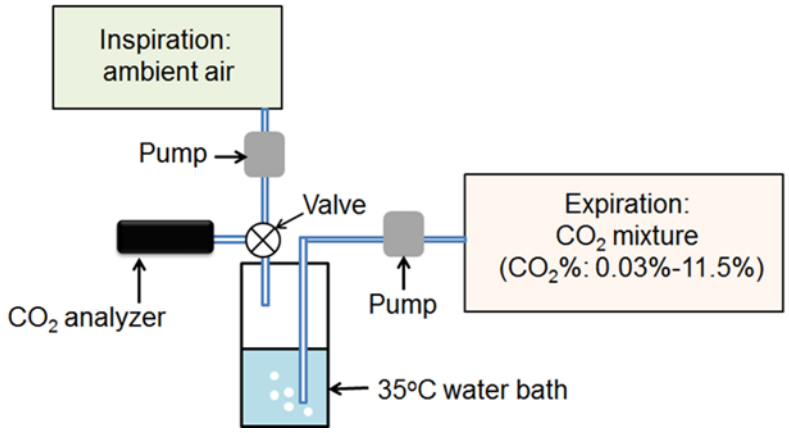

Figure 3-4. The artificial breathing setup used to simulate breathing. CO_2 bags are prepared for the setup using a commercially available sensor, the gas from the bag is bubbled through a heated water bath to humidify the gas, and then the gas is pumped through the capnography device. In order to simulate inhalation, another pump is used to pump in ambient air, and the two pumps are switched in 5 second intervals.[55]

During this artificial breathing test, the sensor was held at about 35 Celsius. This is a condition that we also use during actual breathing tests that helps to minimize temperature fluctuations during the test. Below, in Figure 3-5, the 35C calibration curve can be seen. The relationship can easily be represented as an exponential relationship, which gives us a shape to fit to with real-breath tests. This calibration leads to a relative deviation of roughly 6%, which is too high for breath analysis. The error of this method comes from a few sources. First, the simulated breathing setup does not very effectively remove humidity during the test, which leads to accumulation of water on the sensor.

Second, the output concentration of CO_2 is not constant from the setup. The water will absorb some of the gas being passed through, leading to increasing CO_2 over time. Third is human error. The setup relies on careful timing, which can be difficult with manual switching.

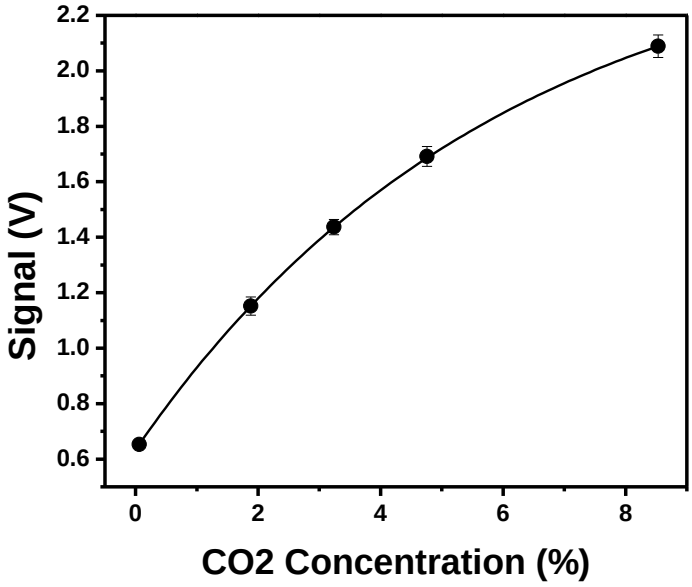

Figure 3-5. A calibration curve of our sensor from the artificial breathing setup using 5 different sensors with the sensor held at 35 C.

3.4 Sensor Selectivity

In order for the sensor to be accurate in human breathing conditions, it needs to be selective to carbon dioxide in breath. The sensor has been tested with high concentrations of the most prevalent chemical species in human breath. Overall, it was found by Dr. Di

Zhao that the sensor, when exposed to any of the major components of breath, shows a minimal response to potential interferants. Considering that the results for all five potential interferants give the same response, it might even be safe to infer that the result seen is due to a baseline effect of switching flows and that the actual interference from the species might be smaller.

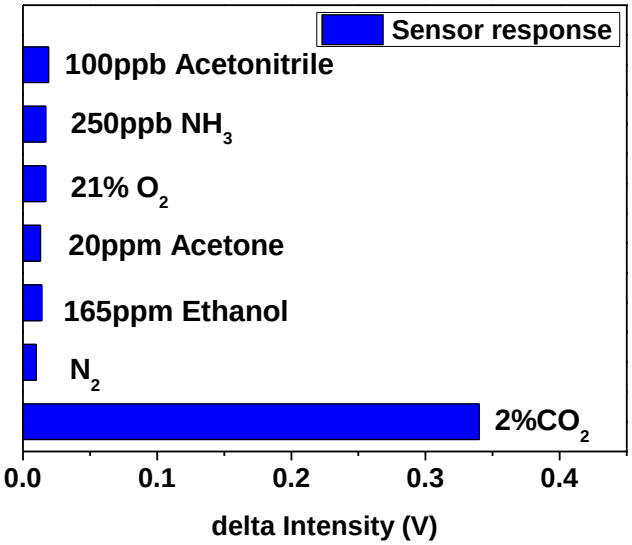

Figure 3-6. A selectivity test comparing our signal with carbon dioxide to 5 of the other most prevalent species in human breath. The test demonstrates that interferants in breath should not have a significant effect on the carbon dioxide reading.[55]

3.5 Sensor Stability and Reproducibility

Tests were performed to evaluate the shelf life of the sensors and the overall reproducibility of the production process. In order to evaluate these, an aging test was

performed on a freshly produced batch of sensors (N = 100), where the sensors were stored at an elevated temperature and tested periodically. The tests were performed using the same artificial breathing setup as described above at 4% CO_2, and the sensors were stored in sealed Mylar bags with a molecular sieve desiccant at 45C. It is shown in Figure 3-7 A that after day 1 (non-aged baseline test), there is an increase in the dispersion of the tests, but after that the dispersion does not rise significantly and that the average values do not change much over time.

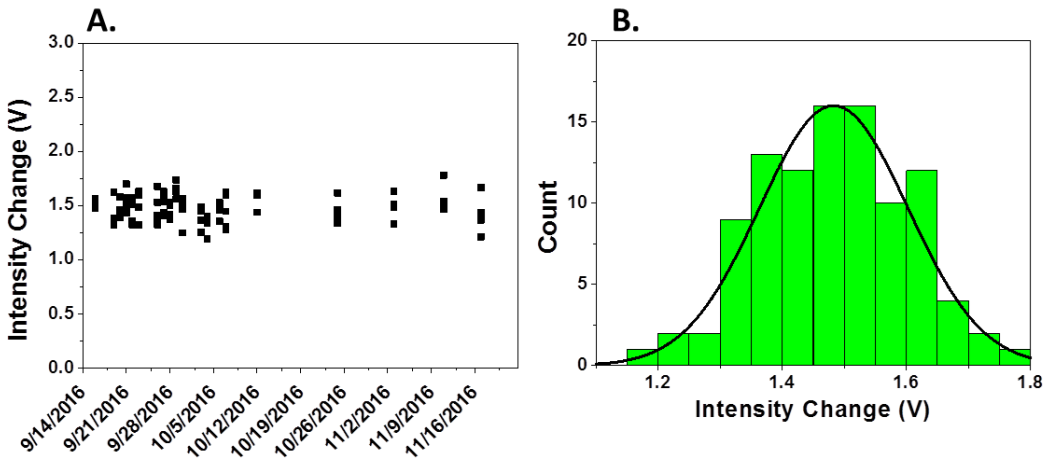

Figure 3-7. A. The results of the stability test showing the change in intensity of the sensors in response to artificial breathing conditions (4% CO_2, same setup as above). B. A distribution of values from part A.

In addition, in Figure 3-7 B we see a normal distribution of intensity changes for the same test. The width of the distribution is something that can be worked with in order to get accurate testing, considering that most of the variance can be accounted for via

calibration during the test (see below). In addition, day to day changes can be seen in Figure 3-7 A, indicating that a certain amount of the variance is likely introduced by the test itself, rather than the sensors.

3.6 Detecting Carbon Dioxide in Human Breathing

Above it is demonstrated that the sensor is sensitive to CO_2 in moist environments and stable over time in dry conditions. The most important condition is human breathing, which introduces new challenges. The main challenges are how to provide a user-friendly calibration, how to account for temperature changes with complex patterns, and how to transduce the transmittance to a CO_2 signal in real time. In order to evaluate this, we use a high-resolution side-stream CO_2 analyzer simultaneously with our device. The side-stream detector used is a Vacumed Silver CO_2 analyzer, which can provide a response time below 250ms and a resolution of 0.01% CO_2, although the accuracy is difficult to assess in actual breathing tests.

3.6.1 Signal Intensity Vs. CO_2 Concentration

The most important relationship is that between the concentration of CO_2 and the intensity output of the sensor. In Figure 3-5, it can be seen that the sensor follows an exponential relationship. Figure 3-8 shows an actual breathing test from a normal subject vs. the raw signal from our device, both measured simultaneously. The test starts at a time of roughly 10 seconds; the earlier part of the test is omitted for clarity. It can be seen

that the raw signal alone does not reflect changes in the end-tidal correctly, does not have accurate slopes in the alveolar plateau, and does not accurately reflect minute features.

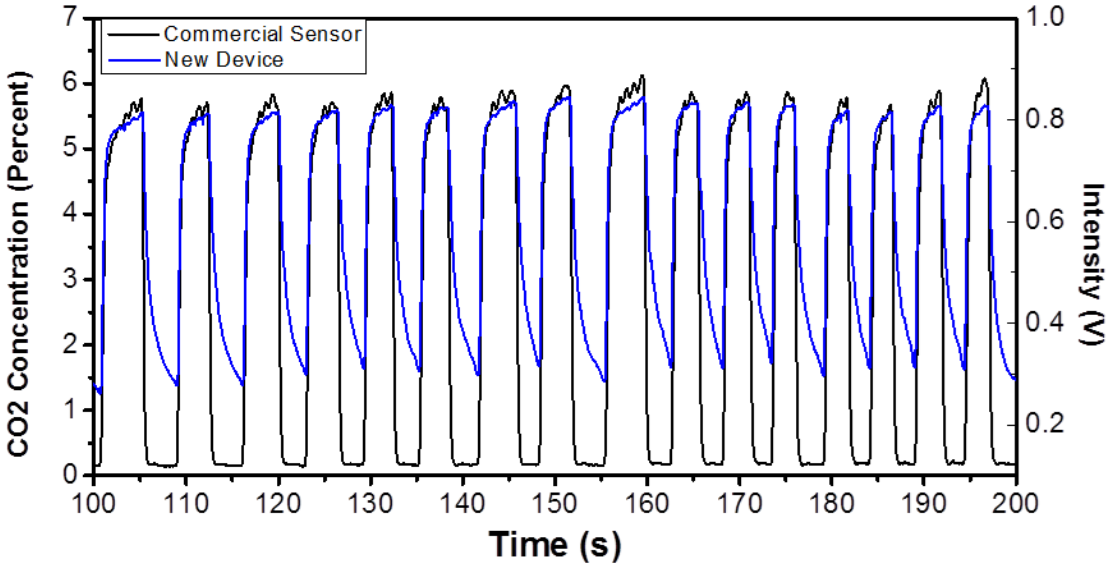

Figure 3-8. A comparison between the commercial device and the raw signal from the colorimetric device for normal breathing. Note that the details seen in the end-tidal portion of the commercial device are not well reflected in the new device's signal.

From tests on the artificial breathing, it can be seen that the sensor calibration follows an exponential relationship. Since the relationship is exponential, within a certain range we can linearize the calibration by raising it to some power, in this case for our range 2.7 works well. Knowing that, we can infer that with real human breathing the calibration will follow a relationship of the form:

$$[CO_2] = A * (V - B)^{2.7}$$

where the concentration of CO_2 is proportional to some constant A, multiplied by the signal (V) minus some variable B which is raised to the 2.7^{th} power. This model can be worked out such that A is constant between tests, and then B is a variable subject to calibration. Figure 3-9 shows the comparison of readings from the commercial unit and our device after application of the equation above, with a difference left between the two for illustration. When comparing the two traces there are a few noteworthy features: First is that with the calibration, end-tidal values begin to change proportionally between the two methods. Second is that minute features begin to look similar between the two methods. Third is that the slopes of the alveolar plateaus are still dissimilar. The reason for this difference is that during exhalation and inhalation, the sensor is subject to temperature changes.

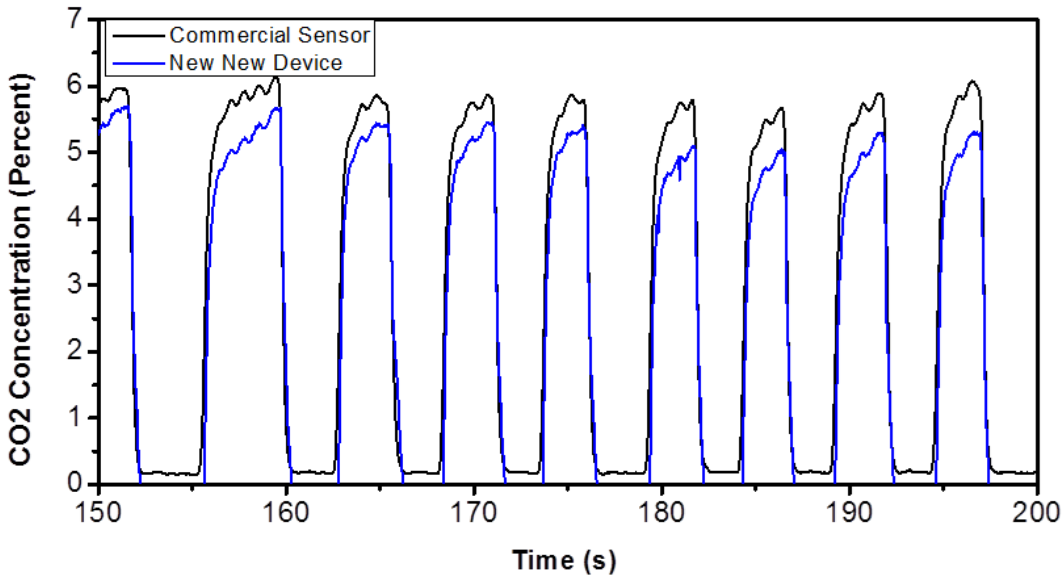

Figure 3-9. A comparison between the commercial sensor and the signal from the colorimetric device with parameters applied for the slope of the raw signal only (excludes corrections for temperature and baseline).

3.6.2 Temperature Corrections

The chemical sensor is very sensitive to temperature, which we combat with a heat model. In future designs, we will also heat the sensor to a temperature similar to that of exhaled air (~35 Celsius) in order to reduce fluctuations. By heating the sensor, we will be able to greatly reduce the range in which the sensor temperature shifts during a test, although we do still have temperature fluctuations due to inhalations. Since the sensor is a thin film, it cannot be measured via a contact method, such as a thermistor. In order to account for changes in the temperature of the sensor, an empirical temperature

accounting method has been developed. Figure 3-10 shows a number of temperature effects that must be accounted for in the system.

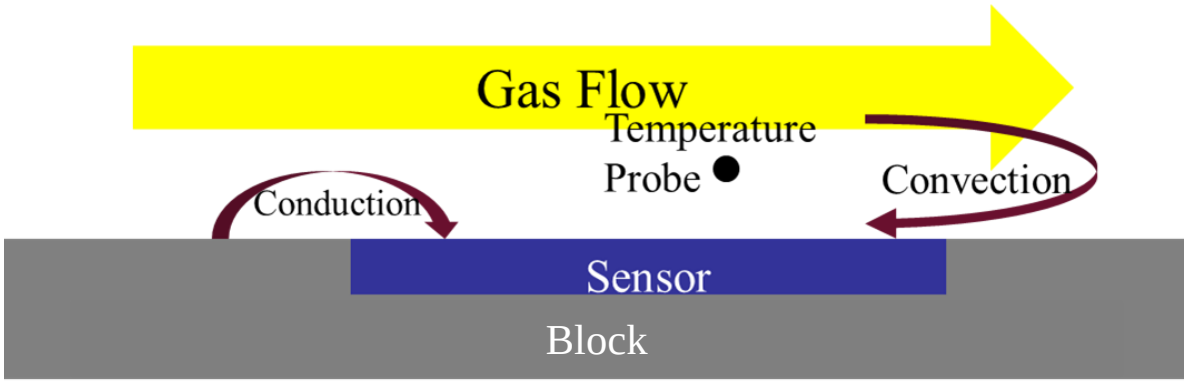

Figure 3-10. An illustration showing the main heat transfer phenomenon governing the sensor's temperature. The gas flow represents both inhaled and exhaled breath, as both are passed over the sensor and therefore over the temperature probe.

For building a temperature accounting model, we can start with Fourier's Law and Newton's law of cooling, which can be stated as such in 1 dimension:

$$Q = k * A * \Delta T = k * (T_{Block} - T_{Sensor})$$

and

$$Q = h * A * \Delta T = h * A * (T_{Gas\ Stream} - T_{Sensor})$$

respectively, where Q is the sensor heat flux, k is the conductive heat transfer coefficient, h is the convective heat transfer coefficient, A is the surface area, and T is the temperature of the respective system. By combining the two equations, we get:

$$Q = k * A * (T_{Block} - T_{Sensor}) + h * A * (T_{Gas\ Stream} - T_{Sensor})$$

which can be further worked to:

$$\frac{d(m * C * \Delta T)}{dt} = m * C * \frac{dT_{Sensor}}{dt}$$

$$= k * A * (T_{Block} - T_{Sensor}) + h * A * (T_{Gas\ Stream} - T_{Sensor})$$

since:

$$Q = \frac{d(m * C * \Delta T)}{dt} = m * C * (T_{Sensor} - T_{Standard\ State}),\ T_{Standard\ State} = 0$$

where C is the specific heat capacity, applying 0 degrees as our standard start for simplicity. The equation can be expressed numerically as:

$$m * C * \frac{T_{sensor,i+1} - T_{Sensor,i}}{\Delta t}$$

$$= k * A * \left(T_{Block,i} - T_{Sensor,i}\right) + h * A * (T_{Gas\ Stream,i} - T_{Sensor,i})$$

where the ith term corresponds to the current time, the i+1th term corresponds to the next iteration, and Δt represents the time step size. The equation can be further simplified to the explicit equation:

$$T_{sensor,i+1} = \frac{\Delta t * A}{m * C} * \left(k * \left(T_{Block,i} - T_{Sensor,i}\right) + h * \left(T_{Gas\ Stream,i} - T_{Sensor,i}\right)\right) + T_{Sensor,i}$$

and further simplified to an empirical form:

$$T_{sensor,i+1} = D * \left(T_{Block,i} - T_{Sensor,i}\right) + E * h(v) * \left(T_{Gas\ Stream,i} - T_{Sensor,i}\right) + T_{Sensor,i}$$

where D is a simple variable representing conductive heat transfer, E is a variable accounting for part of the convective heat transfer, and h(v) is a variable representing the convection as a function of fluid velocity (v). The volumetric flow rate measured by the device, so the general shape of the relationship can be summarized with a generic equation for the convective heat transfer coefficient for air[67]:

$$h(v) = 10.45 - v + 10 * \sqrt{v}$$

which leads to a final equation for the temperature for conduction and convection:

$$T_{sensor,i+1} = D * \left(T_{Block,i} - T_{Sensor,i}\right) + E * \left(10.45 - v + 10 * \sqrt{v}\right) * \left(T_{Gas\ Stream,i} - T_{Sensor,i}\right) + T_{Sensor,i}$$

After generating an equation for the temperature of the sensor, two questions still remain: How are the D and E factors determined and how is this translated to the sensor reading. This is performed by first making an assumption that the relationship between

the sensor temperature and the sensor reading is linear and setting our reference temperature to be breath temperature, or about 35 Celsius. With that, we can model sensor deviation due to temperature as follows:

$$T_{Correction} = F * (35 - T_{Sensor})$$

where F is a generic correction factor. Combining this with the calibration equation, we get the final form of the equation used to convert the reading from the device into a CO_2 concentration:

$$[CO_2] = A * (V - B)^{2.7} + T_{Correction}$$

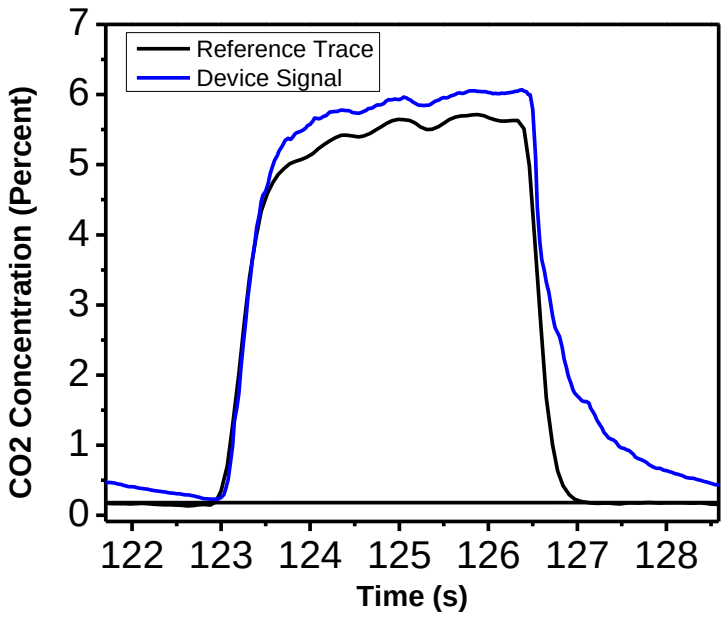

Figure 3-11. A breathing waveform with the calibration equation applied and temperature correction applied. The vertical offset is left for better illustration.

Using these equations, for a single breath waveform we can get something like in Figure 3-11. Unfortunately, this model still neglects a large factor which complicates the signal greatly: humidity. During the course of breathing, the sensor is subject to large swings in relative humidity. Since the sensor is hygroscopic, during the test it will be absorbing and releasing water, which results in latent heat affecting the sensor during each breath cycle. In addition to latent heat effects, different breathing patterns will produce different equilibrium levels of water on the sensor, which likely have an effect

on the sensor due to the pH dependence. A new model has since been constructed, as outlined in section 3.7: Temperature and Humidity Accounting in Breath.

3.6.3 Sensor Calibration

In order to calibrate a colorimetric sensor, either the intra-batch reproducibility needs to be high enough for a calibration to stand across an entire batch or there needs to be some feature in a test that can be used to calibrate the sensor in-situ. Due to variance introduced in the aging process, our sensor utilizes in-situ calibration. This is generally done via a baseline reading at either the beginning or end of the test, but for this sensor we utilize points that are regularly occurring during the test. Since our sensing platform is based on both inhalation and exhalation, every breathing cycle will contain an adsorption and desorption phase. By looking at the desorption phase, we can gather information about the condition of the sensor, essentially viewing differences between sensors as a one-dimensional degradation. Viewing the sensor properties as such, we can apply the desorption curve to give us a calibration factor (the B-factor in section 3.6.2). By using the minimum of the curve (see Figure 3-12), we obtain a calibration factor that is dependent on: 1. The temperature of the sensor at that point. 2. The water content of the sensor at that point. 3. The extent of inhalation (in the sense of both volume and time).

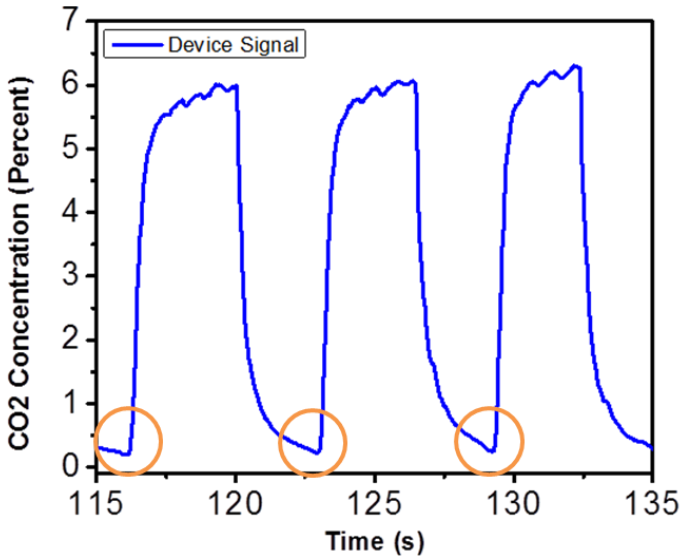

Figure 3-12. A trace of a breathing test with the new device demonstrating the points used for calibration (circled in orange), which are the end of the desorption phase of the breath.

In tests with similar breath patterns, the signal minimum could be used to generate a fairly robust calibration algorithm. As can be seen in Figure 3-13, the signal minimum can be used as a good predictor of the calibration factor of the test. This demonstrates that even though there is a large variance within a batch of sensors, the variance can be accounted for using the inhalation phase of the breathing waveform.

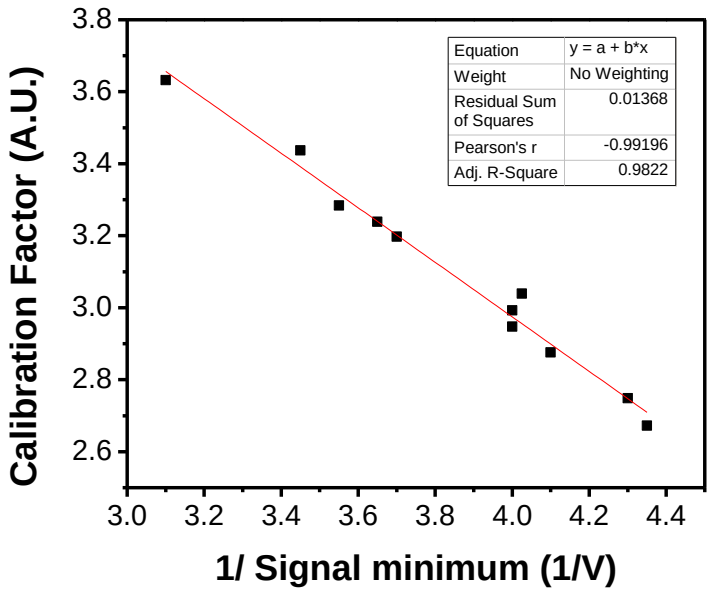

Figure 3-13. A fit comparing the signal minimum from different breathing tests with the calibration factor obtained for each test. The effectiveness was such that the end-tidal carbon dioxide levels could be measured to within 0.15% CO_2 compared to a commercially available unit.

3.6.4 Parameter Measurement in Human Breathing

The device was used with a number of subjects in order to assess its ability to measure capnographic parameters, in this case the End-Tidal CO_2 and the slope of the alveolar plateau. Subjects were asked to breathe normally for 3 minutes for the test, then the calibration algorithm (as described above) was applied and parameters were extracted and compared between the device and the reference method (Vacumed Silver CO_2 Analyzer). The results are shown in Figure 3-14, and demonstrate that the device is

capable of measuring these parameters with fair accuracy. Further improvements will be made using the model developed in chapter 3.7: Temperature and Humidity Accounting in Breath.

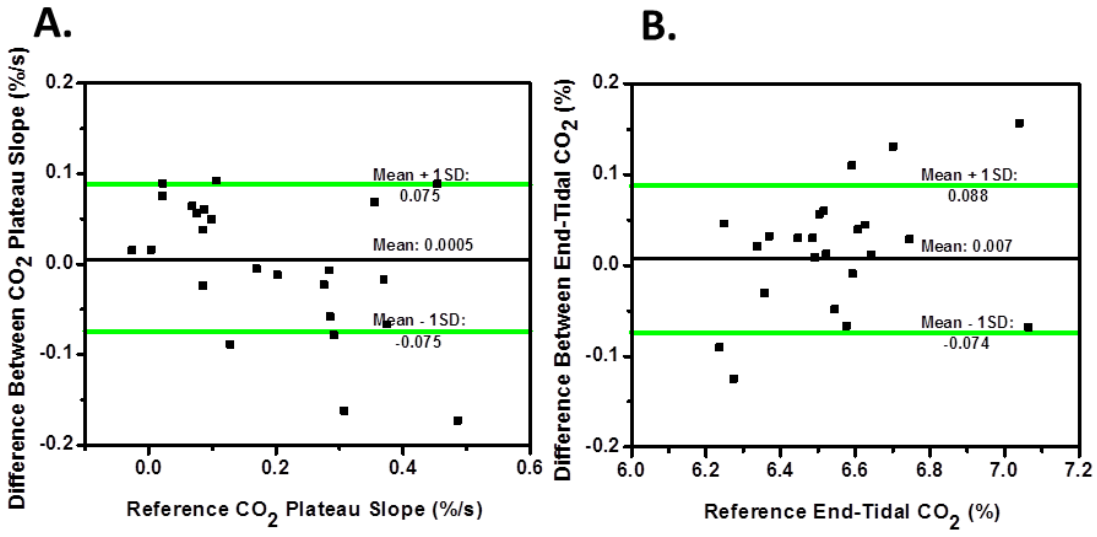

Figure 3-14. A comparison between the new colorimetric device and a commercially available infrared detector comparing measurements for the alveolar plateau (A) and the end-tidal concentration (B).

3.7 Temperature and Humidity Accounting in Breath

In order to accurately account for CO_2 in breath, corrections based on temperature and relative humidity need to be made. In order to develop and apply these corrections, the temperature and water content of the sensor must first be accounted for, which is challenging since as a thin-film sensor, we cannot get an accurate measurement via contact. This was done using the models and constants developed via a thermographic

reference method (Flir A655sc thermal camera) in chapter 4.3, where a discrete model was developed in order to account for temperature changes in terms of conductive and convective heat fluxes as well as heat generation from water interactions.

$$\frac{m * c}{A} * \frac{dT_{Sensor}}{dt} = K * \left(T_{Surface} - T_{Sensor}\right) + H(f) * (T_{Gas} - T_{sensor}) + B * \frac{dC}{dt} \quad (1)$$

$$B * \frac{dC}{dt} = B * (r_{abs} * [C_{Gas}] - r_{des} * [C_{Sensor}]) \quad (2)$$

Equation 1 gives the total heat interactions of the system in 1-dimension, where m is the mass of the sensor, c is the specific heat capacity of the sensor, A is the area of the sensor, T_{sensor} is the temperature of the sensor, t is time, K is the conductive heat coefficient of the system, $T_{surface}$ is the temperature of the sensor-holder, H(f) is the convective heat transfer coefficient of the system as a function of flow (f), T_{gas} is the temperature of the gas passing over the sensor, B is a constant that relates the change in water content to a heat generation term, and C is the water content (in terms of relative humidity). In equation 2, we can further break down the water content portion in terms of absorption and desorption constants (r) and the concentration of water in the sensor and in the gas stream (C). Work in determining the relationships for the conductive and convective terms is detailed in chapter 4.3, "Thermochemical Humidity Detection in Harsh or Non-Steady Environments".

With this equation, an explicit solution can be obtained from easily measured factors in order to determine the temperature of the sensor at the next discrete step in time (25ms in this case). All of the factors can be measured at a fast enough capture rate to

account for changes in a single breath with exception to the concentration of water in the gas stream (C_{gas}). In order to estimate C_{gas}, I can assume that the exhaled gas is at a saturated relative humidity and I can measure the ambient relative humidity. The assumption that exhaled gas is saturated is bolstered by the fact that the exhaled gas cools slightly upon entering the device, and therefore will saturate so long as it is near saturation conditions exiting the mouth. Since flow is being measured in the device, C_{gas} can be determined based on knowns in the device, i.e. whether the gas over the sensor come from and exhalation or inhalation, what the relative humidity levels of each environment are, and what would the relative humidity of that gas be at the measured temperature.

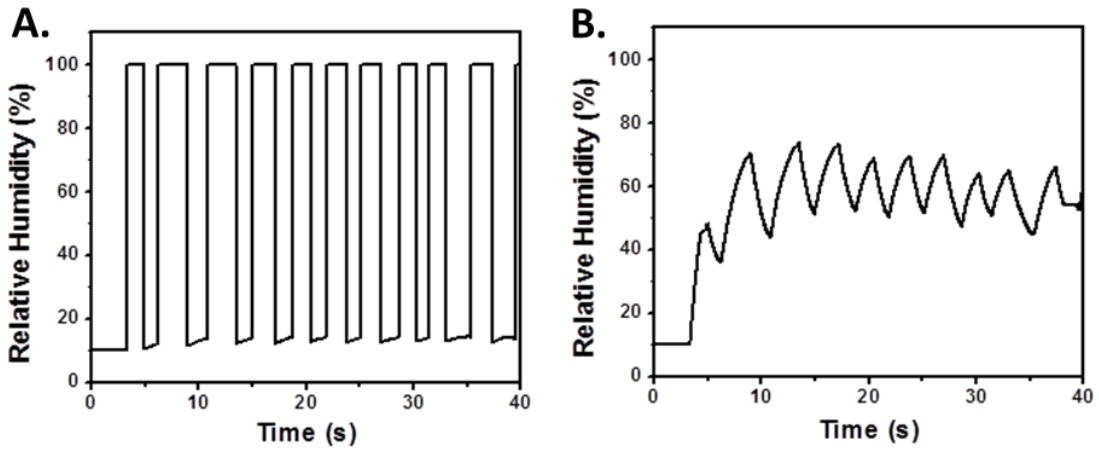

Figure 3-15. A. Calculated relative humidity level of the gas stream through the device during a real breathing test. Note that the exhalations are saturated (100% relative humidity) and the inhalations are calculated based on the temperature of the gas stream

and the ambient relative humidity. B. A convolved gas-stream relative humidity to better represent the effective humidity level being felt by the sensor, as to account for transport and other limitations that are a function of the flow rate.

Applying this logic in a real breath test, the concentration of gas in the device as a function of time, as seen in Figure 3-15A. The test is Figure 3-15A was performed with real human breathing at an ambient relative humidity of about 17%. Note that during the exhalation phases we have saturation conditions (100% relative humidity) and during the inhalation we have variable humidity. This is due to the change in temperature of the gas during inhalation at a constant ambient relative humidity level. In reality, the relative humidity will not have such a sharp pattern as in Figure 3-15A, rather due to transport limitations, mixing in the dead space of the flow channel, and condensation/evaporation of moisture on the walls of the device changes will be slowed. For the sake of having a lightweight and simple model, this can be accounted for with a simple 2-point convolution factor. The convolution operation can be seen in equation 3, and will apply a simple numerical convolution factor (c(f)) as a function of flow rate, where perform a simple convolution operation between the calculated concentration at the next time step ($C_{gas,i+1}^{Calculated}$) and the current gas concentration ($C_{gas,i}^{Actual}$). The convolution factor will be a number up to 1, with 1 representing an infinite flow rate (no transport limitations, effects of condensation/evaporation negligible, dead space negligible) and some low value representing conditions at no flow (natural convection and diffusion is the only

factors of transport). Applying equation 3 to a the calculated relative humidity during a breath test, the result is Figure 3-15B, which represents the effective relative humidity of the gas stream, or essentially what the sensor sees of the gas stream.

$$C_{gas,i+1}^{Actual} = (c(f)) * C_{gas,i+1}^{Calculated} + (1 - c(f)) * C_{gas,i}^{Actual} \quad 3$$

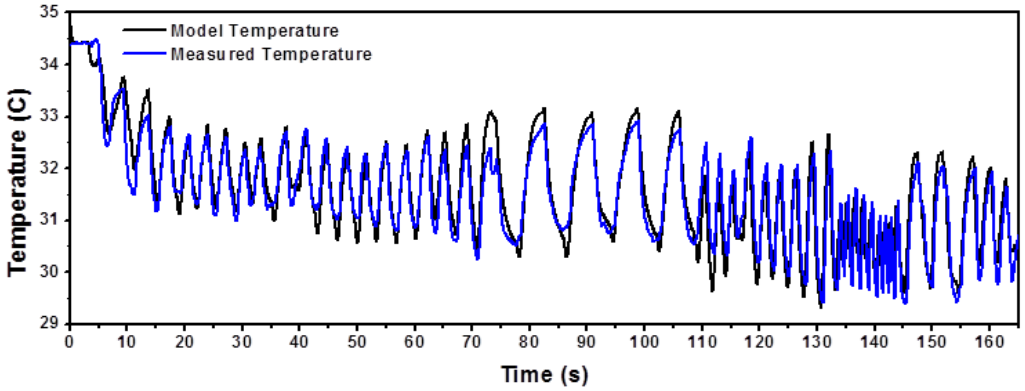

Figure 3-16. A demonstration of the model's performance against temperature measurements from a thermal camera (FLIR A655sc). Note that the main departures are during periods without flow (the two large departures at 40 and 73 seconds).

Using the convolved gas stream humidity value and determining values for the remaining parameters based on breath tests compared against the thermal camera, a model can be built as seen in Figure 3-16. Although the model can predict the temperature with fair accuracy in most portions, the model still has a few flaws. Looking at Figure 3-16, the main issue is that the model does not offer the best response when the flow rate is zero, which took place at 40 and 73 seconds. Overall, the model still needs

additional optimization and a validation in order to ensure that the model accurately predicts the temperature of every breath under every environmental condition.

3.8 Sensor Response Time in Human Breathing

This section introduces validation results for assessment of End-tidal carbon dioxide ($EtCO_2$) concentrations and breathing patterns from the new device. The performance of the new sensor is compared to an infrared carbon dioxide commercial analyzer. Correlation analysis of $EtCO_2$ levels from both methods indicated high accuracy, with a correlation coefficient >0.85. In addition, the capability of the new sensor to discriminate between normal and abnormal breathing patterns was assessed via comparative paired t-test. The overall performance of the new sensor is satisfactory, and opens the possibility of low-cost respiratory analysis for patients with respiratory diseases.

Detection of carbon dioxide concentration is performed by monitoring changes in absorbance between sensing and reference areas via transmittance in our new device. The colorimetric carbon dioxide sensor was calibrated using a commercial carbon dioxide analyzer and a flow sensor. The color sensor was integrated with a flow meter in order to provide both exhalation flow rates and concentrations. The commercial carbon dioxide analyzer, a VacuMed infrared CO_2 analyzer, was used as a reference measurement, and real-time data was recorded via oscilloscope. Data was gathered simultaneously by both methods, providing a real-time comparison between the two methods.

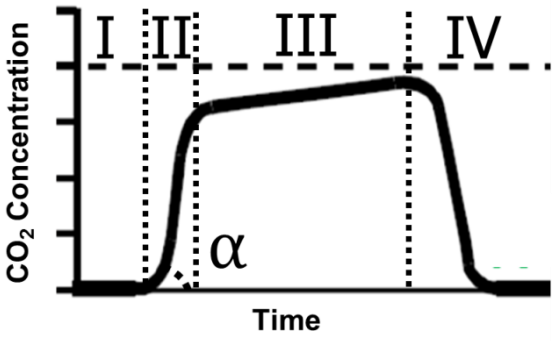

Figure 3-17. A typical CO_2 breathing waveform for a healthly subject. The roman numerals represent different phases of breathing.

Data from the colorimetric sensor was gathered by measuring absorbance as the logarithm of the sensing transmittance over the reference transmittance. The colorimetric sensor signals were used to assess both, end tidal carbon dioxide concentrations ($EtCO_2$) from the calibration, as well as CO_2 patterns, which resembled that shown in Figure 3-17 (see more details below). Beginning exhalation slopes were taken as the maximum time derivative over 50 points (1.25 seconds) in the beginning exhalation phase of the breath, and analyzed in comparison with those exhalation slopes defined under similar conditions from the commercial analyzer.

As Figure 3-18 shows, the colorimetric sensor can assess end-tidal CO_2 levels with a correlation close to 1, and squared-correlation coefficient (R^2) equal to 0.875 using simply the change in voltage from the device (no models). Although we do have correlation, the aforementioned models provide a much higher accuracy. Although end-

tidal CO_2 levels can be useful, waveform characteristics are also an important tool in assessing respiratory and gas-exchange functions.

Table 3-1. A comparison of response times (90%) between devices

	New Colorimetric sensor	Commercial analyzer	Existing colorimetric sensor
90% response time (ms)	150	250	2000

A typical CO_2 waveform in a healthy individual will generally have a shape similar to that shown in Figure 3-17, and four phases (I-IV), two of them for exhalation (II and III), and the other two for inhalation (I and IV). Phase I corresponds to exhalation from the previous breath before the breath cycle of interest. Phase II reflects the CO_2 concentration in the dead space of the lungs and the beginning of CO_2 alveolar release. Phase III corresponds to the alveolar CO_2 in the lung, which rises in concentration through the breath. With abnormal lung function come differences in the slopes of phase II and III of the waveform, along with difference in the $EtCO_2$ concentration.

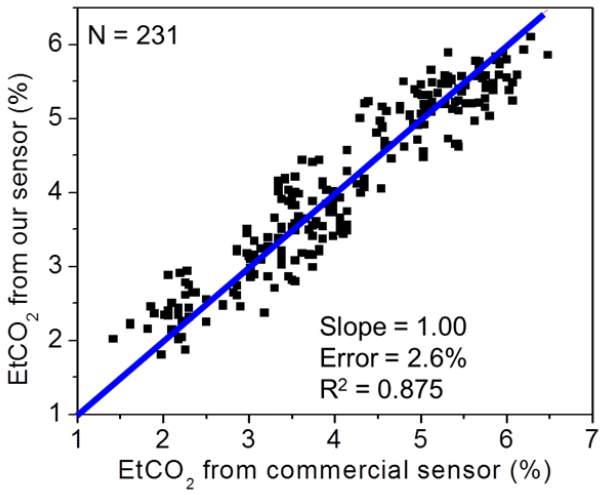

Figure 3-18. A correlation plot of end-tidal CO_2 concentration taken from our colorimetric sensor compared to a commercial infrared detector (VacuMed CO_2 Analyzer).

In order to assess the performance of the colorimetric sensor for assessing waveforms, several test subjects were utilized and their CO_2 waveforms measured by the new sensor as well as the commercially analyzer. Subjects were asked to breathe naturally into the colorimetric sensor device, then, their CO_2 patterns were analyzed for changes in slope. For example, figure 3A-B shows a CO_2 waveform for two of the tested subjects from the commercial analyzer, and the colorimetric sensor device, respectively.

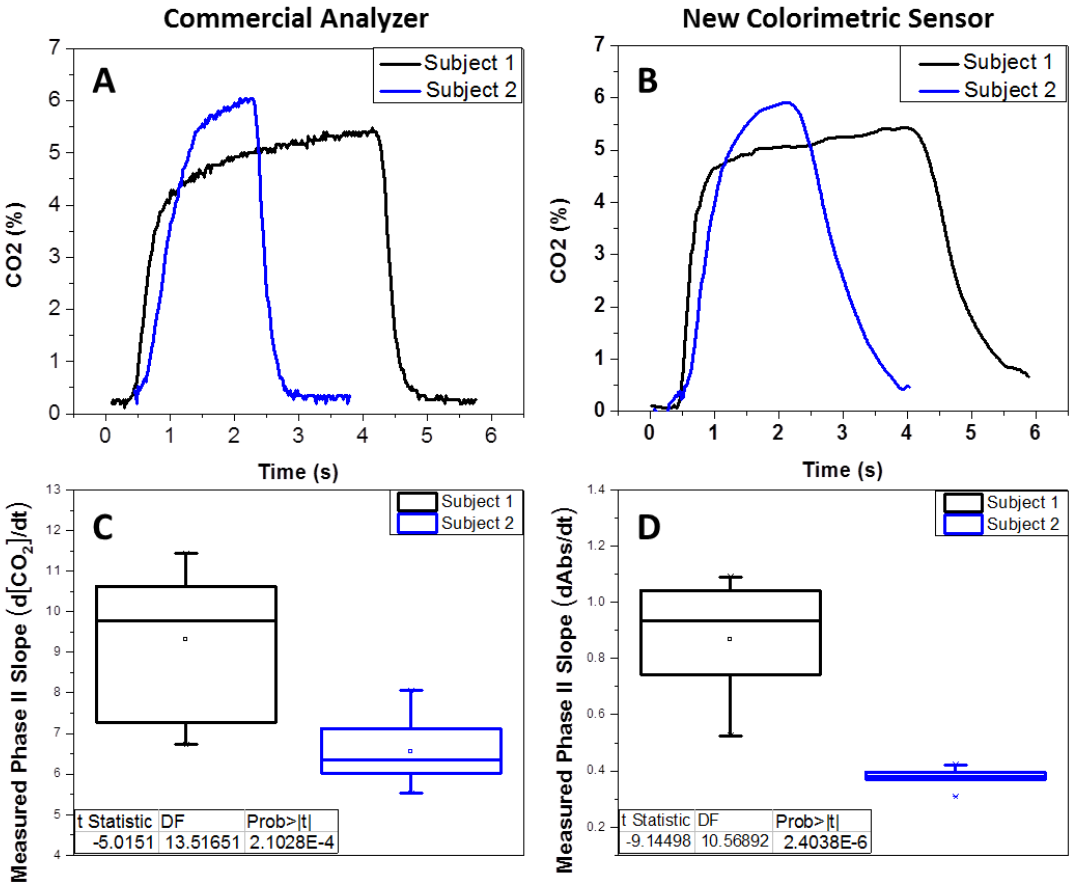

Figure 3-19. A. Two CO2 breath waveforms from different subjects, as measured by a commercially available device. B. The same two breaths as measured by our device. C. A Comparison of phase II slopes over a span of breaths, as measured by commercial device. D. Phase two slopes of the same breaths, as measured by our device.

It is worth noticing, one subject was a 23 year old female smoker with chronic breathing obstruction (subject 1) and one was a 22 year old male non-smoker with no history of respiratory problems (subject 2). The CO2 patterns from both the commercial

analyzer and colorimetric sensor show clear differences in Phase II of the exhalation waveform, indicating differences in lung function between the subjects. Figure 3C-D, show the analysis of Phase II initial expiratory slopes, known as the α angle. It was found that using the commercial sensor or our sensor, the two test subject's beginning-expiratory patterns could be easily discriminated with high certainty. In addition, as an example of the validity of the colorimetric sensor for detection of abnormal breathing patterns, a paired-t test was performed on α angles for a series of 10-11 breathing cycles for subject 1 and subject 2. The results show a statistically significant difference between α angle for subject 1 vs. subject 2, including both the commercial analyzer, and the colorimetric sensor. Furthermore, t-value for the colorimentric sensor (-9.14) had better discrimination resolution than paired t-test results for the commercial analyzer (-5.01).

In order to investigate the origin of the higher discrimination resolution from the colorimetric sensor, a comparion of time response of the CO_2 analysis methods was performed. Table 3-1 summarizes the results. The colorimetric sensor is 60% faster than the commercial analyzer. The difference is attributed to the fact the colorimetric sensor is a mainstream method, and the commercial analyzer is a sidesteam analysis method. Sidesteam methods involve the transportation of the sample from the sampling port to the detector, infrared in this case. This transport is necessary given the need of dehydration of the breath sample for infrared analysis, which is not necessary in the colorimetric sensor. The transport produces a delay of ~250 ms, and with it lateral dilution of CO_2, resulting

in a slower response time and lesser discrimination resolution for α angle analysis of breathing patterns.

By using a simple new colorimetric sensor design, we have created a simple and inexpensive method for detection of real-time CO2 patterns, and quantification of EtCO2 that is capable of assessing diagnosis of lung and gas exchange functions. Based on the results presented, we aim to develop a powerful tool in day to day monitoring of obstructive pulmonary disease that is accessible to patients for non-exacerbation based monitoring. In addition, the new colorimetric sensor is over 10 times faster than existing colorimetric CO2 sensor used for semi-quantitative analysis in intubation of patients and intensive care units. For clinical use, this type of device could be paired with current tools (namely spirometry) in order to more selectively diagnose pulmonary obstructive diseases.

4 Other Works

In additions to the work listed, two other works constitute my dissertation work. The first was the development of a colorimetric sensor for measuring oxygen and carbon dioxide in exhaled breath. The goal of the project was to create a breath sensor capable of measuring metabolism, and doing so with a low-cost and user-friendly sensor. The second work was the development of a disposable sensor for peak humidity detection. The aim of the project was to create a simple, inexpensive, and food-safe sensor that is capable of detecting peak humidity exposure.

These projects were a valuable experience which contributed to knowledge applied to this project. The humidity sensing project was a step into environmental sensing, which will be a future development of this work (environmental CO_2 detection). The Metabolic analysis project was a step into clinical validation, which will be an immediate future work on this project.

4.1 Validation of a Breath Metabolism Sensor

4.1.1 Introduction

A person's resting energy expenditure (REE) is his/her energy expenditure under resting conditions, which is the minimal need of energy to sustain life. During physical activities, the energy expenditure (EE) will be higher, depending on the type, intensity and duration of each physical activity. Indirect calorimetry is the most well established approach for accurate assessment of REE and EE, and widely used in clinical and fitness labs for nutritional support, exercise recommendation, and weight management.[68,69] However, traditional indirect calorimetry equipment is bulky, expensive, and complicated to calibrate and use. For this reason, equations have been created to estimate REE. Because REE depends on age, gender, genes and other attributes of the person, which thus varies widely from person to person, the estimated REE using the well known Harris-Benedict equation[70] or improved equations[71] can be significantly different from the person's true REE value. Additionally, a person's REE may vary over time. For example, exercise may increase REE, and reduction of calorie intake may decrease

REE.[72,73] To fulfill the needs, a mobile indirect calorimeter, Breezing® was developed to facilitate personalized REE measurement and tracking. This pocket-sized indirect calorimeter measures oxygen consumption rate (VO_2) and carbon dioxide production rate (VCO_2) in breath with a colorimetric technology, from which REE and EE are determined according to the well-known Weir equation.[74] It also measures respiratory quotient ($RQ = VCO_2/VO_2$), which is indicative of the source of energy used at the time of the measurement (e.g., carbohydrate vs. fat).

In order to evaluate the accuracy and performance of the mobile indirect calorimeter, a comparative study was carried out using mobile indirect calorimeter and the gold standard Douglas bag method. Over 300 measurements with human objects were performed following the instructions of the mobile indirect calorimeter and standard protocols of the Douglas Bag method. Statistical analysis methods, such as linear regression and Bland-Altman plot were used to establish quantitative correlation between of the values from the mobile indirect calorimeter and that from the gold standard method.

4.1.2 Materials and Methods:

Subjects

Twelve healthy adults from Arizona State University (ASU), including 7 males and 5 females, were tested during this study. Their ages ranged from 21 to 38 years and their body mass indices (BMI) ranged from 16.9 to 32.2 kg/m^2. The study was approved

by the Institutional Review Board of Arizona State University (IRB protocol #1012005855) and all subjects participated in the study voluntarily, providing written informed consent prior to participation. The study was carried out at ASU from January 2013 to June 2014.

The mobile indirect calorimeter, Breezing® Device

The Breezing® device uses a sensor cartridge and a flowmeter to determine the rate of consumed oxygen and produced carbon dioxide in the breath. The sensing technology of the new indirect calorimeter, which used a cell-phone camera as the optical detector, was previously reported.[75] The current Breezing® device uses a QR code to carry calibration parameters of a single-use sensor cartridge, which can be scanned and recognized by the mobile application (app). The device is 6.0 oz. (170 g), and 1.8 in ×2.1 in ×4.8in (4.7 cm × 5.4 cm × 12.3 cm), and connects wirelessly to an iOS mobile device, using Bluetooth 4.0 technology.

The mobile device (phone or tablet) receives data from the device, processes information, and then provides test results and summaries through a graphic user interface. It determines the energy expenditure from the measurement of VO_2 and VCO_2 according to the Weir equation, along with RQ. In addition to the sensor cartridge, the Breezing® device is used with a non-rebreathing 2-valves mouthpiece, as shown in Figure 4-1.

Methods

Before the study, the participants were familiarized with the device, the app, and the testing procedure. The energy expenditures of the subjects were tested under different conditions, including while resting, after physical activity (walking, jogging, running, or exercise in the gym), after eating, and after office work in order to cover a wide energy expenditure range (1000 -4000 kcal/day).

In order to make a real time comparison between the Breezing® device and the Douglas bag method, the gas outlet of the Breezing® device was directly connected to a Douglas bag setup to allow the same breath sample to be simultaneously measured by Breezing® device and by the Douglas bag method (see below).

Breezing® device has a pre-calibrated built-in flow sensor, which can accurately measure the breath flow rate in a range of 0 to 20 L/min with an accuracy within 3%. The single-use sensor cartridge is packed in sealed Mylar Bags with a lifetime over a year at room temperature.

The O_2 and CO_2 concentrations of the breath sample collected in the Douglas bag were measured using reference methods. A commercial electrochemical sensor (VTI Oxygen Analyzer, Vascular Technology, Nashua, NH 03062) was used for O_2 detection and a commercial infrared sensor (Telaire 7001, GE, Goleta, CA) modified with a Nafion drying tube was used for CO_2 detection. Similar to the Breezing® device, EE was

calculated according to Weir Equation and RQ was obtained from the ratio of produced carbon dioxide/consumed oxygen.

During the test, subjects breathed through a disposable mouthpiece connected to the Breezing® device for about 1-2 minutes, depending on the exhalation rate of the user, and until a total of 6 liters of exhaled air was collected. The exhalation volumes were corrected for standard dry temperature, and pressure conditions. The average oxygen and carbon dioxide concentrations from the breaths were measured. While the Breezing® device assessed exhalation rates via the use of an integrated flowmeter, the Douglas Bag method assessed the exhalation rate by measurement of total time to reach 6L exhalation volume. The oxygen consumption rate and carbon dioxide production rate assessed by Breezing® device and Douglas Bag Method were then compared.

Energy Expenditure Assessment Protocol

REE measurements were taken at resting state, including any of the following conditions: 1) immediately upon waking with overnight (8-hour) fasting; 2) after at least 4 hours from a meal (~500 kcal); 3) after at least 4 hours from moderate exercise; 4) after at least 12 hours from strenuous exercise. To measure energy expenditure other than REE, the subjects were tested right after exercises or eating, such as doing the measurement as soon as the running is finished.

Data and Statistical analysis

All data were reported as mean ± SD. The four parameters (VO_2, VCO_2, EE and RQ) were compared by linear regression and evaluated Bland-Altman plots (Figure 4-2). Statistical analysis of the data was performed using Origin Pro 8 (OriginLab Corporation).

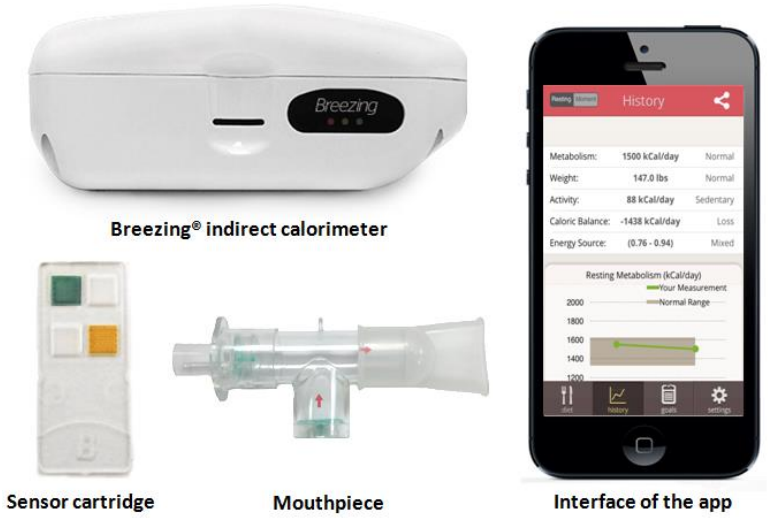

Figure 4-1. The Breezing® indirect calorimeter, sensor cartridge, mouthpiece, and iPhone interface of the application.

4.1.3 Results

Over three hundred tests were performed and the comparison between the Breezing® device and the Douglas bag method was made to evaluate the correlation

between these two methods. The results are shown in Figure 2, and summarized as follows:

VO_2 measurements: Measured oxygen consumption rates (VO_2) were in the range of 150 to 550 mL/min. Linear fitting comparing the Breezing®'s oxygen consumption rates and the corresponding Douglas bag values had a slope of 0.9954 and a R-squared correlation coefficient (R^2) of 0.9976 (Figure 2A). The mean difference of the measured VO_2 between the Breezing® device and Douglas bag method is -0.6 mL/min, indicating there is no significant difference between these two methods. For each individual VO_2 test, the difference between two methods was within ± 28 mL/min. (Figure 2B).

VCO_2 measurements: Measured carbon dioxide production rates (VCO_2) were in the range of 100 to 500 mL/min. Linear fitting comparing Breezing®'s carbon dioxide production rates and the corresponding Douglas bag values had a slope of 0.9946, and a $R^2$of 0.9986 (Figure 4-2 C). The mean difference of the measured VCO_2 between the Breezing® device and Douglas bag method is 1.4 mL/min, indicating there is no significant difference between these two methods. For individual VCO_2 test, the difference between two methods is within ±19 mL/min. (Figure 4-2 D).

EE measurements: Measured energy expenditure (EE) ranged from 1000 to 4000 kcal/day. Linear fitting comparing Breezing®'s EE values and the corresponding Douglas bag values had a slope of 0.9953 and an R^2 of 0.9981 (Figure 4-2 E). The mean difference of the measured EE between the Breezing® device and Douglas bag method is

5.7 kcal/day, indicating there is no significant difference between these two methods. For individual EE test, the difference between two methods is within ±7.6%. (Figure 4-2 F).

RQ measurements: Measured respiratory quotient (RQ) ranged from 0.65 to 1.00. Linear fitting comparing Breezing®'s RQ values and the corresponding Douglas bag values had a slope of 0.9939 and an R^2 of 0.9980 (Figure 4-2 G). The mean difference of the measured RQ between the Breezing® device and Douglas bag method is 0.004, indicating there is no significant difference between these two methods. For individual RQ test, the difference between two methods is within ±0.05 (Figure 4-2 H).

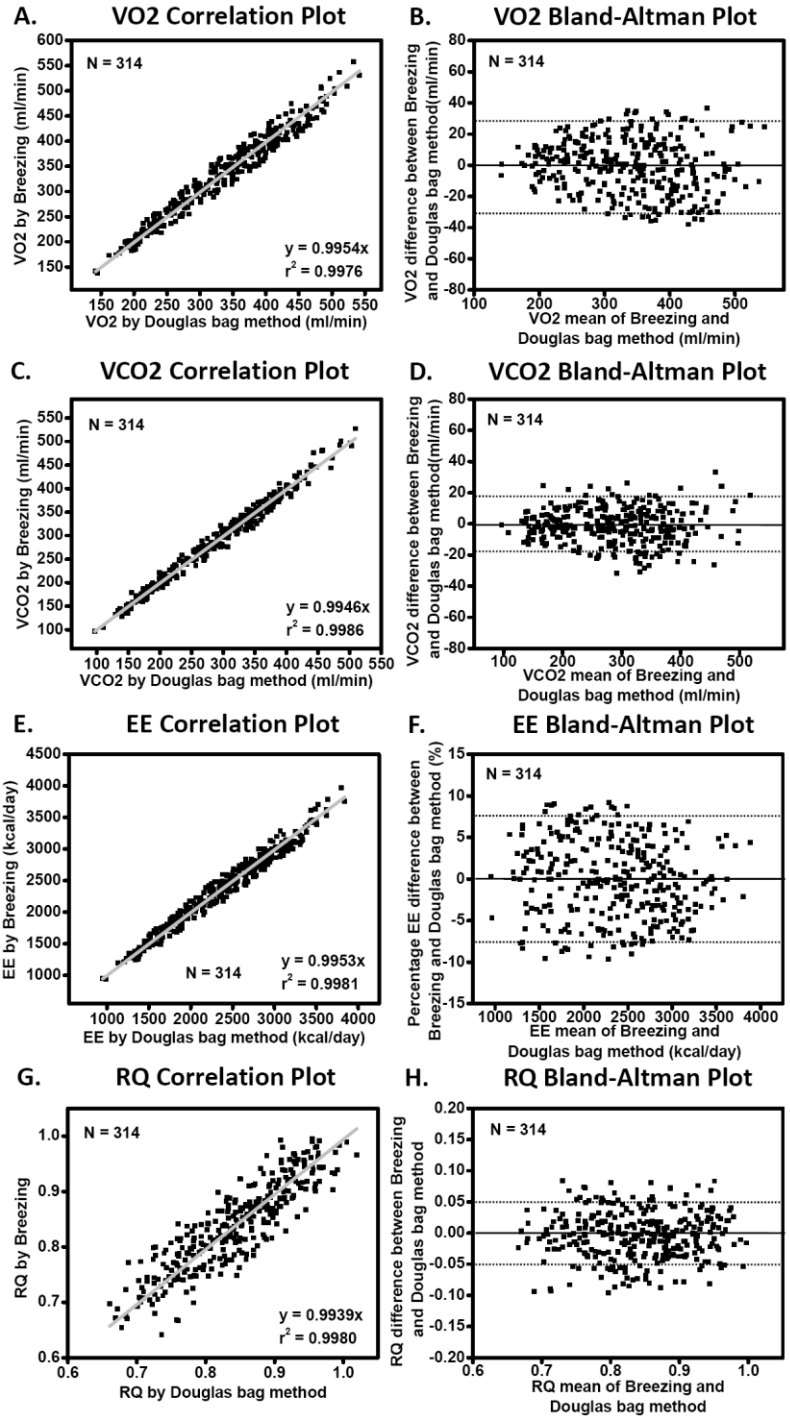
A.
VO2 Correlation Plot
N = 314
y = 0.9954x
r² = 0.9976
VO2 by Breezing (ml/min)
VO2 by Douglas bag method (ml/min)
B.
VO2 Bland-Altman Plot
N = 314
VO2 difference between Breezing and Douglas bag method(ml/min)
VO2 mean of Breezing and Douglas bag method (ml/min)
C.
VCO2 Correlation Plot
N = 314
y = 0.9946x
r² = 0.9986
VCO2 by Breezing (ml/min)
VCO2 by Douglas bag method (ml/min)
D.
VCO2 Bland-Altman Plot
N = 314
VCO2 difference between Breezing and Douglas bag method(ml/min)
VCO2 mean of Breezing and Douglas bag method (ml/min)
E.
EE Correlation Plot
N = 314
y = 0.9953x
r² = 0.9981
EE by Breezing (kcal/day)
EE by Douglas bag method (kcal/day)
F.
EE Bland-Altman Plot
N = 314
Percentage EE difference between Breezing and Douglas bag method (%)
EE mean of Breezing and Douglas bag method (kcal/day)
G.
RQ Correlation Plot
N = 314
y = 0.9939x
r² = 0.9980
RQ by Breezing
RQ by Douglas bag method
H.
RQ Bland-Altman Plot
N = 314
RQ difference between Breezing and Douglas bag method
RQ mean of Breezing and Douglas bag method

Figure 4-2. Comparison between the Breezing® device and Douglas bag method. (A) VO_2 correlation plot; (B) VO_2 Bland-Altman plot; (C) VCO_2 correlation plot; (D) VCO_2 Bland- Altman plot; (E) EE correlation plot; (F) EE Bland-Altman plot (in percentage); (G) RQ correlation plot; (H) RQ Bland-Altman plot.

4.1.4 Discussion

EE is an important parameter provided by Breezing® device. According to the test results from Figure 4-2 F, the difference was within 10% for the range of 1000 to 4000 kcal/day. Since EE is determined by the Weir equation,[74]

$$EE=[3.9\ (VO2) + 1.1\ (VCO2)] \times 1.44$$

where EE is in kcal/day and VO_2 and VCO_2 are in mL/min, the accuracy of EE measurement is determined by the VO_2 and VCO_2 measurements. The Bland-Altman plots for both VO_2 and VCO_2 showed that the absolute differences between Breezing® device and Douglas bag were less than 40 mL/min and this difference was even smaller at the lower end of the analyzed range. In contrast to previous metabolic rate measurement products that use electrochemical[76] or fluorimetric[77] sensors to determine breath oxygen concentration, assuming a carbon dioxide production rate with RQ = 0.85, Breezing® device measures both the breath oxygen and carbon dioxide concentrations to provide accurate measurement of EE, without an assumption that RQ is fixed. Since RQ is a reflection of the substrate of the energy used,[78] and today's diet compositions can be either

rich in carbohydrate or fat with RQ values closer to 1.0 or 0.7 respectively, the EE independence of RQ from Breezing device is very relevant to the field of energy expenditure assessment under free-living conditions.

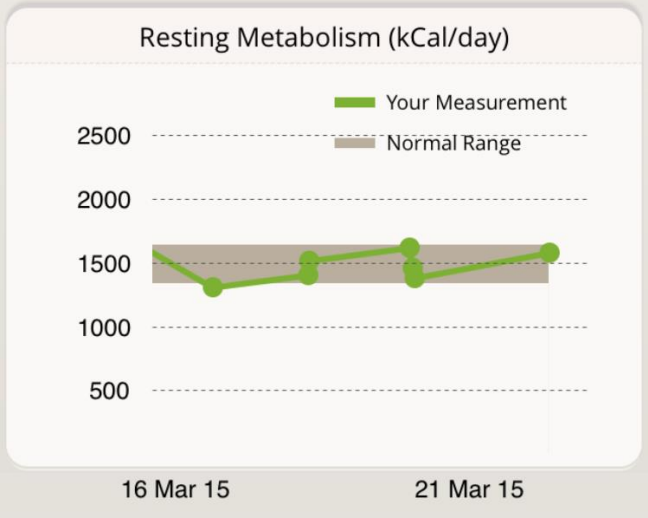

Figure 4-3. Example of REE monitoring for a study subject, using Breezing® indirect calorimeter on different days.

In addition, considering that main stream of personal and professional practices use REE estimations from equations, such as the Harris-Benedict equation,[70] which can produce a large error,[79] Breezing® device is a practice's low-cost and accurate alternative for personal and professional REE assessment.

As mentioned before, respiratory quotient is defined by[80]

$$RQ = V_{CO2} / V_{O2},$$

and indicates primary source of energy metabolized (fat vs. carbohydrates) to generate energy for maintaining body functions and activities. Therefore, instruments that measure VO_2 alone[81] cannot provide RQ information. Breezing® can measure RQ with good accuracy (slope = 0.9939, R^2 = 0.9980 and Bland-Altman difference within ± 0.05 for 80% of the RQ values).

Table 4-1: Personal information of subjects enrolled in the study.

Subject Index	Age	Gender	Weight (kg)	Height (cm)	BMI
Subject-1	28	M	82.7	167.6	29.4
Subject-2	27	F	49.9	161.3	19.2
Subject-3	23	F	65.0	162.6	24.6
Subject-4	21	M	70.0	181.6	21.2
Subject-5	24	M	90.5	167.6	32.2
Subject-6	23	M	70.0	180.3	21.5
Subject-7	38	F	64.9	161.3	24.9
Subject-8	26	F	47.6	167.6	16.9
Subject-9	25	M	65.3	175.3	21.3
Subject-10	33	M	60.9	175.3	19.8
Subject-11	30	F	52.2	160.0	20.4
Subject-12	26	M	63.5	175.3	20.7

According to previous studies, the energy expenditure level can vary for the same people under different physical activity and diet conditions.[82] The sensing technology in Breezing® device was able to provide energy expenditure information to the study participants in a user-friendly manner guided by the cell phone app. Figure 4-3 shows an example of REE tracking for a study participant, who used Breezing® device under free

living conditions several times in a day for a period of several days. As it can be seen, the new indirect calorimeter allows frequent monitoring of REE, and reveals the intrinsic REE value variability (~1,500 kcal/day average) of +/-10%, which has been reported to be typical for REE in the literature[11, 16]. It is worth noticing, the study participant using the Breezing® device did not receive any professional assistance for the measurements' assessment.

Table 4-2: Summary of participating subjects.*

	N	Age (yr)	Height (cm)	Weight (kg)	BMI (kg/m^2)
Men	7	25.7±3.9 (21-33)	174.7±5.5 (167.6-181.6)	71.9±10.9 (60.9-90.5)	23.7±4.9 (19.8-32.2)
Women	5	28.8±5.7 (23-38)	162.6±3.0 (160.0-167.6)	55.9±8.4 (47.6-65.0)	21.2±3.5 (16.9-24.9)
Total	12	27.0±4.8 (21-38)	169.7±7.7 (160.0-181.6)	65.2±12.5 (47.6-90.5)	22.7±4.4 (16.9-32.2)

* parameters including: mean ± standard deviation, and minimum and maximum values.

4.1.5 Conclusion

The test results from Breezing® device show good agreement with the results from the Douglas Bag method for VO_2, VCO_2, EE and RQ. The EE readings from Breezing® show less than 10% difference with the readings from the Douglas bag method in the range of 1000 - 4000 kcal/day. Breezing® indirect calorimeter is a portable device and easy to use, which can benefit accurate assessment of energy expenditure for multiple clinical conditions such as Resting and Non-Resting conditions under free-living conditions, and related applications, such as weight management[16] and associated-energy expenditure changes[17], excess post-exercise oxygen consumption[11].

4.2 Development of a Disposable Colorimetric Humidity Sensor

4.2.1 Introduction

Many products, ranging from food and pharmaceuticals to semiconductors and natural gas, face issues with product degradation in the presence of humidity[83-86]. In many cases, product damage due to the effect of humidity is difficult to assess before use. In pharmaceuticals, for example, humidity can cause issues with degradation of active ingredients resulting in decreased effects or changes in the auto adhesive properties of drugs, resulting in deviations from expected delivery times[85]. Most of the time, pharmaceutical products need to be stable within the 25% - 75% range of relative humidity; food products need a constant humidity range depending on the application[83-

[85]. Humidity monitoring of consumer products requires an inexpensive, simple, and equipment-free sensor with a relatively low toxicity.

In semiconductor packaging, desiccant evaluation, and similar measurements humidity monitoring is needed on a large scale, but at a low cost. Cobalt (II) chloride is commonly used for these applications, but it is unsuited for purposes where irreversibility is required and toxicity is a concern[87,88]. Other metal chlorides have been proposed and produced, but unfortunately they are still somewhat toxic and have a much higher cost than cobalt (II) chloride[89]. Moreover, metal chloride based humidity sensors can also cause environmental damage when disposed. Photonic crystal sensors have gathered a large amount of attention as a low cost optical humidity sensor due to their highly sensitive visual response to changes in humidity, but unfortunately most cannot accurately detect low levels of humidity and are intrinsically reversible sensors[90-93]. A highly sensitive, irreversible, environmentally friendly, and low-cost humidity indicator, therefore, is needed for humidity monitoring of common consumer goods.

In this section, we describe the characteristics and developmental details of a new type of colorimetric humidity sensor based on a liquid composite material. The sensing material used for sensing consists mainly of a viscous medium that provides hygroscopic characteristics for environmental humidity capture, and a redox indicator that translates the humidity level of the matrix into a distinct color change. DenimBlu30, which has been previously used for detection of oxygen in aqueous solutions, is used as the redox indicator[94,95]. DeminBlu30 is yellow in its reduced form and turns blue upon oxidation.

The choice of DenimBlu30 is strategic because it has been approved for use as a food colorant in the United States and the EU and is currently considered safe for use in many end consumer products, including blue jeans and food[96,97].

The new colorimetric sensor described here has several advantages over conventional instruments. First, the sensor is comprised of well-known compounds of low toxicity, making it much safer than cobalt (II) chloride sensors for humidity monitoring of pharmaceutical or food products[98-102]. Second, the preparation of the material for the sensor utilizes relatively mild chemicals and consists of a very simple process. Third, it was found that the probe material and matrix do not readily degrade under standard conditions when unreacted and kept dry[103-105]. Finally, the sensing material was found to easily detect peak humidity levels in the range 5-100% relative humidity, providing a sensor that can be very easily mass produced and has potential applications in pharmaceutical and food packaging.

4.2.2Experimental

Materials

DenimBlu30 (high purity, biological stain), ethanol (200 proof, analytical grade), potassium acetate (99%), magnesium chloride hexahydrate, and silica gel were purchased from Sigma-Aldrich. Sodium hydroxide (99.3%) was purchased from Fisher Scientific, and sodium borohydride (98%) was purchased from EMD Millipore. Water (18 MΩ.cm) was purified using an ELGA Purelab Ultra reverse osmosis water purifier.

Sensing Solution and Sensor Preparation

Sensing solution preparation: Solutions consisted of sodium borohydride, sodium hydroxide (pH ~10), water (10ml), Denimblu30 (saturation), and ethanol (3.75ml) mixed and purged with ultra-high purity nitrogen. After mixing, they were transferred to a nitrogen environment glove box (VAC OMNI-LAB) for storage and casting.

Sensor preparation: Sensors were prepared using GENETIX polypropylene 384-well plates as substrates. Firstly, unmodified silica gel with gypsum (60 Å porosity, 5-15µm particle size, 500-600 m^2/g surface area) was cast in individual wells of the plate and dried in ambient conditions. Plates were then transferred to a glove box and the sensing solution (13µl/well) was added to the wells. Well plates were then allowed to dry for 2 days before testing. The well plates were used only to control the drying rate of the coated silica gel; the silica gel was tested in the well plates for simplicity.

Glove Box Conditions

Samples were prepared under inert atmosphere conditions in a VAC OMNI-LAB glove box with ultra-high purity nitrogen. Humidity levels typically remained at 0.5 ppm (0.002% RH) with peak levels of 10 ppm, and oxygen levels typically remained at 0.1 ppm with peaks of less than 1 ppm. After the appropriate amount of aging time, samples were cast and allowed to dry.

Fourier Transform Infrared Spectroscopy (FTIR) Measurements

All FTIR measurements were taken using a Thermo-Scientific Nicolet 7600 FTIR spectrometer equipped with a Smart Orbit diamond plate single reflectance ATR unit. Samples for FTIR analysis were prepared by casting 50 uL samples on glass slides in glove box conditions, and then scanned via diamond ATR crystal. Background spectrums were averaged over 64 scans and sample spectrums were averaged over 32 scans. Samples were measured with a resolution of ~2 cm^{-1} in the range of 500 cm^{-1} to 4000 cm^{-1}.

Differential Scanning Calorimetry (DSC) Measurements

DSC measurements were performed using a Thermal Advantage DSC and -40 °C refrigerated cooling system with ultra-high purity nitrogen gas flow. Samples were prepared in aluminum hermetic DSC pans in masses ranging from ~3mg - ~5mg. Sample pans were loaded and pressed under inert conditions in a MBRAUN Labmaster 130 glove box. DSC samples were prepared by casting 50 uL samples of solution on glass slides, then transferring the dried sensing material to a hermetic aluminum DSC pan. An empty hermetic pan was used as a reference and a ramp rate of 10 $^{\circ}$C/min was used for all tests. The same reference pan was used for all experiments.

Humidity detection and calibration

Intensity measurements were taken using a Logitech webcam in a closed container with saturated salt solutions for humidity measurement. Ambient conditions of saturated potassium acetate (~23% RH), saturated magnesium chloride (~33% RH), saturated sodium chloride (~75% RH), and water (~100% RH) were used as calibration humidity controls. Two hours were allowed for equilibration of sensors in a close environment with a humidity control solution, and then images of the sensors were taken and processed. RGB Image processing was done in ImageJ (NIH) by taking the signal as the blue or red intensity normalized by the grey intensity (sum of the intensity of all components), which provided maximum sensitivity to humidity.

4.2.3 Results and Discussion

Fourier Transform Infrared Spectroscopy Study

As explained in the sensor preparation subsection of the experimental section, once the sensing material's components were combined, they were stored in an inert ultra-low humidity environment (glove box) at room temperature. Spontaneous reaction of the solution occurring under inert conditions determined the final sensing mixture composition, with time being the main factor. Fourier Transform Infrared Spectroscopy (FTIR) was employed to evaluate the optimized aging time of the final sensing mixture. In addition, Differential Scanning Calorimetry (DSC) was used to evaluate thermal transitions of the sensing mixture with heat exposure (see below). Preparation conditions

of the sensing mixture, used as a sensing material, were optimized, allowing for a chemically and thermally stable sensor.

It is worth noting that the sensing material was prepared by aging the solution of sodium borohydrate and the redox indicator in an alkaline media in the absence of oxygen and humidity (see reaction mechanism section), the pH of which ranged from ~7.5 to ~9. Figure 4-4 A and Figure 4-5 show FTIR spectra by which changes in chemical moieties of the sensing solution can be observed over the course of the solution aging process. Peaks due to vibrations, symmetric stretching, and asymmetric stretching of water typically occurring at 1885 cm^{-1}, 3506 cm^{-1}, and 3685 cm^{-1}, were observed for this sensing at ~1625 cm^{-1}, ~3450 cm^{-1}, and ~3550 cm^{-1}, which gives insight into changes in the sensing material's bonding environment[106]. This specific type of shift has been reported to be characteristic of very polar bonding environments in aqueous systems[107,108]. In addition, Figure 4-4A shows that the characteristic peaks of sodium borohydride diminished at 1105 cm^{-1}, 2220 cm^{-1}, and 2275 cm^{-1}, and new peaks appeared between 1800 cm^{-1} – 2300 cm^{-1}, indicating the presence of the hydrogen-bridged boron structures of diborane[109-113]. Additionally, a strong peak increasing in intensity at ~ 850 cm^{-1} indicated an increase in the concentration of orthoborates, which are expected during the aging of sodium borohydride[113]. It is worth noticing that main changes of chemical moieties occurred during the first 3 days of aging.

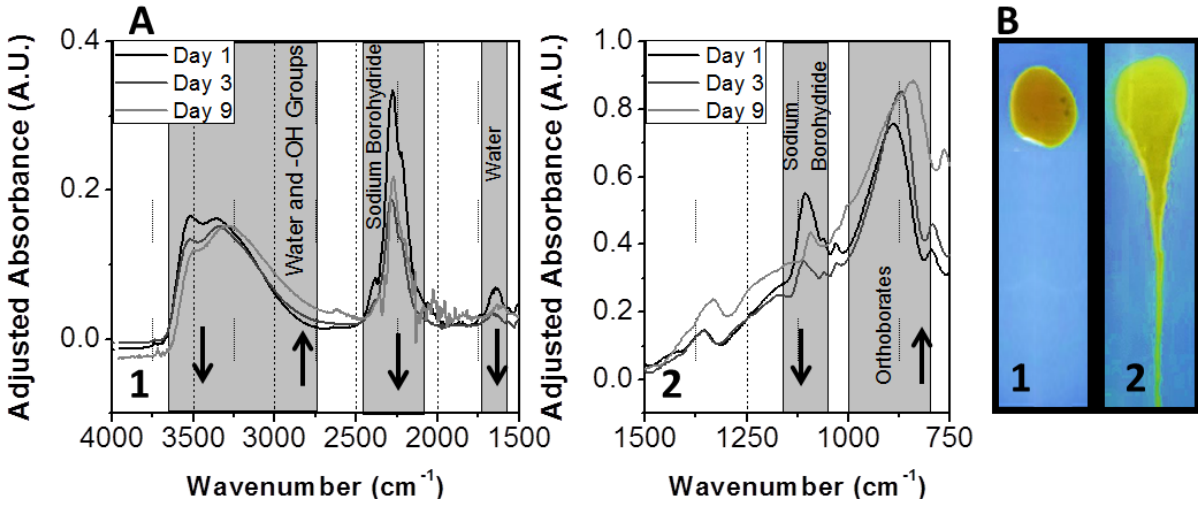

Figure 4-4. (A) FTIR spectra of sensing materials cast and dried after different days of aging in a glove box environment, short and mid IR regions. (B) Cast and dried sensing material before (1) and after (2) centrifugation. The test was performed to demonstrate the liquid nature of the sensing material at room temperature.

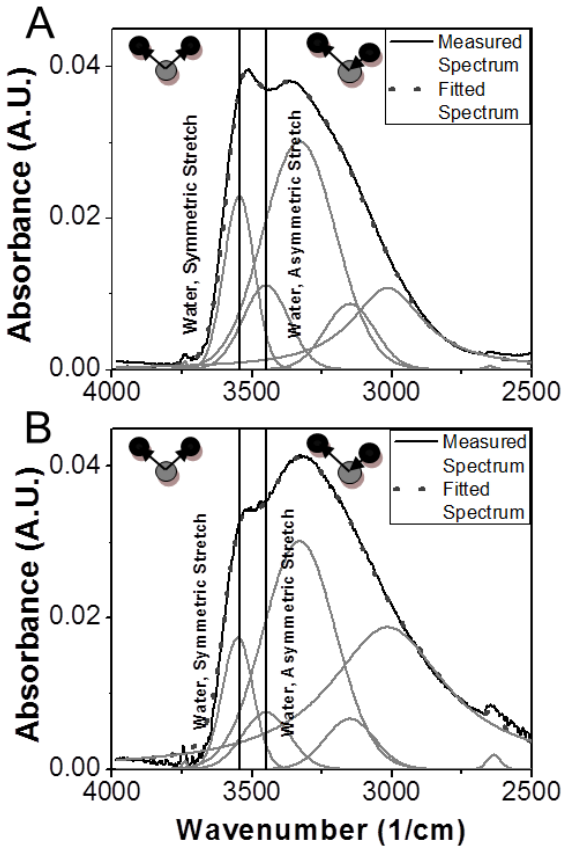

Figure 4-5 FTIR spectra from non-aged (A) and 9-day aged (B) sensing solution. Grey lines represent unmixed simulated curves. The black line represents experimental spectra.

In order to characterize the water shift phenomena, spectral unmixing simulation of the above-mentioned water and –OH peaks was performed by fitting gaussian and lorentzian distributions to the spectrum until the sum of all distributions produced a peak that matched the experimental peak with a good fit. Figure 4-5 shows the experimental and unmixed simulated spectra, and it can be seen that the peak at ~3300 cm^{-1} can be

separated into several secondary peaks corresponding to water and other -OH containing compounds. Since during the course of the reaction orthoborate concentrations rise (at ~850 cm^{-1}), -OH containing groups were attributed to said borate species and considered to be responsible for the changes in bonding environment arising from the aging process. Increases in pH of the solution from about 7.5 to 9 were measured in the course of sensing material aging (from day 1 to day 9), which is in agreement with the formation of polyborates during the course of aging[111]. Distribution of borates species (mainly $B(OH)_3$, $B_5O_6(OH)_4^-$, $B_3O_3(OH)_4^-$, $B_4O_5(OH)_4^{2-}$,$B_3O_3(OH)_5^{2-}$,and $B(OH)_4^-$) is highly dependent on temperature, pH, counter-ion, and concentration. The observed change in pH is indicative of a change in the distribution of equilibrium concentrations in the borate mixture[110-112,114].

It is important to note that the aging of the sensing solution not only brings chemical changes, but also significant changes in physical properties. The cast and thoroughly dried sensing material turns into a highly viscous liquid with aging, which can be easily dispersed by the action of centrifugation (Figure 4-4 B).

We consider the material to be a liquid composite, since it is a liquid by virtue of its diverse composition, being composed of very little solvent (see DSC analysis below) and mostly species that are highly crystalline under the same conditions when pure. Additionally, gravimetric measurements showed that the dried solution only weighed roughly 40% more than the total amount of solids added initially (after 9 days of aging). Since it is well known that much of the water is incorporated into the borate products (see

below), this reinforces the notion that very little of the final sensing element is free water.[115-117]

Solution aging was a key point for the liquid composite medium formation; it was found that a chemically stable product resulted from 9 or more days of aging.

Differential Scanning Calorimetry (DSC)

DSC was performed to evaluate the thermal properties and thermal stability of the non-aged and aged sensing material. Figure 4-6 A shows DSC scans for sensing material samples aged for 1, 4, 9, and 14 days. In addition, the heat absorbed (lower portion of the scan) and released (top portion of the scan) during the scan was evaluated during heating and cooling (Figure 4-6 B). Likewise, heating and cooling glass transition temperatures were extracted. In all samples, heating glass transitions were observed from -12 °C to 35 °C and a small degree of quenching and annealing was seen during cooling at -15 °C [118]. From Figure 4-6 B, it can be observed that the sensing material's heat capacity decreased and approached constant values as aging time increased. This is consistent with a drop in water content, as water has roughly double the heat capacity of anticipated borate products [119].

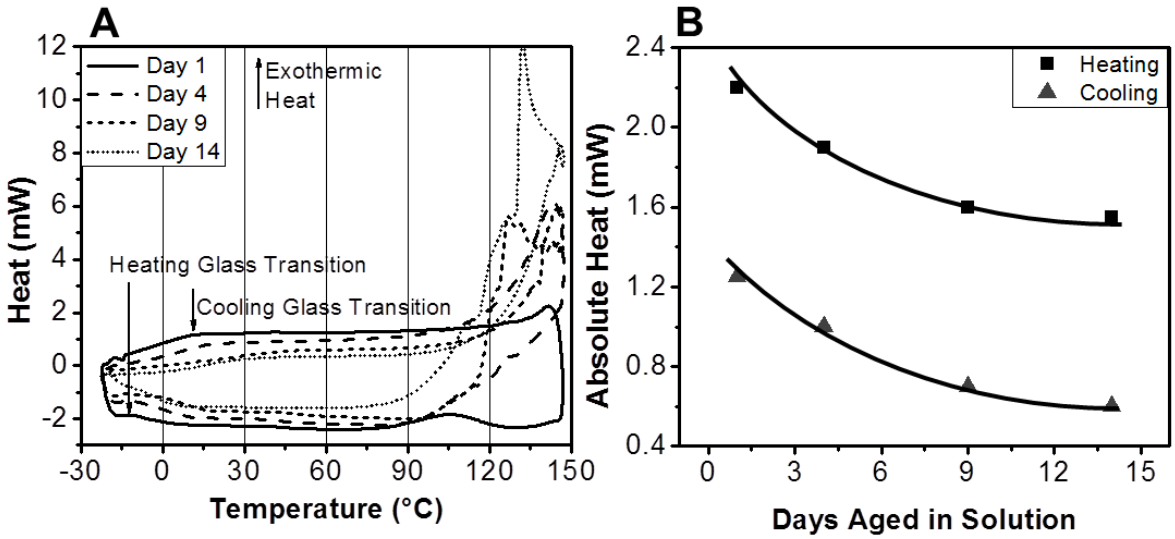

Figure 4-6. (A) DSC curves for samples aged different times in aqueous media. (B) Heat capacity of sensing material vs. aging time of the solution used as sensing material. Note: absolute values are not corrected, and they may include instrument offset. However, testing offset is equal for each test.

It is worth noting in Figure 4-6 A that higher values of heat, indicating an exothermic process, were released once the samples were exposed to temperatures higher than 90 °C. In addition, the degree of the exothermic process was elevated for longer aged sensing samples. This exothermic reaction may occur due to the presence of borate products in aged samples. It is hypothesized that some borate products (e.g., diborane) could react with the aluminum capsule used for testing. This exothermic reaction, in

addition to glass transition temperatures (see below), were utilized to access the stability of the synthesized sensing material over time.

In order to stabilize the aged sensing material, a heat treatment at 50°C was applied. Aged sensing samples treated at 50 °C did not show destructive exothermic behavior after (at least) 1 week of treatment. Figure 4-7 A shows an example of DSC scans for 9-day aged sensing samples untreated, and then treated with heat for 1, 2, and 6 weeks. In all heated samples, destructive exothermic behavior was not observed below 100 °C during high temperature DSC tests. In addition, the stability gained for heat treatment was found to be permanent. This effect is demonstrated in Figure 4-7 B.

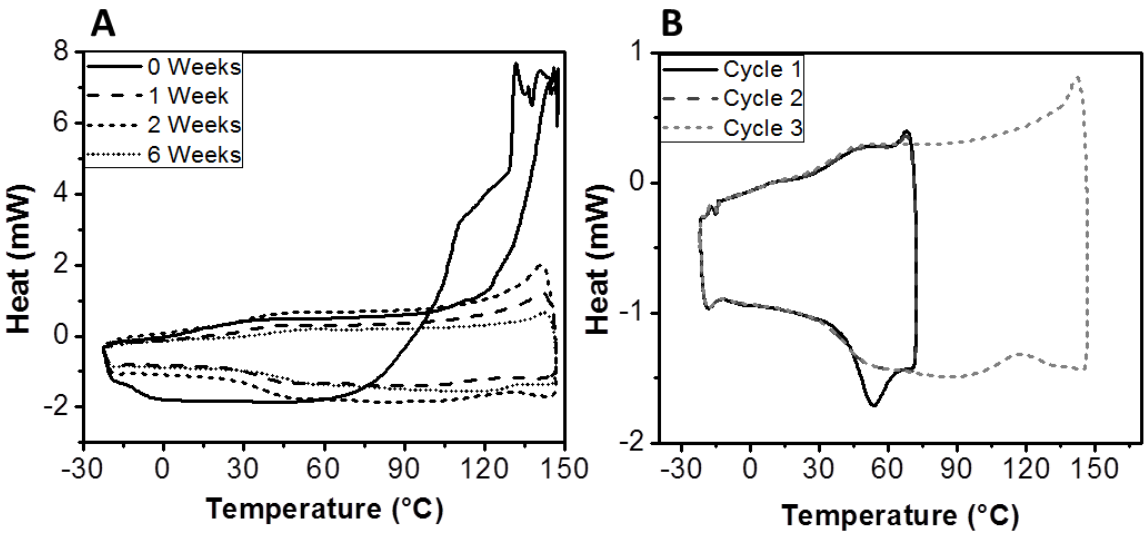

Figure 4-7. (A) DSC curves of sensing materials cycled from -20 to 150 °C after 2 cycles from -20-75 °C. The sensing materials were left at 50 °C for different times. (B) DSC curve of sensing material at low (up to 70°C for 1st and 2nd cycles), and at high (150°C

for 3rd cycle) temperatures. The sensing material sample was previously treated with heat at 50 °C for 5 weeks and left at 25 °C for 1 week.

During the course of this work, DSC thermal cycling was performed and the analysis of changes between cycles was noted to be indicative of thermal stability. As evidenced by cooling glass transition temperatures shown in Figure 4-8 A, the temperature of the first cooling glass transition shifted notably in non-aged solution samples during thermal cycling. The shift became more evident with sensing samples that were further aged. However, the shift disappeared for heat-treated aged sensing samples. The stability shown in the glass transition temperature after heating (Figure 4-8 A) was also observed in heat-treated sample kept at room temperature (not shown). This is in agreement with the stability gained in the inhibition of the exothermic process (discussed above). Therefore, it can be concluded that oven aging of the sensing samples results in thermal stability gains that are retained over time at room temperature conditions.

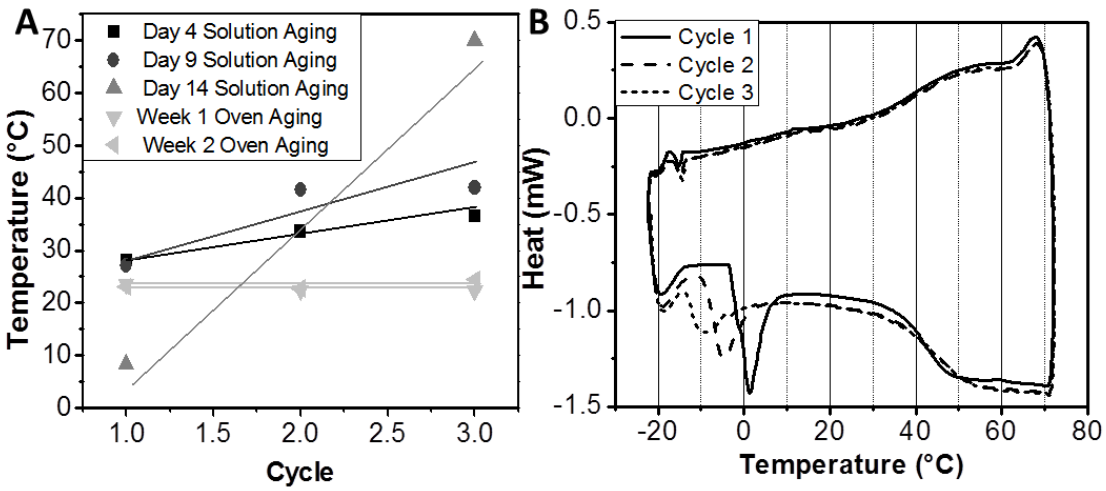

Figure 4-8. (A) Cooling glass transition temperature vs. cycle number, with first 2 cycles ramping from -20 to 75 °C, then the third cycle ramping from -20 to 150 °C for different aged sensing material samples (4, 9, and 14 days), and 14-day aged sensing samples treated with heat at 50°C (1 and 2 week oven aging). (B) DSC curve from thermal cycling of a slightly hydrated sample (see text for details).

An investigation of hydrated samples provides further evidence of the low-solvent nature of the liquid composite. It is well known that weakly associating water in the sensing material can be detected by a melting point at slightly below 0°C[118]. In Figure 4-8 B, a sample that had not dried to the same degree as the rest of the samples was cycled. It can be seen that the first cycle exhibits a melting point slightly below zero. In subsequent cycles, the melting point lowers in temperature, the melting peak broadens,

and the melting peak lowers in intensity. This is indicative of water in the borate matrix that is weakly associating with the chemical environment; this free water begins to associate more strongly with the matrix on each thermal cycle. The lack of this feature in the remaining DSC curves indicates that little to no free water is present in the sensor. Thermal cycling demonstrated that increases in instability from solution aging could be alleviated by oven aging of the prepared sensor. This reinforces the notion that our sensing material is a liquid composite material with little to no characteristics of free water.

Humidity Detection

As described in the experimental section, the sensing material was deposited onto silica substrate. Optical measurements were taken with sensor exposure to different humidity levels. Figure 6A shows the absorbance spectra of the sensing material before and after the exposure to humidity. It can be observed that the wavelengths corresponding to Blue and Red RGB components were the most affected by the humidity-induced color change. The Blue and Red intensity changes were normalized by the sum of the intensity of all components (RGB), giving a measure of chromaticity change, and studied as a function of relative humidity levels. Figure 4-9 B summarizes the most relevant results of the system. It is worth noticing that the normalized Red signal gave out greater sensitivity at low relative humidity levels, while the normalized blue signal showed greater sensitivity at high relative humidity levels.

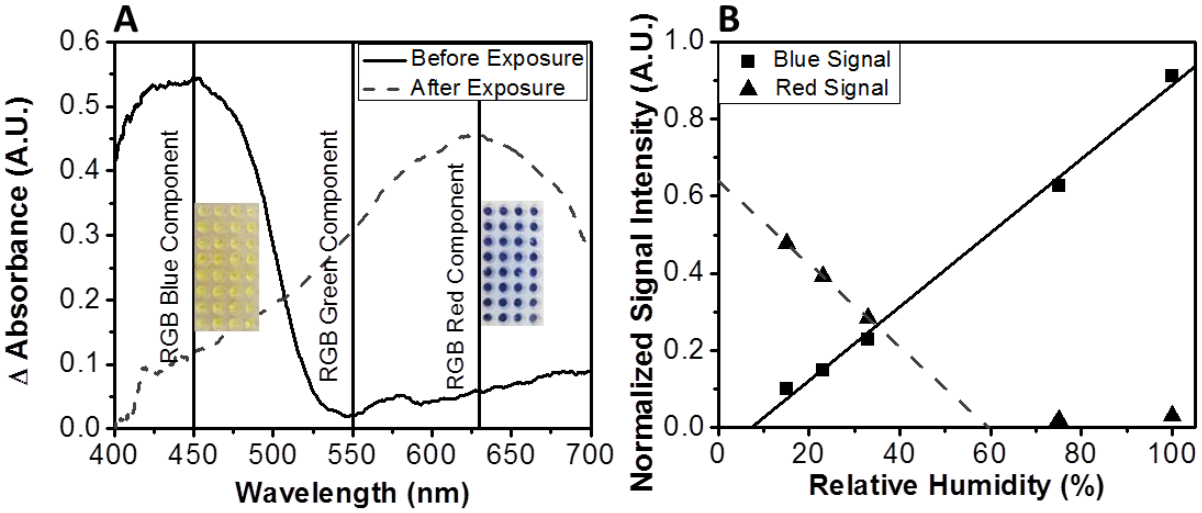

Figure 4-9. (A) Absorbance spectra of sensing material. The changes are due to reduced and oxidized dye. RGB wavelengths are marked with solid vertical lines, along with pictures of the new humidity sensor. (B) Calibration curve of the new humidity sensor. Relationship between the new humidity sensor signal and relative humidity assessed with a reference humidity sensing device. The sensor signals were taken as the intensity (red or blue) change over the total intensity (red + blue + green) of the sensor.

Another interesting feature observed was that when placed in a dry environment after two or more hours of equilibration to a set humidity, the sensors did not display reversible behavior. This is likely due to the high stability of the reduced form of the redox dye in this medium. Figure 4-10 shows comparative results assessed between the new calibrated colorimetric humidity sensors and either ambient relative humidity levels measured via hygrometer or humidity controlled by saturated salt solution. It can be

observed that calibration of the sensor using a CMOS chip from a webcam setup illuminated by ambient lighting can provide relatively accurate results that are in good agreement with the reference sensor, with errors not exceeding 12%. Overall, we found the sensor capable of detecting humidity levels with a standard deviation of roughly 3.3% relative humidity, which could be improved upon by better preparation methods, testing conditions, and signal processing. The sensing reaction takes between 50-70 minutes to equilibrate under natural diffusion. It is worth noting that the sensor response may be accelerated by using different sensor configuration and forced convective. Despite improvements being needed, our sensor still provides improved resolution than the typical cobalt (II) chloride sensor without utilizing toxic materials.

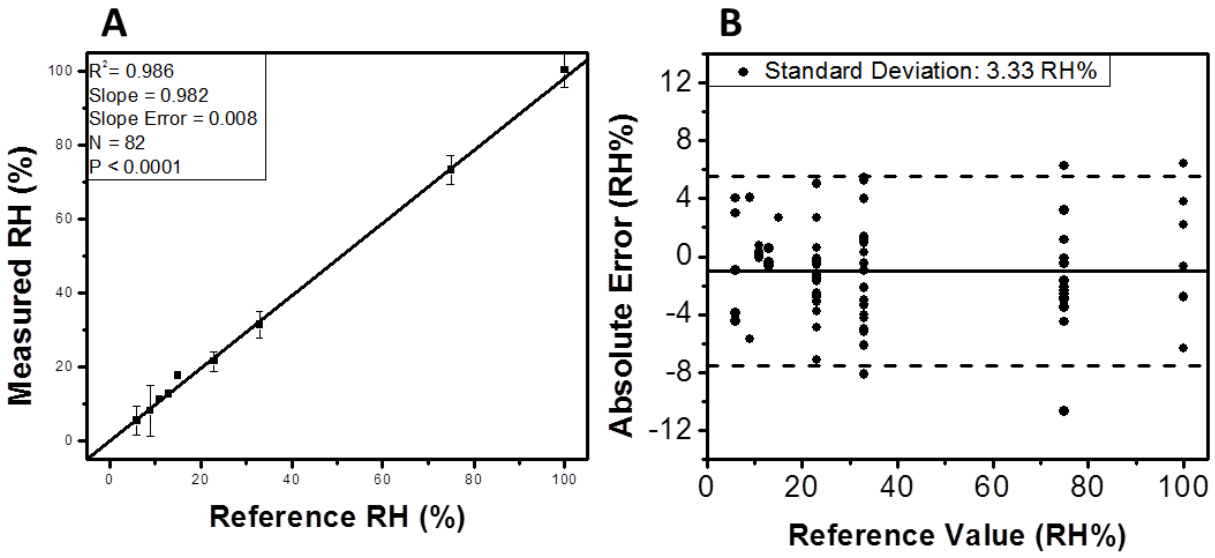

Figure 4-10. (A) The relationship of relative humidity readings (RH %) between the new humidity sensor and a reference humidity sensing device. (B) Bland-Altman plot

comparing the new sensor's absolute errors to the reference humidity sensing device in a range from 0 to 100% with dotted lines representing the 95% confidence limits.

Reaction Mechanism

The borate matrix is produced in aqueous conditions by the reaction of sodium borohydride with water, producing mainly $NaBO_2$ by the irreversible reaction: [110-112,114,115,117]

$$NaBH_4(aq) + 2H_2O(l) \rightarrow NaBO_2(aq) + 4H_2(g)$$

The reaction product, $NaBO_2$, is hydrated to generate $NaB(OH)_4$, which then equilibrates reversibly into a diverse mixture of borate ions. In simple aqueous systems, borate ion solutions can contain over a dozen components, since the composition depends on temperature, pH, concentration of species, and counter-ions[110-112,114]. The aqueous borate solution is then coated on silica gel and dehydrated. This sensing material product maintains itself as a liquid composite coating providing a very strong hydrogen bonding environment, as discussed above.

While in the dehydrated state, the strong hydrogen bonding environment does not allow oxidation of the redox dye, despite ambient conditions holding ample oxygen (generally 20.5%). This is possibly due to unfavorable reaction environment and/or extremely low permeability of the liquid composite coating to oxygen. Humidity detection is attained by embedding this redox dye in the borate matrix and taking advantage of its strong hydrogen bonding borate environment, which is favorable for water absorption. Once the dye-modified liquid-composite material is exposed to water,

absorption of water induces an improvement of dye-oxygen reaction environment and/or increase in the liquid composite's affinity for oxygen, resulting in a visual oxidation of the redox dye from yellow to blue[120], which is made irreversible by the liquid-composite being deposited on silica; the liquid composite itself has shown reversibility when exposed to a dry environment after reaction. It is also worth remarking that the sensor is designed and tested for ambient oxygen levels (20.5%).

In addition, it was found that by varying the film thickness of the sensing liquid composite on the silica gel the sensitivity and dynamic range of the sensor can be easily tuned. Thick coating sensing films were more sensitive to higher humidity levels, while thinner coating sensing films were more sensitive to lower humidity levels. This is an interesting feature for implementation of the sensor in real sensing conditions and broad humidity level range.

Stability

The sensing material developed herein has shown great long-term stability in room temperature settings. Sensors that have been exposed to dry environments with high and low oxygen concentration have shown no signs of visual color changes or degradation of the material for over 4, and 12 months, respectively.

4.2.4 Conclusion

The borate-redox dye based humidity sensor was successfully prepared, and systematic characterizations were performed using FTIR, DSC, and imaging methods to

gain insight into the composition, sensor stability, and reactivity. The extent of reaction of sodium borohyride in the sensing solution was monitored via FTIR, and showed that after 9 days of solution aging a chemically stable liquid composite sensing material could be produced. By DSC screening, we found that further aging in the dried state at elevated temperature produced a thermally stable sensing material. By aging the dried sensor at 50 °C, thermal stability could be established as per evaluation by traditional and cyclic DSC methods. The material was found to be stable over time in conditions similar to or more extreme than the needs of the food and pharmaceutical industries with the use of materials of low toxicity. The sensor can detect a relative humidity in the range of 5-100% in an irreversible manner with good reproducibility and high accuracy. This low-cost, highly sensitive, and easy-to-use humidity sensor can be sized to a miniaturized strip, which makes it easy to be applied to product humidity monitoring in pharmaceutical or food products.

4.3 Thermochemical Humidity Detection in Harsh or Non-Steady Environments

4.3.1 Introduction

Although humidity sensing is a well-established field with a range of sensors for low-cost, high accuracy, or other special applications, humidity sensing in harsh or complex environments is still a challenge. Some examples of harsh environments are sewers and equipment for drying prepared foods. In both of these cases, monitoring humidity may be needed for improved outcomes. For instance, relative humidity is an

important factor in predicting corrosion rates in sewers. In the United States alone, it was estimated that sewer corrosion incurs a cost of 14 billion dollars annually.[121] Work has gone into building predictive models for service life in order to avoid costly sewer collapse[122-124]; however, as seen in the work of generating predictive models, humidity is an important factor and is beneficial for predicting corrosion rates. On the other hand, it has been found that in the aggressive environment of sewers, traditional electronic humidity sensors can begin to fail in as little as a few days due to the same effects driving sewer corrosion [125]. Along this line, work has been reported for development of robust sensors capable or monitoring this environment, which includes Optical Fiber-Based Gratings[125] and Strain-Based Fiber Optics[126]. In addition, humidity detection in food processing can present a major challenge since the environment can be nearly fully dry (~0% relative humidity), and physically challenging due to the exposure to particulates, and suspended materials[127-129].

Another challenging environment for sensing humidity is breath. Breath humidity is important for detection of hydration, and for accurately detecting other parameters related to metabolism[1], lung function[130], and renal status.[131] Scaling breath sensing technologies to clinical and consumer levels, however, is a massive challenge due to complexities in handling breath.[132-135] Breathing involves inconsistent and complex flow patterns and sampling involves massive changes in both humidity and temperature, especially in rebreathing applications.

In previous works we have developed disposable humidity sensors based on color change detection for product monitoring[38]. In this work, we demonstrate the utility of a thermal method for humidity detection, utilizing two approaches, consisting of a surface hydrophilically tuned to produce an exo- or endothermic reaction in response to humidity:

1- A thermistor-based chemical sensor, which consists of a surface-treated thermistor, enabling an inexpensive and robust contact method with an accurate low-thermal mass thermistor starting at less than $3 in bulk and simple data-acquisition circuitry, which can be insulated from harsh environments.
2- A thermographic humidity sensor, which utilizes a thermal camera to image a simple disposable sensing element, enabling a non-contact method of transducing humidity signal. Thermal infrared sensors start at as little as $8 each in bulk and consumer thermal cameras start at as little as $250 (FLIR One)[136].

In both methods, high accuracy can be achieved when applied with a proper reference, such as an uncoated thermistor (in the method 1- thermistor-based chemical sensor) or insulated spot on the disposable imaging element (in the method 2- thermographic humidity sensor). In both approaches, the chemical modification of the thermistor or the disposable imaging agent (sensing element) have a wide variety of sensing options available. In this work, we take advantage of heat interactions involved in the hydration of a neutral salt in the presence of humidity. With this, we demonstrate the effectiveness

of thermistor-based chemical detection of humidity and the characterization and effectiveness of thermographic chemical detection of humidity.

4.3.2 Materials and Methods

Thermistor-Based Method

Thermistor-based method consists of a coated thermistor in a gas stream exposed to alternating samples of dry and humid gas samples (see Figure 4-11). For these experiments, the temperatures and flows of the two gasses were held constant, such that any heat effects were purely from water interactions.

Sensing Thermistor preparation: The sensing thermistor was prepared by coating a low-thermal mass thermistor (EPCOS, part no. B57550G0103F000) with a solution containing a long-chain quaternary amine salt and color dye. The salt provides heat upon hydration, the buffer works to stabilize the sensor, and the dye allows for visualization. The thermistor was dip-coated and allowed to dry in ambient lab conditions. Measurements were taken at 40 Hz, with an effective temperature resolution of less than 0.05 Celsius.

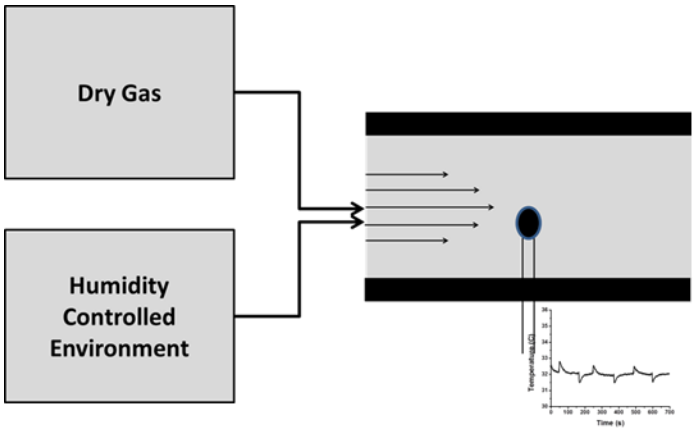

Figure 4-11. Schematic of the thermistor-based humidity detector. Alternated dry gas and humidity controlled samples were introduced at constant temperature and flow rate into the sensor chamber.

Humidified Gas Samples: Humidified samples were made using a humidity controlled environment (Coy Labs). A large chamber was maintained at a humidity set point, and then gas from said environment pumped at a set flow rate over the thermistor.

Thermographic Method

The thermal camera setup utilized a sensor with the same chemistry as in the thermistor-based chemical method. In this case, the hydrophilic sensing mixture was applied in the form of a disposable coated Teflon strip. The Teflon strip was placed in a heated aluminum block (see Figure 4-12). For the thermographic tests, heat accounting was performed for general heat transfer, including conduction and convection.

Disposable sensing element: The sensing elements were prepared by coating a porous Teflon membrane with the same mixture as the thermistor. The Teflon is dip-coated and dried, then laminated into an easy-to-handle chip, as seen in Figure 4-12A.

Flow Measurements and Heating: Flow measurements and heating were performed in a custom setup. Flow measurements were performed with a differential pressure flow meter (Confined Pitot Tube[137] with a Freescale MP3V5004DP differential pressure transducer). Heat was supplied to an aluminum heating block via a Nichrome wire, with a temperature set point of 37.9 degrees Celsius. This temperature was named sensor block temperature, T_{block}. The device was designed such that the sensing element (sensor) sits in the aluminum block and the flow laterally runs over the sensor. The imaging port is located in the opposite side of the sensing element, as seen in Figure 4-12B. An additional thermistor (same as above) was located in the flow stream to take the gas stream temperature, T_{gas}. This temperature, together with T_{block} and the temperature measurements assessed via the thermal camera (see below) on the sensing element (T_{sensor}) were also taken in the gas stream in order to build the heat model used for evaluation.

Thermal Camera: A FLIR A655sc was used for the experiments. The camera utilizes an uncooled micro bolometer sensor array with a 640x480 resolution, 50 Hz full-window resolution, and accuracy of +/- 2% of the reading. All data acquisition was done in the provided software: Research IR.

Humidified Gas Samples: Samples were prepared by passing dry gas through a water bath. Samples with 100% relative humidity were prepared by passing the gas through pure water and 33% relative humidity samples were prepared by passing the gas through a saturated magnesium chloride solution.

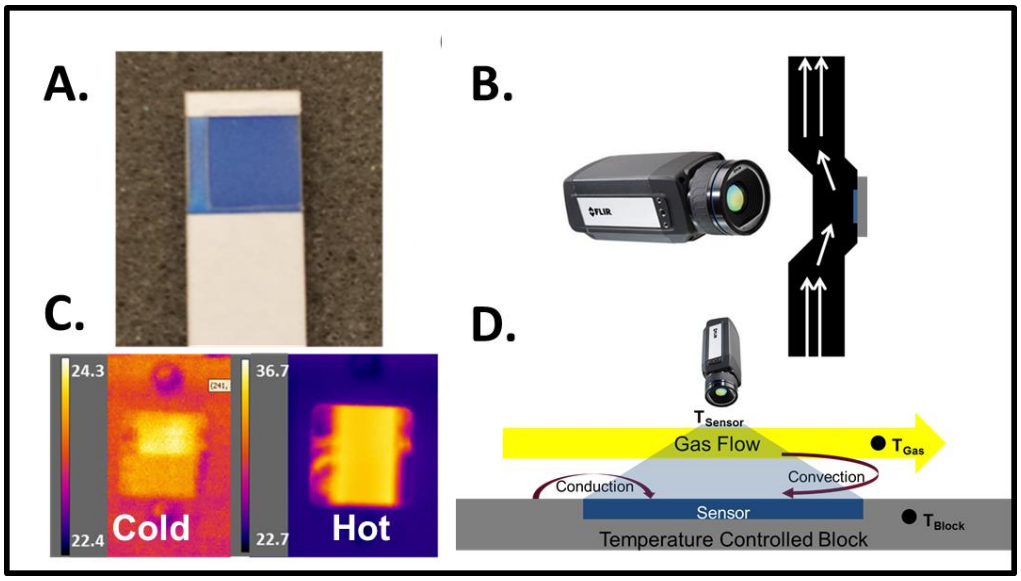

Figure 4-12. Thermographic Method: (A) The sensing element used for relative humidity testing. The sensor consists of coated Teflon membrane (blue) laminated in polystyrene with cardstock for easy handling and rigidity. (B) An illustration of the test setup, where the camera is viewing inside of a slot in the top of the flow device, with air being passed over the sensor, and the sensor sitting in an aluminum block held at constant temperature. (C) A comparison between hot and cold thermal images of the setup. The warmer portion of the image is the sensor inside of the flow chamber used for the experiments, and the colder portions are the exterior of the device. (D) A schematic of the heat transfer

phenomenon present when testing the strip. Note that relevant temperatures are measured by thermistor at the probe in the gas stream (T_{gas}) and the sensor block (T_{block}), along with measuring the sensor via thermal camera (T_{sensor}).

4.3.3 Results and Discussion

Humidity measurements were performed using both methods: thermistor-based detection and thermographic detection, both of which were utilizing the same hydrophilic chemical probe, consisting of a mixture of a salt with a dye. With this type of chemical probe, the latent heat of vaporization of water and the enthalpy of hydration for the salt can be taken advantage of for thermal detection.

Thermistor-Based Humidity Detection

Figure 4-13A shows the result of the thermistor-based humidity sensing experiments. The experiments were carried out at room temperature with insignificant fluctuations of temperature between tests as indicated by a hydrophobically (PTFE)-coated thermistor sensor used as reference. Therefore, all temperature changes in the hydrophilically-modified thermistor were related to the humidity changes. As it can be seen in all experiments shown in Figure 4-13A, there is a significant increase in temperature with humidity exposure. The temperature and flow of the stream were held constant, so heat gained is gradually lost to the stream. Due to this, we see a spike and decrease in temperature rather than accumulation. Since the temperature and flow rates were held constant, for analysis purposes, only the difference between the baseline and

peak temperature from humidity exposure was needed. Figure 4-13B shows the relationship between the relative humidity that the sensor is exposed to and the corresponding observed temperature change. It can be seen that the thermistor-based sensor provides a proportional correlation between the temperature change and the relative humidity, and saturates around 75% relative humidity. The sensor saturation effect could be potentially combatted by either changing the chemical coating or heating the thermistor.

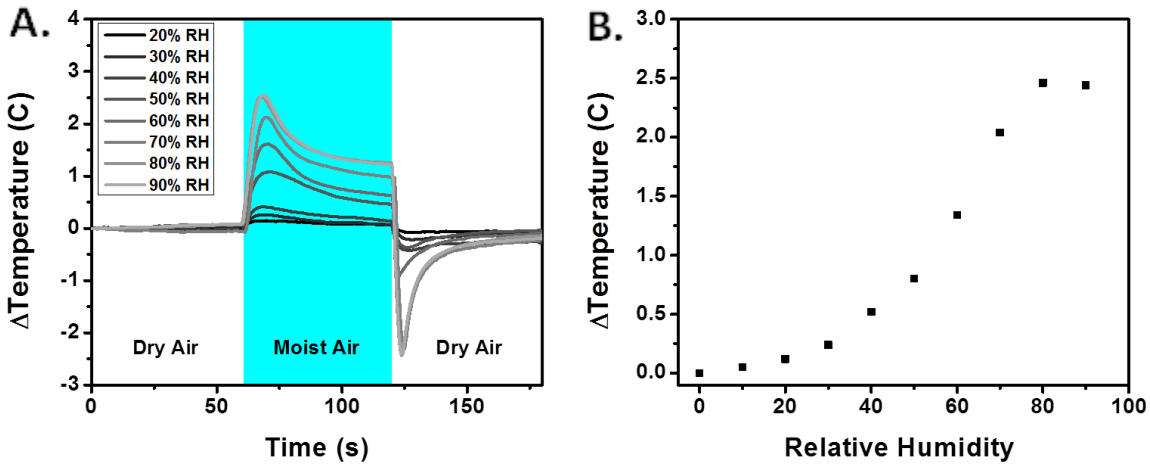

Figure 4-13. (A) Test results from alternating between dry and humid air. Absolute temperatures during the tests ranged from about 23 to 26 degrees Celsius. (B) The difference between the baseline and the peak temperature increases as a function of relative humidity.

Thermal Camera Humidity Detection

The second method was to utilize a thermal camera to measure temperature changes on a disposable sensor. In order to measure heat interactions due to humidity, the sensor was held at an elevated temperature and sample gases were introduced at known flow rates. The elevated temperature works to prevent the sensor from saturation (as seen with the thermistor), which also works to protect the sensor from water accumulation. Heating was done with an aluminum block holding the sensor (see Figure 4-12D). Although higher temperatures are desirable for avoiding saturation, the temperature also needs to be low enough to allow for hydration. For this set of experiments, the temperature of the aluminum block holding the sensor was set at 37.9 degrees Celsius. For this set of tests, the flows and temperatures were not held constant like in the thermistor-based method. Due to this, changes in inlet temperature and flow rate needed to be accounted for.

The sensing system utilizes heat generation from the hydration of the hydrophilic chemical layer on the sensing element for the quantification of humidity levels. In order to relate the amount of heat generated from humidity interactions, the system needed to be characterized in terms of heat contributions from conduction and convection. Therefore, heat contributions from the three heat sources: conduction, convection, and chemistry were accounted for. Equation 4 shows the overall heat relationship:

$$\frac{dQ_{total}}{dt} = \frac{dQ_{conduction}}{dt} + \frac{dQ_{convection}}{dt} + \frac{dQ_{chemical}}{dt} \quad (4)$$

where Q is heat flux, either total or from a contributor (conduction, convection, or chemical interaction) as a differential over time (t). Equation 5 shows the relationship between the total heat and the mass (m), specific heat capacity (c), and the temperature of the sensor (T_{sensor}):

$$Q_{total} = \mathrm{m} * \mathrm{c} * \Delta T_{Sensor} = m * c * T_{Sensor} \quad (5)$$

By utilizing a reference state of 0 degrees Celsius, we can simplify equation 5 to what is seen on the right side of the equation. The relationship can be further broken down to equation 6 as follows:

$$\frac{m * c}{A} * \frac{dT_{Sensor}}{dt} = K * \left(T_{Surface} - T_{Sensor}\right) + H(f) * (T_{Gas} - T_{sensor}) + B * \frac{dC}{dt} \quad (6)$$

where A is the area, K is the conduction coefficient, $T_{surface}$ is the temperature for the block (T_{block}), T_{sensor} is the temperature of the sensor, H(f) is the convection coefficient as a function of the flow rate (f), B is the amount of heat generated per unit change in relative humidity concentration, C is the concentration of humidity on the sensor, and t is time. This form gives explicit contributions from each component in terms of coefficients, which were determined under certain experimental conditions as described in the next sections.

Heat Transfer Characterization of the Thermographic Sensing System

Conductive Heat Transfer Characterization

The first characterization of the system was to perform heat tests without a flow in order to determine the conduction and free convection rates. In order to measure changes under these conditions, a sensor at room temperature was placed inside of the heated device, and then the rate of heating recorded via thermal camera. These tests were performed at constant relative humidity with no flow. Under these conditions equation 3 can be simplified to equation 7.

$$\frac{m * c}{A} * \frac{dT_{Sensor}}{dt} = K * \left(T_{Surface} - T_{Sensor}\right) + H(0) * (T_{Gas} - T_{sensor}) \quad 7$$

At steady-state conditions, the net heat flux will be equal to zero, which allows for simplification down to equation 8.

$$\frac{K}{H(0)} = \frac{(T_{sensor} - T_{Gas})}{\left(T_{Surface} - T_{Sensor}\right)} \quad 8$$

In order to determine the absolute values of the coefficients, the relationship can be solved for non-steady-state conditions, as seen in Figure 4-14. By performing this analysis, we can ascertain both K and H(0) for our system.

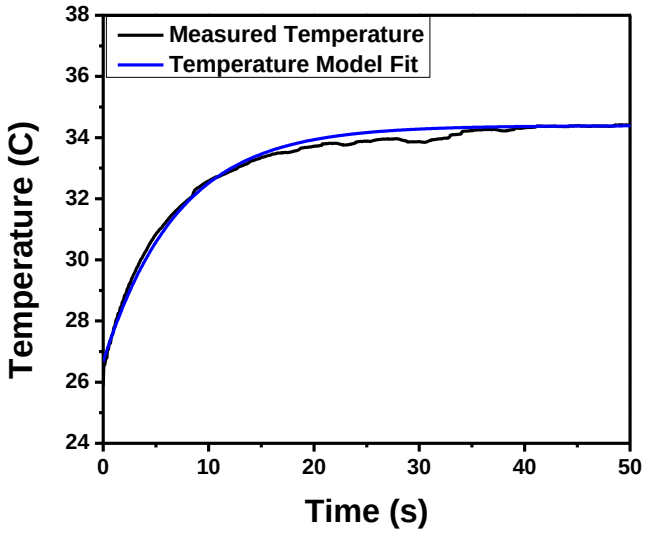

Figure 4-14. A non-flow test showing the change in temperature of the sensor over time after the room-temperature sensor is inserted into the heated device.

Convective Heat Transfer Characterization

The next step was to determine the relationship of the convection coefficient as a function of flow rate. This was done by setting a dry gas cylinder to a set flow rate and cycling flow through the setup (on and off), all while recording the temperature changes with the thermal camera. This allows a very straight forward and simple method for assessing the convection coefficient at constant flows, as all temperatures and the conduction coefficient are accounted for in all cases. Figure 4-15A shows a series of these tests. From these tests, the convection coefficient (H) as a function of the flow rate

can be obtained, as shown in Figure 4-15B. Note that the behavior at low flows is not characteristic of a typical flat-plate cooling relationship[138]. This is due to the unique geometry of the system.

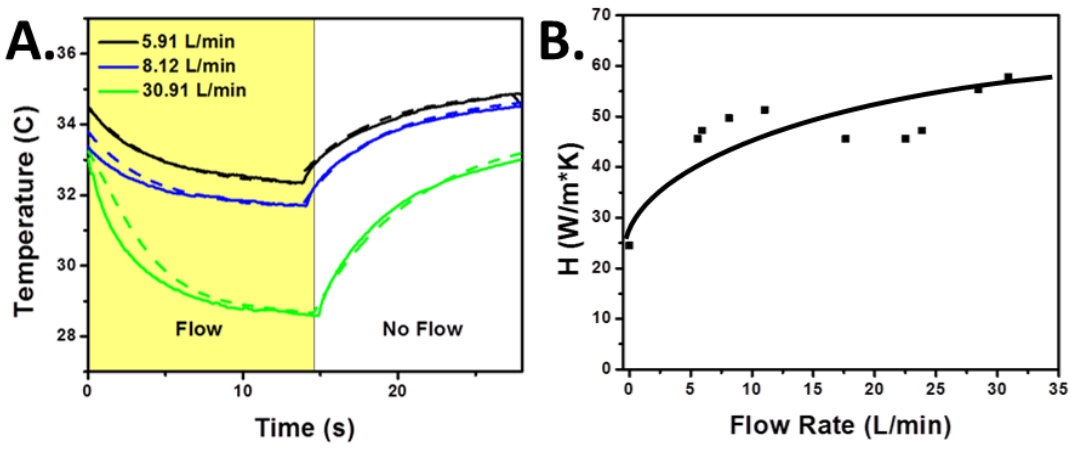

Figure 4-15 (A) Curves demonstrating the testing (solid line) and fitting (dotted line) procedure used to generate the heat transfer convention coefficients (H). Flows were pulsed and the changes in temperature were recorded and modeled. The fitting (dotted line) was performed following equation 4? (B) Corresponding convection coefficient of the sensor (H) as a function of the volumetric flow rate.

Chemical Interaction Characterization

For probing humidity with this setup, the tests can be reframed as the deviation from heat values expected under dry conditions. The heat production will be a function of

two factors: the partial pressure of water in the gas and sensor, and the absorption and desorption rates, as shown in equation 9 as follows:

$$\left(\frac{m * c}{A} * \frac{dT_{Sensor}}{dt}\right)_{Reaction} = B * \frac{dC}{dt} = B * (r_{abs} * [C_{Gas}] - r_{des} * [C_{Sensor}]) \quad 9$$

where r_{abs} and r_{des} are the rates of absorption and desorption, respectively, C_{gas} is the concentration of analyte in the gas surrounding the sensor, and C_{sensor} is the concentration of analyte in the sensing element, where in this case the analyte is humidity.

Since the effects of conduction and convection can be calculated, the heat generation from reactivity can be ascertained. Figure 4-16 demonstrates that the bulk of the changes seen in the sensor temperature are in fact from humidity changes. The figure contrasts the differences seen between an uncoated reference (black line) and a coated sensor (blue line). Comparing these two, the temperature change due to humidity is seen clearly in the coated sensor.

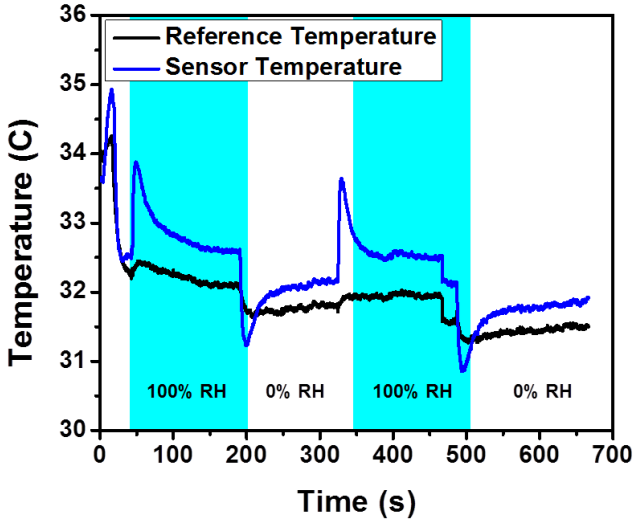

Figure 4-16. A humidity test with temperature measurements from a hydrophobic reference area and hydrophilic sensing area. The reference area was a polystyrene portion of the sensor next to the sensing area.

Figure 4-17 shows that when applying different concentration of relative humidity to the disposable sensor, we can see distinct changes in temperature with the thermal camera by averaging the appropriate areas. Clear differences in magnitude can be seen between 33% relative humidity and 100% relative humidity. Using the appropriate model, it is feasible to measure relative humidity at a fast capture rate (<1s): the heat from humidity can be isolated from other conductive and convective effects, and the heat flux is a direct function of the change in water content of the sensor.

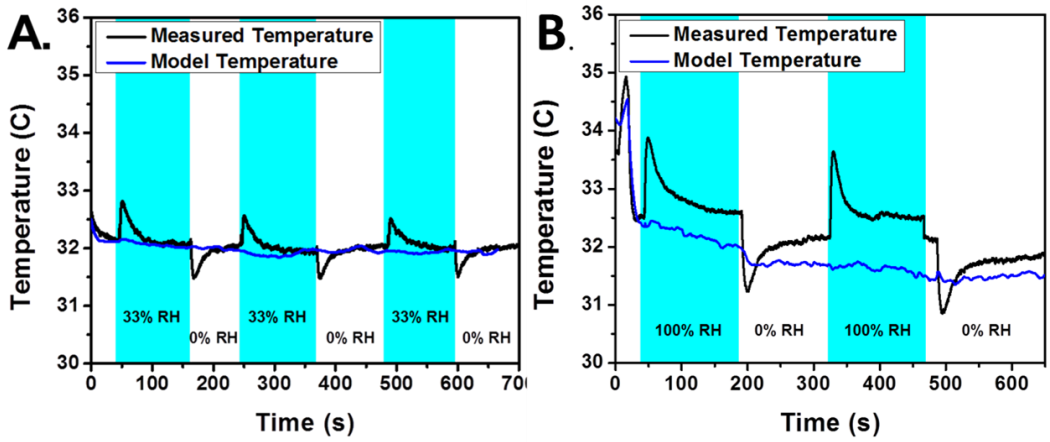

Figure 4-17. Temperature traces which show the measured heat response from pulsing alternating relative humidity levels over the sensor with dry air and air at 33% relative humidity (A) and 100% relative humidity (B). The blue line represents expected temperature values based on conduction ad convection relationships, while the black line represents the measured temperature on the hydrophilic area.

4.3.4 Conclusion

In this work, we demonstrate the utility of the humidity detection via thermal analysis. This can provide a robust and inexpensive measurement for application in harsh environments, such as sewers or food processing operations, or in otherwise difficult environments, such as breath. Using a coated thermistor, we demonstrate the ability to discriminate relative humidity in the range of 0-75% by measuring temperature changes. Using a thermal camera and disposable element, we demonstrate a clear signal due to relative humidity change and provide evidence of a relationship between the magnitude

of change in relative humidity and the magnitude of the signal. In tests conducted, no heat release was observed with exposure to acid gasses, such as pure carbon dioxide or concentrated hydrochloric acid. Future work in this area will be directed to specific sensor design to adapt the needs of different sensing scenarios.

5 Conclusions

Demonstrated here is the development of a sensing platform and colorimetric sensor, along with other works in line with this type of project. The sensing platform is demonstrated to be able to accurately measure flow rate at a minimal flow-resistance via the newly developed Confined Pitot Tube (CPT) flow meter, effectively deliver the sample to the sensor and transduce its color change, and effectively mitigate ambient lighting effects. The colorimetric sensor is demonstrated to be sensitive, specific to CO_2, have a very fast time-response, be reproducible, and be stable over time. In order to account for temperature and humidity, a sophisticated model is constructed in order to take items that are easily measured, convert them into a temperature change value to explicitly predict the next temperature, and track water content during the test. With this platform, we demonstrate the effectiveness of the device to monitor CO_2 in breath. In addition, three other works are shown which demonstrate techniques that will be employed in future endeavors in this project: environmental monitoring and clinical validation. This work delivers a working prototype Capnometer that is capable of accurate measurement of CO_2 and flow rate in breath.

6 Future Work

Future work will involve three main goals: final optimization and packaging of the device, a validation study, and a clinical study. The first step will be the final optimization and packaging of the device. This will consist of fine-tuning the circuit design for robustness, performing the final optimizations for measuring CO_2 and confounding factors (temperature and moisture), and developing better software for user-friendliness. The second goal will be to perform a validation study to evaluate the performance of the device. This will be a simple study, and will consist of recruiting a small cohort of subjects with varying end-tidal CO_2 levels, tidal volumes, and breathing rates with subjects with and without lung obstruction. By performing a validation study, it can be established how accurate the unit is across a variety of breathing conditions and how effective the unit is for classifying lung obstruction in real subjects. The final task will be a clinical study in order to determine the effectiveness of the unit for home monitoring of COPD and the benefit of home monitoring. This will be done by giving a group of COPD patients a CO_2 monitoring device and evaluating whether having them use the device leads to an improved outcome as compared to the current standard of care. This would likely constitute enough work in order to apply for FDA clearance as a class II medical device.

In parallel, work from this project will go into development of a non-invasive cardiac output monitor. The device will first have a rebreathing circuit integrated and have the rebreathing circuit optimized. Similar to above, the device with the rebreathing

circuit will need to validated and eventually have a similar clinical study to evaluate its effectiveness. A validation study will be performed to ensure that the device is accurate across a range of cardiac output values, then a clinical study will be implemented in order to evaluate if the device can improve patient outcomes via home monitoring.

REFERENCES

1. Zhao D, Xian X, Terrera M, et al. A pocket-sized metabolic analyzer for assessment of resting energy expenditure. *Clinical Nutrition.* 2014;33(2):341-347.

2. Bridgeman D. Development of a Point-of-Care Capnography tool for Monitoring Pulmonary Function. *Arizona Bioindustry Association 2015*. Phoenix, Az 2015.

3. Brown RH, Brooker A, Wise RA, et al. Forced expiratory capnography and chronic obstructive pulmonary disease (COPD). *Journal of breath research.* 2013;7(1):017108.

4. You B, Peslin R, Duvivier C, Vu VD, Grilliat J. Expiratory capnography in asthma: evaluation of various shape indices. *European Respiratory Journal.* 1994;7(2):318-323.

5. Anesthesiologists ASo. Standards and Guidlines. 2016; http://www.asahq.org/quality-and-practice-management/standards-and-guidelines. Accessed September 14, 2016.

6. Agus MS, Alexander JL, Mantell PA. Continuous non-invasive end-tidal CO2 monitoring in pediatric inpatients with diabetic ketoacidosis. *Pediatric diabetes.* 2006;7(4):196-200.

7. Fearon DM, Steele DW. End-tidal carbon dioxide predicts the presence and severity of acidosis in children with diabetes. *Academic emergency medicine.* 2002;9(12):1373-1378.

8. Isserles SA, Breen PH. Can Changes in End-Tidal Pco2 Measure Changes in Cardiac Output? *Anesthesia & Analgesia.* 1991;73(6):808-814.

9. Gravenstein JS, Jaffe MB, Gravenstein N, Paulus DA. *Capnography*: Cambridge University Press; 2011.

10. Linko K, Paloheimo M, Tammisto T. Capnography for detection of accidental oesophageal intubation. *Acta anaesthesiologica scandinavica.* 1983;27(3):199-202.

11. Walsh BK, Crotwell DN, Restrepo RD. Capnography/Capnometry during mechanical ventilation: 2011. *Respiratory care.* 2011;56(4):503-509.

12. Standardization IOf. ISO 80601-2-55:2011. In: Standardization IOf, ed2011.

13. Control CfD, Prevention. Chronic obstructive pulmonary disease among adults--United States, 2011. *MMWR. Morbidity and mortality weekly report.* 2012;61(46):938.

14. Akinbami LJ, Moorman JE, Bailey C, et al. Trends in asthma prevalence, health care use, and mortality in the United States, 2001–2010. *NCHS data brief.* 2012;94(94):1-8.

15. Rabe KF, Hurd S, Anzueto A, et al. Global strategy for the diagnosis, management, and prevention of chronic obstructive pulmonary disease: GOLD executive summary. *American journal of respiratory and critical care medicine.* 2007;176(6):532-555.

16. Bacharier LB, Strunk RC, Mauger D, White D, Lemanske Jr RF, Sorkness CA. Classifying asthma severity in children: mismatch between symptoms, medication use, and lung function. *American journal of respiratory and critical care medicine.* 2004;170(4):426-432.

17. Miller MK, Johnson C, Miller DP, et al. Severity assessment in asthma: an evolving concept. *Journal of allergy and clinical immunology.* 2005;116(5):990-995.

18. Farish SE, Garcia PS. Capnography primer for oral and maxillofacial surgery: Review and technical considerations. *Journal of anesthesia & clinical research.* 2013;4(3):295.

19. Romero PV, Rodriguez B, De Oliveira D, Blanch L, Manresa F. Volumetric capnography and chronic obstructive pulmonary disease staging. *International journal of chronic obstructive pulmonary disease.* 2007;2(3):381.

20. Yaron M, Padyk P, Hutsinpiller M, Cairns CB. Utility of the expiratory capnogram in the assessment of bronchospasm. *Annals of emergency medicine.* 1996;28(4):403-407.

21. Krauss B, Deykin A, Lam A, et al. Capnogram shape in obstructive lung disease. *Anesthesia & Analgesia.* 2005;100(3):884-888.

22. Braman SS. Hospital Readmissions for COPD: We Can Meet the Challenge. *Chronic Obstructive Pulmonary Diseases: Journal of the COPD Foundation.*2(1):4-7.

23. Coventry PA, Gemmell I, Todd CJ. Psychosocial risk factors for hospital readmission in COPD patients on early discharge services: a cohort study. *BMC pulmonary medicine.* 2011;11(1):1.

24. Garcia-Aymerich J, Farrero E, Felez M, Izquierdo J, Marrades R, Anto J. Risk factors of readmission to hospital for a COPD exacerbation: a prospective study. *Thorax.* 2003;58(2):100-105.

25. Craig Stump DJ, Yulia Abidov, NJ Tao, Karen Herbst, Erica Forzani. An Integrative Personalized Professional Practice using Mobile Technologies for Weight Management2016.

26. Elixhauser A, Au DH, Podulka J. Readmissions for chronic obstructive pulmonary disease, 2008. 2011.

27. Stradling J. Hypercapnia during oxygen therapy in airways obstruction: a reappraisal. *Thorax.* 1986;41(12):897.

28. Mitrouska I, Tzanakis N, Siafakas N. Oxygen therapy in chronic obstructive pulmonary disease. *European Respiratory Monograph.* 2006;38:302.

29. Physicians AAoF. AHA Releases Statement on Exercise and Heart Failure. 2003; http://www.aafp.org/afp/2003/0901/p969.html. Accessed January 4, 2017.

30. Prevention CfDCa. Heart Disease Facts. 2010; https://www.cdc.gov/heartdisease/facts.htm. Accessed January 4, 2017.

31. Critchley LAH. *Minimally invasive cardiac output monitoring in the year 2012*: INTECH Open Access Publisher; 2013.

32. Haryadi DG, Orr JA, Kuck K, McJames S, Westenskow DR. Partial CO2 rebreathing indirect Fick technique for non-invasive measurement of cardiac output. *Journal of clinical monitoring and computing.* 2000;16(5-6):361-374.

33. Odenstedt H, Stenqvist O, Lundin S. Clinical evaluation of a partial CO2 rebreathing technique for cardiac output monitoring in critically ill patients. *Acta anaesthesiologica scandinavica.* 2002;46(2):152-159.

34. Van Heerden P, Baker S, Lim S, Weidman C, Bulsara M. Clinical evaluation of the non-invasive cardiac output (NICO) monitor in the intensive care unit. *Anaesthesia and intensive care.* 2000;28(4):427-430.

35. Illinois S. Thermal Conductivity Analyzers. 2016; http://www.systechillinois.com/en/thermal-conductivity_52.html. Accessed September 13, 2016.

36. Dextens. Thermal conductivity multiple gas sensor: carbon dioxide (CO2), nitrogen (N2), hydrogen (H2). http://www.directindustry.com/prod/dextens/product-92615-961055.html. Accessed September 14, 2016.

37. How Does an NDIR CO2 Sensor Work? Accessed November 9, 2016.

38. Bridgeman D, Corral J, Quach A, Xian X, Forzani E. Colorimetric humidity sensor based on liquid composite materials for the monitoring of food and pharmaceuticals. *Langmuir.* 2014;30(35):10785-10791.

39. KRING EV, LAUTENBERGER WJ, BARRY BAKER W, DOUGLAS JJ, HOFFMAN RA. A new passive colorimetric air monitoring badge system for ammonia, sulfur dioxide and nitrogen dioxide. *The American Industrial Hygiene Association Journal.* 1981;42(5):373-381.

40. Lopez-Ruiz N, Curto VF, Erenas MM, et al. Smartphone-based simultaneous pH and nitrite colorimetric determination for paper microfluidic devices. *Analytical chemistry.* 2014;86(19):9554-9562.

41. Ye T, He C, Qu Y, et al. A simple colorimetric device for rapid detection of Hg 2+ in water. *Analyst.* 2012;137(18):4131-4134.

42. Bentley RA, Griffin OG, Love RG, Muir DC, Sweetland KF. Acceptable levels for breathing resistance of respiratory apparatus. *Archives of Environmental Health: An International Journal.* 1973;27(4):273-280.

43. Goldstein R. *Fluid mechanics measurements*: CRC Press; 1996.

44. Ilsley AH, Hart JD, Withers RT, Roberts JG. Evaluation of five small turbine-type respirometers used in adult anesthesia. *Journal of clinical monitoring.* 1993;9(3):196-201.

45. Yeh MP, Adams TD, Gardner RM, Yanowitz FG. *Turbine flowmeter vs. Fleisch pneumotachometer: a comparative study for exercise testing.* Vol 631987.

46. Yoshiya I, Shimada Y, Tanaka K. Evaluation of a hot-wire respiratory flowmeter for clinical applicability. *Journal of Applied Physiology.* 1979;47(5):1131-1135.

47. Blumenfeld W, Wilson PD, Turney S. A mathematical model for the ultrasonic measurement of respiratory flow. *Medical and biological engineering.* 1974;12(5):621-625.

48. Kreit JW, Sciurba FC. The accuracy of pneumotachograph measurements during mechanical ventilation. *American journal of respiratory and critical care medicine.* 1996;154(4):913-917.

49. LaNasa PJ, Upp EL. *Fluid Flow Measurement: A Practical Guide to Accurate Flow Measurement*: Butterworth-Heinemann; 2014.

50. Bird RB, Stewart WE, Lightfoot EN. *Transport phenomena*: John Wiley & Sons; 2007.

51. Kolmogorov AN. Equations of turbulent motion in an incompressible fluid. Paper presented at: Dokl. Akad. Nauk SSSR1941.

52. Wilcox DC. Formulation of the kw Turbulence Model Revisited. *AIAA journal.* 2008;46(11):2823-2838.

53. Korr. http://korr.com/products/medical-metabolic-rate-analysis-system/.

54. Robert Harr PJ, Mark A. Best. Spirometry tests. [Website]. http://www.surgeryencyclopedia.com/Pa-St/Spirometry-Tests.html. Accessed 2/18, 2015.

55. Zhao D. *A Novel Handheld Real-time Carbon Dioxide Analyzer for Health and Environmental Applications*, Arizona State University; 2014.

56. Borisov SM, Waldhier MC, Klimant I, Wolfbeis OS. Optical carbon dioxide sensors based on silicone-encapsulated room-temperature ionic liquids. *Chemistry of materials.* 2007;19(25):6187-6194.

57. Nakamura N, Amao Y. Optical sensor for carbon dioxide combining colorimetric change of a pH indicator and a reference luminescent dye. *Analytical and bioanalytical chemistry.* 2003;376(5):642-646.

58. Segawa H, Ohnishi E, Arai Y, Yoshida K. Sensitivity of fiber-optic carbon dioxide sensors utilizing indicator dye. *Sensors and Actuators B: Chemical.* 2003;94(3):276-281.

59. Zhao D, Miller D, Shao D, et al. A personal device for analyzing carbon dioxide in real time and real breath: Experimental investigation and computational simulation. *Sensors and Actuators B: Chemical.* 2013;183:627-635.

60. Zhao D, Miller D, Xian X, Tsow F, Forzani ES. A novel real-time carbon dioxide analyzer for health and environmental applications. *Sensors and Actuators B: Chemical.* 2014;195:171-176.

61. Caplow M. Kinetics of carbamate formation and breakdown. *Journal of the American Chemical Society.* 1968;90(24):6795-6803.

62. Dickson A, Millero FJ. A comparison of the equilibrium constants for the dissociation of carbonic acid in seawater media. *Deep Sea Research Part A. Oceanographic Research Papers.* 1987;34(10):1733-1743.

63. Mehrbach C. Measurement of the apparent dissociation constants of carbonic acid in seawater at atmospheric pressure. 1973.

64. Garg LC, Maren TH. The rates of hydration of carbon dioxide and dehydration of carbonic acid at 37. *Biochimica et Biophysica Acta (BBA)-General Subjects.* 1972;261(1):70-76.

65. Gibbons BH, Edsall JT. Rate of hydration of carbon dioxide and dehydration of carbonic acid at 25. *Journal of biological chemistry.* 1963;238(10):3502-3507.

66. Jensen A, Jensen J, Faurholt C. Studies on carbamates. 6. The carbamate of glycine. *Acta Chemica Scandinavica.* 1952;6(3):395-397.

67. Convective Heat Transfer. http://www.engineeringtoolbox.com/convective-heat-transfer-d_430.html. Accessed 11/16, 2016.

68. Pinheiro Volp AC, Esteves de Oliveira FC, Duarte Moreira Alves R, Esteves EA, Bressan J. Energy expenditure: components and evaluation methods. *Nutr Hosp.* 2011;26(3):430-440.

69. Ferrannini E. The theoretical bases of indirect calorimetry: a review. *Metabolism.* 1988;37(3):287-301.

70. Harris JA, Benedict FG. A biometric study of human basal metabolism. *Proc Natl Acad Sci U S A.* 1918;4:370–373.

71. Frankenfield D, Roth-Yousey L, Compher C. Comparison of predictive equations for resting metabolic rate in healthy nonobese and obese adults: a systematic review. *J Am Diet Assoc.* 2005;105(5):775-789.

72. Leibel RL, Rosenbaum M, Hirsch J. Changes in energy expenditure resulting from altered body weight. *N Engl J Med.* 1995;332(10):621-628.

73. Nelson KM, Weinsier RL, Long CL, Schutz Y. Prediction of resting energy expenditure from fat-free mass and fat mass. *Am J Clin Nutr.* 1992;56(5):848-856.

74. Weir JB. New methods for calculating metabolic rate with special reference to protein metabolism. *J Physiol.* 1949;109:1-9.

75. Zhao D, Xian X, Terrera M, et al. A pocket-sized metabolic analyzer for assessment of resting energy expenditure. *Clin Nutr.* 2014;33:341-347.

76. http://korr.com/products/reevue/.

77. http://www.mimhs.com/bodygem/techspecs/.

78. McArdle WD, Katch FI, Katch VL. Exercise Physiology: Energy, Nutrition, & Human Performance. *Lippincott Williams & Wilkins.* 2007.

79. Frankenfield DC, Muth ER, Rowe WA. The Harris-Benedict studies of human basal metabolism: history and limitations. *J Am Diet Assoc.* 1998;98(4):439-445.

80. Flatt JP. Body composition, respiratory quotient, and weight maintenance. *Am J Clin Nutr.* 1995;62(5):1107S-1117S.

81. McDoniel SO. Systematic review on use of a handheld indirect calorimeter to assess energy needs in adults and children. *Int J Sport Nutr Exerc Metab.* 2007;17(5):491-500.

82. Poehlman ET, Horton ES. The impact of food intake and exercise on energy expenditure. *Nutr Rev.* 1989;47(5):129-137.

83. Rizvi SSH, Perdue RR. Requirements for foods packaged in polymeric films. *C R C Critical Reviews in Food Science and Nutrition.* 1981;14(2):111.

84. Yam KL, Takhistov PT, Miltz J. Intelligent Packaging: Concepts and Applications. *Journal of Food Science.* 2005;70(1):R1-R10.

85. Podczeck F, Newton JM, James MB. The influence of constant and changing relative humidity of the air on the autoadhesion force between pharmaceutical powder particles. *International Journal of Pharmaceutics.* 12/6/ 1996;145(1–2):221-229.

86. Kidnay AJ, Parrish WR. *Fundamentals of natural gas processing.* Vol 200: CRC Press; 2006.

87. Beyersmann D, Hartwig A. The genetic toxicology of cobalt. *Toxicology and applied pharmacology.* 1992;115(1):137-145.

88. Lauwerys R, Lison D. Health risks associated with cobalt exposure — an overview. *Science of The Total Environment.* 6/30/ 1994;150(1–3):1-6.

89. Stohs SJ, Bagchi D. Oxidative mechanisms in the toxicity of metal ions. *Free Radical Biology and Medicine.* 2// 1995;18(2):321-336.

90. Hawkeye MM, Brett MJ. Optimized Colorimetric Photonic-Crystal Humidity Sensor Fabricated Using Glancing Angle Deposition. *Advanced Functional Materials.* 2011;21(19):3652-3658.

91. Tian E, Wang J, Zheng Y, Song Y, Jiang L, Zhu D. Colorful humidity sensitive photonic crystal hydrogel. *J.Mater.Chem.* 2008;18(10):1116-1122.

92. Xuan R, Wu Q, Yin Y, Ge J. Magnetically assembled photonic crystal film for humidity sensing. *Journal of Materials Chemistry.* 2011;21(11):3672-3676.

93. Luechinger NA, Loher S, Athanassiou EK, Grass RN, Stark WJ. Highly Sensitive Optical Detection of Humidity on Polymer/Metal Nanoparticle Hybrid Films. *Langmuir.* 2007;23(6):3473-3477.

94. Lopes P, Saucier C, Teissedre P-L, Glories Y. Main routes of oxygen ingress through different closures into wine bottles. *Journal of agricultural and food chemistry.* 2007;55(13):5167-5170.

95. Lopes P, Saucier C, Teissedre P-L, Glories Y. Impact of storage position on oxygen ingress through different closures into wine bottles. *Journal of agricultural and food chemistry.* 2006;54(18):6741-6746.

96. Marmion DM. *Handbook of US colorants: foods, drugs, cosmetics, and medical devices*: John Wiley & Sons; 1991.

97. Saltmarsh M, Saltmarsh M, Barlow S. *Essential guide to food additives*: Royal Society of Chemistry; 2013.

98. Gaunt IF, Grasso P, Kiss IS, Gangolli SD. Short-term toxicity study on Indigo Carmine in the pig. *Food and cosmetics toxicology.* 1969;7(0):17-24.

99. Hooson J, Gaunt IF, Kiss IS, Grasso P, Butterworth KR. Long-term toxicity of indigo carmine in mice. *Food and cosmetics toxicology.* 1975;13(2):167-176.

100. Fail PA, Chapin RE, Price CJ, Heindel JJ. General, reproductive, developmental, and endocrine toxicity of boronated compounds. *Reproductive Toxicology.* 1998;12(1):1-18.

101. Burdock GA. *Encyclopedia of food and color additives.* Vol 3: CRC Press; 1997.

102. Villota R, Hawkes JG, Cochrane H. Food applications and the toxicological and nutritional implications of amorphous silicon dioxide. *Critical Reviews in Food Science & Nutrition.* 1986;23(4):289-321.

103. Prado AGS, Bolzon LB, Pedroso CP, Moura AO, Costa LL. Nb2O5 as efficient and recyclable photocatalyst for indigo carmine degradation. *Applied Catalysis B: Environmental.* 2008;82(3–4):219-224.

104. Vautier M, Guillard C, Herrmann J-M. Photocatalytic Degradation of Dyes in Water: Case Study of Indigo and of Indigo Carmine. *Journal of Catalysis.* 2001;201(1):46-59.

105. Sousa MM, Miguel C, Rodrigues I, et al. A photochemical study on the blue dye indigo: from solution to ancient Andean textiles. *Photochemical & Photobiological Sciences.* 2008;7(11):1353-1359.

106. Zhang C, Khaliullin RZ, Bovi D, Guidoni L, KÃ¼hne TD. Vibrational Signature of Water Molecules in Asymmetric Hydrogen Bonding Environments. *The Journal of Physical Chemistry Letters.* 2013;4(19):3245-3250.

107. Ludvigsson M, Lindgren J, Tegenfeldt J. FTIR study of water in cast Nafion films. *Electrochimica Acta.* 2000;45(14):2267-2271.

108. Smith BC. *Infrared spectral interpretation: a systematic approach*: CRC press; 1998.

109. Vandeginste BGMt, De Galan L. Critical evaluation of curve fitting in infrared spectrometry. *Analytical Chemistry.* 1975;47(13):2124-2132.

110. Jun L, Shuping X, Shiyang G. FT-IR and Raman spectroscopic study of hydrated borates. *Spectrochimica Acta Part A: Molecular and Biomolecular Spectroscopy.* 1995;51(4):519-532.

111. Momii RK, Nachtrieb NH. Nuclear magnetic resonance study of borate-polyborate equilibria in aqueous solution. *Inorganic chemistry.* 1967;6(6):1189-1192.

112. Zhou Y, Fang C, Fang Y, Zhu F. Polyborates in aqueous borate solution: A Raman and DFT theory investigation. *Spectrochimica Acta Part A: Molecular and Biomolecular Spectroscopy.* 2011;83(1):82-87.

113. Nyquist RA, Kagel RO. *Handbook of infrared and raman spectra of inorganic compounds and organic salts: infrared spectra of inorganic compounds.* Vol 4: Academic press; 1972.

114. Farmer JB. Metal Borates. In: Emeléus HJ, Sharpe AG, eds. *Advances in Inorganic Chemistry.* Vol Volume 25: Academic Press; 1982:187-237.

115. Hua D, Hanxi Y, Xinping A, Chuansin C. Hydrogen production from catalytic hydrolysis of sodium borohydride solution using nickel boride catalyst. *International Journal of Hydrogen Energy.* 2003;28(10):1095-1100.

116. Marrero-Alfonso EY, Gray JR, Davis TA, Matthews MA. Minimizing water utilization in hydrolysis of sodium borohydride: the role of sodium metaborate hydrates. *International Journal of Hydrogen Energy.* 2007;32(18):4723-4730.

117. Schlesinger HI, Brown HC, Finholt AE, Gilbreath JR, Hoekstra HR, Hyde EK. Sodium Borohydride, Its Hydrolysis and its Use as a Reducing Agent and in the Generation of Hydrogen1. *Journal of the American Chemical Society.* 1953;75(1):215-219.

118. BershteÄ-n VA, Egorov VM. *Differential scanning calorimetry of polymers :physics, chemistry, analysis, technology*. New York: Ellis Horwood; 1994.

119. Grenier G, Westrum EF. The Heat Capacity and Thermodynamic Functions of Sodium Metaborate from 5 to 350Â°K. *Journal of the American Chemical Society.* 1956;78(24):6226-6227.

120. Scovazzo P, Visser AE, Davis Jr JH, et al. Supported ionic liquid membranes and facilitated ionic liquid membranes. *ChemInform.* 2002;33(48):240-240.

121. Koch GH, Brongers MP, Thomson N, Virmanio Y, Payer JH, Kutz M. Cost of corrosion in the United States. *Handbook of environmental degradation of materials.* 2005:3-24.

122. Jiang G, Keller J, Bond PL, Yuan Z. Predicting concrete corrosion of sewers using artificial neural network. *Water research.* 2016;92:52-60.

123. Wells T, Melchers R. Modelling the life-cycle of concrete gravity sewers subject to microbial corrosion. Paper presented at: Life-Cycle of Engineering Systems: Emphasis on Sustainable Civil Infrastructure: Proceedings of the Fifth International Symposium on Life-Cycle Civil Engineering (IALCCE 2016), 16-19 October 2016, Delft, The Netherlands2016.

124. Alwis LS, Bustamante H, Bremer K, Roth B, Sun T, Grattan KT. A pilot study: Evaluation of sensor system design for optical fibre humidity sensors subjected to aggressive air sewer environment. Paper presented at: SENSORS, 2016 IEEE2016.

125. Alwis LS, Bustamante H, Bremer K, Roth B, Sun T, Grattan K. Evaluation of the durability and performance of FBG-based sensors for monitoring moisture in an aggressive gaseous waste sewer environment. *Journal of Lightwave Technology.* 2016.

126. Thomas PJ, Hellevang JO. A fully distributed fibre optic sensor for relative humidity measurements. *Sensors and Actuators B: Chemical.* 2017.

127. Sebastian P, Bruneau D, Collignan A, Rivier M. Drying and smoking of meat: heat and mass transfer modeling and experimental analysis. *Journal of food engineering.* 2005;70(2):227-243.

128. Zhang W, Ma H, Yang SX. An inexpensive, stable, and accurate relative humidity measurement method for challenging environments. *Sensors.* 2016;16(3):398.

129. Nathakaranakule A, Kraiwanichkul W, Soponronnarit S. Comparative study of different combined superheated-steam drying techniques for chicken meat. *Journal of Food Engineering.* 2007;80(4):1023-1030.

130. Bridgeman D, Zhao D, Tsow F, Xian X, Forzani E. A Non-Invasive and Inexpensive Capnography Device for the Monitoring of COPD and Other Pulmonary Diseases. *IEEE Healthcare Innovation Point-of-Care Technologies Conference*. Seattle, Washington: IEEE; 2014.

131. Davies S, Spanel P, Smith D. Quantitative analysis of ammonia on the breath of patients in end-stage renal failure. *Kidney international.* 1997;52(1):223-228.

132. Qian Z. *The Impact of Humidity on an Optical Chemical Sensing Device for Non-invasive Exhaled Gas Monitoring*, University of Cincinnati; 2016.

133. Jalal AH, Umasankar Y, Gonzalez PJ, Alfonso A, Bhansali S. Multimodal technique to eliminate humidity interference for specific detection of ethanol. *Biosensors and Bioelectronics.* 2017;87:522-530.

134. Zito CA, Perfecto TM, Volanti DP. Impact of reduced graphene oxide on the ethanol sensing performance of hollow SnO 2 nanoparticles under humid atmosphere. *Sensors and Actuators B: Chemical.* 2017.

135. Yao MS, Tang WX, Wang GE, Nath B, Xu G. MOF Thin Film-Coated Metal Oxide Nanowire Array: Significantly Improved Chemiresistor Sensor Performance. *Advanced Materials.* 2016;28(26):5229-5234.

136. FLIR. http://www.flir.com/home/. Accessed 2/1, 2017.

137. Bridgeman D. The Development of a New Differential Pressure Flow Meter for Bidirectional Measurement of Human Breath Flow. *American Institute for Chemical Engineers 2015 Annual Meeting*. Salt Lake City, Ut 2015.

138. Whitaker S. Forced convection heat transfer correlations for flow in pipes, past flat plates, single cylinders, single spheres, and for flow in packed beds and tube bundles. *AIChE Journal.* 1972;18(2):361-371.